

Classical and semiclassical approaches to excitons in cuprous oxide

Von der Fakultät Mathematik und Physik der Universität Stuttgart
zur Erlangung der Würde eines Doktors der Naturwissenschaften
(Dr. rer. nat.) genehmigte Abhandlung

Vorgelegt von

Jan Ertl

aus Stuttgart

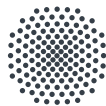
Hauptberichter:

Prof. Dr. Jörg Main

Mitberichter:

Prof. Dr. Johannes Roth

Tag der mündlichen Prüfung: 19.07.2024



Universität Stuttgart

1. Institut für Theoretische Physik

2024



Inhaltsangabe

Wird ein Elektron vom Valenzband in das Leitungsband angeregt, so lässt es ein positiv geladenes Loch im Valenzband zurück, welches mit dem Elektron über die Coulomb-Wechselwirkung interagiert. Dadurch können sich gebundene Zustände, die Exzitonen, bilden. Diese können als Analogon des Wasserstoffatoms im Festkörper betrachtet werden. Als Solches lässt sich für die Exzitonen eine Rydberg-Serie beobachten. Während in den meisten Halbleitern nur die niedrigsten Zustände experimentell zugänglich sind, konnte für Kupferoxydul eine solche Serie von T. Kazimierczuk et al. [Nature **514**, 343 (2014)] bis zu Hauptquantenzahlen von $n = 25$ nachgewiesen werden. Diese Zustände erreichen Ausdehnungen im μm Bereich und liegen damit in einer Region, in der das Korrespondenzprinzip greifen sollte und quantenmechanische Eigenschaften sich über klassische Dynamik verstehen lassen.

Eine genauere Untersuchung der Spektren von Kupferoxydul zeigt Abweichungen von einem reinen wasserstoffartigen Verhalten. Diese Abweichungen lassen sich auf die komplexe Bandstruktur von Kupferoxydul zurückführen, welche die kubische O_h Symmetrie des Kristalls trägt. Zur theoretischen Beschreibung des Systems wird ein Quasispin $I = 1$ eingeführt, welcher das dreifach entartete Valenzband beschreibt. Durch die Kopplung des Quasispins an den Spin des Lochs im Valenzband spaltet das Valenzband auf, was zu einer gelben und zwei grünen Exzitonenserien mit leichten und schweren Löchern führt.

In dieser Doktorarbeit entwickeln wir eine semiklassische Interpretation für Exzitonen in Kupferoxydul, die über die wasserstoffartige Beschreibung hinaus geht. Dazu wird ein adiabatischer Ansatz eingeführt, wobei die Terme des Hamiltonians welche die Bandstruktur beschreiben, in einer Basis für den Quasi- und Lochspin diagonalisiert werden. Dies führt auf eine Beschreibung über Energieflächen im Impulsraum, wobei sich diese Energieflächen direkt den verschiedenen Exzitonenserien zuordnen lassen.

Um klassische Exzitonenserien zu berechnen, wählt man nun die Energiefläche für die zu betrachtende Serie und löst dann die Hamiltonschen Bewegungsgleichungen. Da die Energieflächen die kubische Symmetrie des Systems aufweisen, wird die Symmetrie gegenüber einem wasserstoffartigem System stark reduziert, was die Existenz drei-

dimensionaler Bahnen und chaotischer Dynamik ermöglicht.

Für die gelbe Serie beobachten wir einen fast vollständig regulären Phasenraum, der sich durch quasiperiodische Bewegung auf regulären Torusstrukturen auszeichnet, sowie kleine chaotische Bereiche.

Um nun die Existenz einer solchen klassischen Exzitonendynamik in den quantenmechanischen Spektren nachzuweisen, führen wir eine Skalierungstechnik ein. In der Fouriertransformierten der skalierten quantenmechanischen Spektren lassen sich die Peaks dann, mithilfe semiklassischer Theorien, durch klassische Bahnen erklären. Dabei zeigt sich, dass die Abweichung von einem reinen wasserstoffartigen Verhalten am Größten ist für niedrige Energien.

Ausgehend vom vollen Hamiltonian mit kubischer Symmetrie entwickeln wir ein sphärisches Modell, über das wir die Quanteneffekte der gelben Serie über eine semiklassische Torusquantisierung berechnen. Ein Vergleich mit quantenmechanischen Rechnungen zeigt dabei eine gute Übereinstimmung mit unseren semiklassischen Resultaten und erlaubt somit eine Zuordnung von Exziton Bahnen zu den entsprechenden Quantenzuständen, ähnlich wie im Bohrschen Atommodell.

Abschließend stellen wir die Dynamik der gelben und grünen Exzitonenserie gegenüber. Dazu analysieren wir den Phasenraum mithilfe von Poincaré-Schnitten in den Symmetrieebenen und Lagrange-Deskriptoren. Außerdem betrachten wir die Lyapunov-Stabilität ausgewählter Orbits. Dabei zeigt sich die Existenz chaotischer Bereiche sowohl für die gelbe als auch die grüne Serie, die chaotischen Anteile sind jedoch für die grüne Serie deutlich größer als für die gelbe Serie. Es zeigt sich somit, dass Exzitonen in Kupferoxydul ein Zweikörperproblem darstellen, in dem auch bereits ohne den Einfluss äußerer Felder Chaos auftritt.



Abstract

When an electron is excited from the valence into the conduction band it leaves behind a positively charged hole in the valence band to which it can couple through the Coulomb interaction. Bound states of electrons and holes, the excitons, are the solid state analogue of the hydrogen atom. As such they follow a Rydberg series. T. Kazimierczuk et al. [Nature **514**, 343 (2014)] were able to show the existence of Rydberg excitons in cuprous oxide up to principle quantum number $n = 25$. These states then have extensions in the μm range and thus lie in a region where the correspondence principle is applicable and quantum mechanics turns into classical mechanics.

A more precise study of experimental spectra reveals significant deviations from a purely hydrogen-like behavior. These deviations can be traced to the complex valence band structure of cuprous oxide which inherits the cubic O_h symmetry of the system. A theoretical description of the band structure introduces new degrees of freedom, i.e., a quasispin $I = 1$ describing the three-fold degenerate valence band. Due to the coupling of quasispin and hole spin the valence band splits resulting in a yellow exciton series and two green exciton series with light and heavy holes.

In this thesis we provide a semiclassical interpretation for excitons in cuprous oxide beyond the hydrogen-like model. To this end we introduce an adiabatic approach diagonalizing the band structure part of the Hamiltonian in a basis for quasi- and hole spin. This leads to a description via energy surfaces in momentum space, which correspond to the different exciton series.

Classical dynamics can be calculated by choosing the energy surface of the series under interest and integrating Hamilton's equations of motion. Due to the energy surfaces the symmetry is drastically reduced compared to the hydrogen-like problem now allowing for the existence of fully three-dimensional orbits as well as the possibility of chaotic dynamics. For the yellow exciton series we find mostly regular phase space regions with quasi-periodic motion on near-integrable tori and small chaotic phase space regions.

To demonstrate the existence of classical exciton orbits in the quantum spectra we show that the quantum mechanical recurrence spectra exhibit peaks, which, by appli-

cation of semiclassical theories and a scaling transformation, can be directly related to classical periodic exciton orbits. An analysis of the energy dependence reveals that the dynamics deviations' from a purely hydrogen-like behavior increase with decreasing energy.

Starting from the full Hamiltonian we develop a spherical model from which we are able to derive the quantum defects of the yellow exciton series using a semiclassical torus quantization. A comparison with quantum mechanical calculations show good agreement with our semiclassical results, thus allowing to identify individual quantum states by a corresponding classical exciton orbit in analogy to Bohr's atomic model.

Finally, we provide a comparison of yellow exciton series with the two distinct green exciton series. The phase space is analyzed by application of Poincaré surfaces of section and Lagrangian descriptors. In addition, we investigate the Lyapunov stability of individual orbits. The analysis reveals the existence of a classically chaotic exciton dynamics for both yellow and green excitons, however, the chaotic regions are more pronounced for the green than for the yellow excitons. Excitons in cuprous oxide thus provide an example of a two-particle system with chaos even without the application of external fields.



Contents

Inhaltsangabe	3
Abstract	5
1. Introduction	13
2. Nonlinear dynamics in Hamiltonian systems	19
2.1. Conservative Hamiltonian systems	19
2.2. Integrable systems	20
2.3. Near-integrable systems	22
2.3.1. KAM theorem	22
2.3.2. Poincaré-Birkhoff theorem	23
2.4. Methods to sample phase space	25
2.4.1. Poincaré surfaces of section	25
2.4.2. Stability of orbits	25
2.4.3. Lagrangian descriptors	26
3. Semiclassical description of Hamiltonian systems	27
3.1. Integrable systems	27
3.2. Non-integrable systems	32
4. From solid state systems to excitons in cuprous oxide	35
4.1. Electronic structure of solid state systems	35
4.1.1. Born-Oppenheimer approximation	36
4.1.2. Free electron model	37
4.1.3. Structure of crystalline solids	38
4.1.4. Bloch functions	39
4.1.5. Nearly free electrons	40

4.1.6. Effective mass and electron holes	42
4.2. Excitons in cuprous oxide	42
4.2.1. Hydrogen-like model for excitons	43
4.2.2. Cuprous oxide	44
5. Adiabatic approach for the exciton dynamics in cuprous oxide	51
5.1. Adiabatic approach	51
5.1.1. Formal derivation	53
5.2. Calculation of energy surfaces	55
5.2.1. Analytical expressions for the energy surfaces	55
5.2.2. Solution of cubic polynomial equations	56
5.2.3. Revisiting the cubic symmetry of cuprous oxide	58
6. Classical dynamics of the yellow exciton series	61
6.1. Classical exciton orbits and PSOS	63
6.2. Stability properties of periodic orbits	67
6.3. Action and ordering scheme for orbits in cuprous oxide	68
6.4. Calculation of action variables	71
7. Evidence for the existence of exciton orbits in quantum spectra	73
7.1. Systems with scaling property	73
7.2. Scaling technique for excitons in cuprous oxide	74
7.3. Calculation of the trace formula amplitudes	75
7.4. Verification of exciton orbits in quantum spectra	77
7.4.1. Scaled exciton spectra	77
7.4.2. Quantum recurrence spectra	78
7.4.3. Semiclassical analysis and discussion	80
8. Quantum defects of the yellow exciton series in cuprous oxide	83
8.1. Spherical averages of energy surfaces in cuprous oxide	85
8.2. EBK-quantization for excitons in cuprous oxide	86
9. Chaos in the green exciton series	89
9.1. Dynamics at $n_0 = 5$	89
9.2. Bifurcations of the central green exciton orbit	91
9.3. Lyapunov exponents	92
9.4. Analysis of the full phase space with LDs	94
10. Conclusion and outlook	97
A. Material parameters	101
B. Exciton-Hartree units	103

C. Matrix representation of angular momentum operators	105
D. Functions for the calculation of energy surfaces in cuprous oxide	107
Bibliography	109
Zusammenfassung in deutscher Sprache	127
Curriculum Vitae	137
Danksagung	139



List of abbreviations

cb	conduction band
e	electron
e.g.	for example
EBK	Einstein-Brillouin-Keller (method)
eff	effective
Eq.	equation
et al.	and others
exc	exciton
Fig.	figure
g	gap
g,hh	green series with heavy holes
g,lh	green series with light holes
H	hydrogen
h	hole
i.e.	that is
KAM	Kolmogorov-Arnold-Moser (theorem)
LD	Lagrangian descriptor

List of abbreviations

pc	primitive cell
po	periodic orbit
ppo	primitive periodic orbit
PSOS	Poincaré surface of section
Ref.	reference
Ryd	Rydberg
Sec.	section
vb	valence band
WKB	Wenzel-Kramer-Brillouin (method)
y	yellow series

1 Introduction

Classical physics accurately describe observed phenomena on mesoscopic to macroscopic length scales and thus play a crucial role in our understanding and perception of nature. The development of classical physics started with Isaac Newton. The introduction of his universal law of gravity and the development of infinitesimal calculus as well as his laws of motion laid down the foundations of classical mechanics. This framework allowed for a theoretical derivation of the planetary motion on Kepler ellipses in the two-body problem of sun and planet. In this case the dynamics is completely regular. The system is called integrable when for every degree of freedom an independent constant of motion exists. For a bound system the dynamics in phase space is confined to regular tori. For periodic orbits the frequency ratios of cycles on the torus is given by rational numbers and the torus is called resonant.

The dynamics however change drastically when introducing a third body, where chaotic dynamics become possible. While historically Poincaré's work on the three-body problem laid down the foundation for chaos theory [1], the problem is still a topic of active research up until today [2–4]. In phase space, the existence of a non-integrable perturbation leads to a destruction of torus structures according to the Kolmogorov-Arnold-Moser theorem (KAM theorem) [5–7]. It states that most of the tori survive a small perturbation leading only to a deformation of the tori. Increasing the strength of the perturbation leads to a break-up of more and more torus structures resulting in chaotic behavior. For two-dimensional systems, this can be conveniently presented using a Poincaré surface of section (PSOS). Here, the chaotic regions result in stochastic areas in the PSOS. Periodic orbits appear as fixed points in accordance with the Poincaré-Birkhoff theorem [8–10], with an equal number of elliptical (stable) and hyperbolic (unstable) fixed points. The stability properties of these orbits can be quantified through the stability matrix and its eigenvalues, which are linked to the Lyapunov exponents. The Lyapunov exponents provide a quantitative measure for the instability of chaotic trajectories. For three-dimensional motion, the PSOS is no longer suitable to depict the emerging phase space structure. However, other geometrical properties

of the orbits can be used to characterize the dynamics. An example is the Lagrangian descriptor (LD), which measures the arc length of an orbit for a given time interval and starting configuration [11, 12]. Recently it has been shown that an indicator based on the second derivatives of the LD provides a powerful tool for revealing the global phase space structures of a dynamical system [13].

With the end of the 19th century it became evident that classical physics needed to be expanded to describe the phenomena observed in microscopic systems. One case where this becomes visible is when looking at atomic spectra, where the energy appears quantized at distinct lines. The first quantitative description was introduced by Balmer in 1885 providing a formula correctly reproducing the lines in the range of visible light for the hydrogen atom [14]. This formula was expanded by Rydberg only three years later and published in the following years [15], predicting the existence of other series in addition to the Balmer series which only includes transition to $n_1 = 2$. The Rydberg formula was confirmed after the Lyman series for $n_1 = 1$ [16] and the Paschen series for $n_1 = 3$ [17] were found.

The first theoretical explanation for the hydrogenic spectra was given by Bohr's atomic model [18]. He postulated that the electron can only move on certain classical orbits fulfilling a quantization condition for the angular momentum. From this model one can derive the Rydberg formula which to this point was only given empirically. This model was further expanded by Sommerfeld giving a quantization condition for every coordinate, allowing now also to include ellipses instead of only circular orbits used first in the Bohr model [19]. With this procedure one obtains three quantum numbers which can be assigned to the corresponding ellipse providing an intuitive understanding of the periodic table.

The hydrogen-like model is also appropriate to deal with atoms with one highly excited electron. For these Rydberg atoms the distance of the electron to the core and the other electrons is large, meaning that the nucleus and the remaining electrons can approximately be treated as one entity with net charge $+e$. While the hydrogen atom only exhibits one peak for a given principle quantum number n , other atoms with one shell electron show deviations from this behavior where a splitting for different angular momenta l becomes apparent. In the classical picture this can be understood when looking at the corresponding orbits. For states with low angular momentum quantum numbers l , the orbits of the excited electron come closer to the core, which in this region can no longer be screened by the other electrons. Thus, the excited electron experiences a stronger Coulomb interaction, lowering the binding energy. To capture these deviations from the hydrogen spectrum, Rydberg himself introduced a correction scheme to modify the expressions for the energy in his publication from 1890 [15]. This can be achieved by subtracting a non-integer quantum defect $\delta_{n,l}$ from the principle quantum number $n^* = n - \delta_{n,l}$ and substituting n by n^* in the Rydberg formula. As the screening of the core becomes better for increasing angular momentum quantum number the quantum defects typically decrease with increasing l .

The methods of old quantum mechanics however fail already for helium when an

additional electron is introduced. An insight concerning this problem was gained by Einstein, who further specified the quantization condition by Sommerfeld only allowing the coordinate systems resulting in action angle variables [20]. As the helium atom constitutes a three-body problem, the dynamics become chaotic, leading to a destruction of torus structures and thus the inapplicability of the quantization procedure.

This problem was resolved with the introduction of modern quantum mechanics where the dynamical object is now no longer given by classical orbits but rather a complex probability amplitude, i.e. the wave function ψ . The dynamics of the wave function is then governed by the Schrödinger equation. A theoretical treatment correctly reproduces the spectrum of helium, however, the exact quantum computations do not provide any intuitive physical interpretation. Similar is true for other complex systems, a prominent example being the hydrogen atom in a magnetic field, which is a quantum system, whose classical analogue shows a transition from regular to chaotic dynamics, and whose spectra in the non-perturbative regime can hardly be explained intuitively using a pure quantum mechanical terminology.

An intuitive interpretation can be obtained by means of semiclassical methods, linking the quantum spectra to periodic orbits and their properties. For integrable systems the basis is given by the quantization condition introduced by Einstein. A semiclassical treatment of the wave functions reveals that one has also to account for some singular points when performing a semiclassical torus quantization. To do this one has to add the Maslov index which counts the number of reflections and turning points on the independent paths on the torus in the quantization condition for the corresponding action variable. This treatment first introduced by Keller in 1958, is also termed Einstein-Brillouin-Keller method (EBK method) [20–22]. A formula for the density was later derived by Berry and Tabor [23, 24]. In the Berry-Tabor formula, classical periodic orbits provide sinusoidal fluctuations characterized by the periodic orbit parameters. A similar formula for non-integrable systems is due to Gutzwiller [25–27]. Instead of families of orbits belonging to the same torus in the integrable case, Gutzwiller’s trace formula takes into account the isolated periodic orbits in the non-integrable system. These methods provide the basis for the study of quantum chaos, allowing for a vivid description of quantum system with underlying classically chaotic dynamics, e.g., the helium atom [28–30] or the hydrogen atom in external fields [31–35].

In this thesis we now want to provide a semiclassical interpretation for excitons in cuprous oxide. The theoretical foundations for the description of excitons have been formulated by Frenkel [36–38], Peierls [39] and Wannier [40]. Here, we focus on Wannier excitons, which typically appear in semiconductors like cuprous oxide [41]. These excitons can be formed when an electron is excited from the valence band into the conduction band of a semiconductor. The missing electron in the valence band can be treated as a positively charged quasiparticle, the hole. Due to the Coulomb interaction electrons and holes can then form hydrogen-like bound states called excitons. Cuprous oxide takes a special role in exciton physics. On the one hand, excitons have been discovered in this material first [42], on the other hand, compared to other semiconductors, where only low

principle quantum numbers are experimentally accessible, the group by Manfred Bayer in Dortmund was able to show the existence of a Rydberg series up to high principle quantum numbers until $n = 25$ for cuprous oxide [43]. Nowadays, this series of P states can be even traced up to $n = 30$ [44]. The spectra of cuprous oxide differ from an ideal hydrogen-like behavior exhibiting a splitting of different angular momentum states and even a hyper-fine splitting for different l -manifolds [45]. These deviations from the Rydberg series are due to the complex band-structure which has to take into account the cubic O_h symmetry of the system [45–48]. A theoretical model has been achieved in the Luttinger-Kohn theory [49–51], where a quasispin $I = 1$ is introduced. The coupling between the quasispin and the hole spin S_h results in a splitting of the valence band and leads to a yellow [43, 44, 47] and green exciton series [44, 47, 52, 53] with light and heavy holes.

The theoretical treatment of the full model allowed to incorporate the quantum defect concept for additional angular momentum states in analogy to quantum defects in atoms [47, 48]. For the yellow exciton series the quantum defects $\delta_{n,l}$ are positive and grow with decreasing angular momentum l . They also slightly grow as function of n until saturating for large n .

While experimental and theoretical works have further advanced since [53–111], an intuitive interpretation of excitonic spectra in terms of classical exciton orbits beyond the hydrogen-like model was still missing before the start of this thesis. After first approaches modeling the spin-degrees of freedom in a classical framework following the Landau-Lifschitz-Gilbert equation failed [112, 113], we were able to develop an adiabatic approach treating the spin degrees of freedom in a quantum mechanical framework while the dynamics in coordinate space are treated classically [114, 115]. In this approach, the additional band structure corrections are accounted for via energy surfaces in momentum space. These energy surfaces carry the cubic symmetry of the system and can be assigned directly to the different exciton series.

Due to the symmetry reduction compared to the hydrogen-like case the dynamics is no longer integrable allowing for the possibility of chaotic dynamics. In a quantum mechanical framework the existence of quantum chaos has been demonstrated for magnetoexcitons in cuprous oxide which break all antiunitary symmetries [59, 61, 62, 64, 116, 117]. Calculating classical exciton orbits by integrating Hamilton's equations of motion we were able to demonstrate the existence of classically chaotic phase space regions even without the application of external fields [115, 118, 119]. The green exciton series in particular exhibits large chaotic regions in phase space, while for the yellow exciton series large regular regions exist.

The connection between classical orbits and the quantum spectra is given through semiclassical formulas for the density of states. The semiclassical formulas become particularly easy when the system exhibits a scaling property, where the system in the scaled units no longer depends on the energy (or another external parameter) and the action scales linearly with the scaling parameter [120]. The density of states can then be understood as a Fourier series in the scaled action. This results in delta peaks at the

scaled action of periodic orbits in the Fourier transform quantum recurrence spectra. To recover such a scaling property for excitons in cuprous oxide we employ a scaling technique to the spin-orbit coupling. While this procedure is not possible in an experiment, a tunable spin-orbit coupling strength has already been used for the theoretical investigation of the exchange interaction in the yellow exciton series [89]. The existence of a classical dynamics can then be directly proven by assigning classical orbits to the peaks in quantum recurrence spectra [118, 121].

Quantum defects $\delta_{n,l}$ with a splitting of the different angular momentum states can appear in systems with spherical symmetry. While the full model for excitons in cuprous oxide has the cubic O_h symmetry and the material parameters can be obtained from band structure calculations [47, 48], earlier works used a spherical model where the material parameters were obtained by a fit to experimental spectra [122]. Here, the material parameters characterizing the strength of the spherical contributions deviate strongly between the different methods. Starting from the full model with cubic symmetry we perform a spherical average using an efficient spherical design [123] to obtain a spherical model. This then shows good agreement with the spherical model from the literature [122] providing a link between the previously contradicting models. Extracting the quantum defects using the semiclassical EBK method we find a good agreement with quantum mechanical results in the literature [47, 48, 66].

This thesis is organized as follows. Chapter 2 gives a short overview over the basic concepts of nonlinear dynamics in Hamiltonian systems. In addition, different techniques for sampling the phase space of such systems are introduced. On the basis of classical dynamics we review the key concepts of semiclassical physics in chapter 3, introducing the EBK method, the Berry-Tabor formula as well as Gutzwiller's trace formula. In chapter 4 we give a brief introduction to solid state physics resulting in the quantum mechanical description of excitons in cuprous oxide. Following this, we develop the adiabatic approach for the exciton dynamics in chapter 5. Here, we derive analytical expressions of the energy surfaces and discuss the symmetries of the cuprous oxide crystal. The following chapters present our results for excitons in cuprous oxide. Chapter 6 discusses the classical dynamics of the yellow exciton series. The existence of a classical exciton dynamics in the quantum spectra is demonstrated in chapter 7 by the application of semiclassical theory and a scaling technique. In chapter 8 we develop a spherical model starting from the model with full cubic symmetry. On this basis we extract the quantum defects of the yellow series. This is followed by a comparison of the dynamics of the yellow and the two distinct green exciton series in chapter 9. We observe large chaotic regions in phase space. Finally, we close by giving a summary and outlook in chapter 10.

1. Introduction

Essential parts of this thesis have been published in Refs. [115, 118, 121],

- *Classical and semiclassical description of Rydberg excitons in cuprous oxide*, J. Ertl, P. Rommel, M. Mom, J. Main, M. Bayer, Phys. Rev. B, **101**, 241201(R) (2020)
- *Signatures of Exciton Orbits in Quantum Mechanical Recurrence Spectra of Cu_2O* , J. Ertl, M. Marquardt, M. Schumacher, P. Rommel, J. Main, M. Bayer, Phys. Rev. Lett., **129**, 067401 (2022)
- *Classical dynamics and semiclassical analysis of excitons in cuprous oxide*, J. Ertl, M. Marquardt, M. Schumacher, P. Rommel, J. Main, M. Bayer, Phys. Rev. B, **109**, 165203 (2024)

submitted for publication [119, 124],

- *Rydberg excitons in cuprous oxide: A two-particle system with classical chaos*, J. Ertl, S. Rentschler, J. Main, Chaos, submitted
- *The energy level spectrum of the yellow exciton series in cuprous oxide*, J. Heckötter, A. Farenbruch, D. Fröhlich, M. Aßmann, D. R. Yakovlev, M. Bayer, M. A. Semina, M. M. Glazov, P. Rommel, J. Ertl, J. Main, H. Stolz, Physics Reports, submitted

or are in preparation for publication,

- *Quantum defects of Rydberg excitons in cuprous oxide: A semiclassical picture*, J. Ertl, J. Main, in preparation.

2

Nonlinear dynamics in Hamiltonian systems

In this chapter we give a brief introduction to the theoretical foundations of nonlinear dynamics and chaos in Hamiltonian systems. The presentation is mainly based on Refs. [125, 126]. A more detailed introduction can be found for example in Refs. [27, 126–131].

2.1 Conservative Hamiltonian systems

Here we want to discuss the dynamics of autonomous Hamiltonian systems

$$H(\mathbf{r}, \mathbf{p}) = E, \quad (2.1)$$

where the Hamilton function has no explicit time dependence and thus provides the energy E as a constant of motion. The classical dynamics of such a system with N degrees of freedom can be calculated by integrating Hamilton's equations of motion

$$\dot{r}_i = \frac{\partial H}{\partial p_i}, \quad \dot{p}_i = -\frac{\partial H}{\partial r_i}, \quad (2.2)$$

with $i = 1, 2, \dots, N$. This can be conveniently summarized by introducing the phase space vector

$$\boldsymbol{\gamma} = \begin{pmatrix} \mathbf{r} \\ \mathbf{p} \end{pmatrix}. \quad (2.3)$$

Hamilton's equations of motion then read

$$\dot{\boldsymbol{\gamma}} = \mathbf{J} \frac{\partial H}{\partial \boldsymbol{\gamma}}, \quad (2.4)$$

where \mathbf{J} is the symplectic matrix

$$\mathbf{J} = \begin{pmatrix} 0 & \mathbb{1} \\ -\mathbb{1} & 0 \end{pmatrix}, \quad (2.5)$$

with the $N \times N$ identity matrix $\mathbb{1}$ and 0 the $N \times N$ matrix containing only zeroes. In general Hamilton's equations of motion provide a set of $2N$ coupled differential equations for a system with N degrees of freedom, which typically are directly solvable only for a small number of systems. Sometimes the problem can be simplified by introducing new coordinates $\mathbf{r}, \mathbf{p} \rightarrow \mathbf{R}(\mathbf{r}, \mathbf{p}), \mathbf{P}(\mathbf{r}, \mathbf{p})$. To maintain the structure of Hamilton's equations of motion this has to be done by using a canonical transformation, which can be realized using a suited generating function, e.g., $F_2 = S(\mathbf{r}, \mathbf{P})$. The generating function then connects old and new variables by

$$\begin{aligned} p_i &= \frac{\partial S}{\partial r_i}, \\ R_i &= \frac{\partial S}{\partial P_i}. \end{aligned} \quad (2.6)$$

Inserting this back into the Hamiltonian one arrives at the Hamilton-Jacobi equation

$$H\left(\mathbf{r}, \frac{\partial S}{\partial \mathbf{r}}\right) = E, \quad (2.7)$$

which is a partial differential equation, where the solution provides the generating function S .

2.2 | Integrable systems

The solution of the equations of motion becomes particularly easy when the Hamilton function in the new coordinates no longer depends on the coordinates \mathbf{R} , i.e., $H = H(\mathbf{P})$. From Hamilton's equations of motions

$$\dot{R}_i = \frac{\partial H}{\partial P_i}, \quad \dot{P}_i = -\frac{\partial H}{\partial R_i} = 0, \quad (2.8)$$

it follows that the generalized momenta now provide a set of constants of motion

$$P_i = \text{const.} \quad (2.9)$$

If for a system the number of independent constants of motion is the same as the number of degrees of freedom the system is called integrable. The differential for the generating function S is then given by

$$dS = \sum_i \frac{\partial S}{\partial r_i} dr_i + \frac{\partial S}{\partial P_i} dP_i = \sum_i p_i dr_i, \quad (2.10)$$

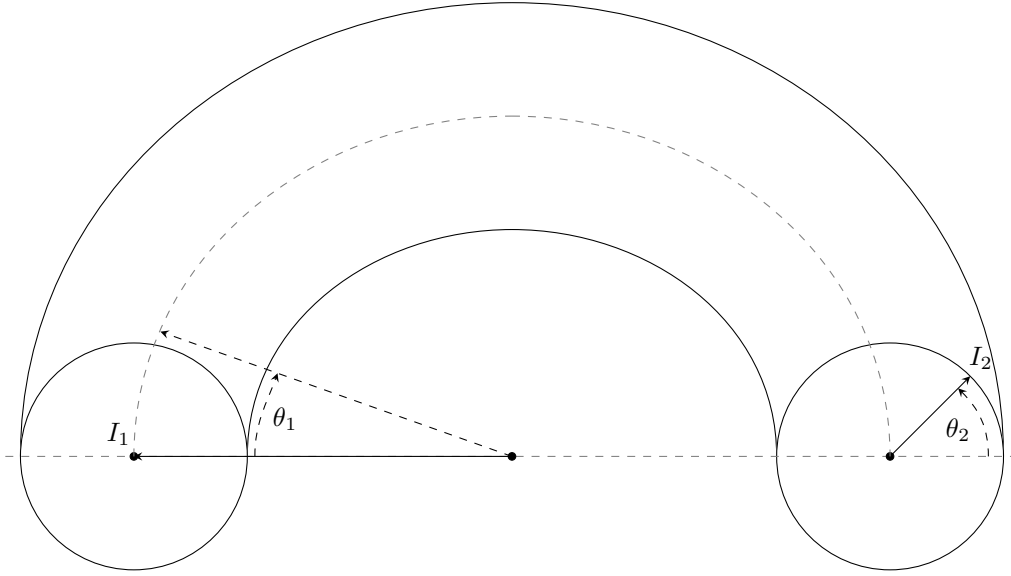


Figure 2.1.: Visualization for the action angle variables on a two-dimensional torus.

allowing to identify

$$S = \int \mathbf{p} d\mathbf{r} \quad (2.11)$$

as the action of the particle. The corresponding coordinates then have a linear dependence on time

$$R_i(t) = \alpha_i t + R_i(0), \quad (2.12)$$

with $\alpha_i = \frac{\partial H}{\partial P_i}$. If the system is confined, the motion along the independent paths becomes periodic. The resulting phase space takes the shape of an N torus. This is visualized in figure 2.1 for a two-dimensional system. In such systems one can introduce action angle variables $\mathbf{I}, \boldsymbol{\theta}$ where the action variables

$$I_i = \frac{1}{2\pi} \oint_{\mathcal{C}_i} \mathbf{p} d\mathbf{r} \quad (2.13)$$

are the constants of motion obtained by integrating along the independent paths on the torus \mathcal{C}_i characterized by the corresponding angles θ_i going from 0 to 2π . Since action variables provide constants of motion the corresponding angles again show the linear dependence on time

$$\theta_i = \omega_i t, \quad (2.14)$$

with frequencies

$$\omega_i = \frac{\partial H}{\partial I_i}. \quad (2.15)$$

If all ratios ω_i/ω_j for the different frequencies on the torus are given by rational numbers the corresponding orbit becomes periodic and can be characterized by a set of integer winding numbers M_i , which count the number of cycles on each of the tori \mathcal{C}_i until the orbit returns to its initial position. The periodic orbits are located on resonant tori.

2.3 Near-integrable systems

We now want to discuss the influence of a small perturbation εH_1 to an integrable system H_0 . The Hamilton function of the system is given by

$$H(\mathbf{I}, \boldsymbol{\theta}) = H_0(\mathbf{I}) + \varepsilon H_1(\mathbf{I}, \boldsymbol{\theta}), \quad (2.16)$$

where \mathbf{I} and $\boldsymbol{\theta}$ are the action angle variables of the unperturbed system. The full system can then be treated perturbatively to find new action angle variables $\tilde{\mathbf{I}}, \tilde{\boldsymbol{\theta}}$ for the full system such that the Hamilton function only depends on the new action variables $H = H(\tilde{\mathbf{I}})$. For this one develops the perturbation into a Fourier series

$$H_1(\mathbf{I}, \boldsymbol{\theta}) = \sum_{m \neq 0} H_{1,m}(\mathbf{I}) e^{im\boldsymbol{\theta}}, \quad (2.17)$$

with $m_i \in \mathbb{Z}$. Up to first order in ε the generating function for this system is then given by [126]

$$S(\tilde{\mathbf{I}}, \boldsymbol{\theta}) = \tilde{\mathbf{I}}\boldsymbol{\theta} + i\varepsilon \sum_{m \neq 0} \frac{H_{1,m}(\tilde{\mathbf{I}})}{m\boldsymbol{\omega}(\tilde{\mathbf{I}})} e^{im\boldsymbol{\theta}}. \quad (2.18)$$

In the scope of the perturbation series the new action variables are then constants of motion for the perturbed system to first order. While in principle the perturbation series can be continued to higher orders in ε , the question remains whether the perturbation series converges. It becomes immediately clear that series diverges for resonant tori where $m\boldsymbol{\omega} = 0$.

2.3.1 KAM theorem

For non-resonant tori the question whether they survive a perturbation is answered by the KAM theorem after Kolmogorov, Arnold, and Moser [5–7]. In short, it states that for small enough values of ε a given non-resonant torus with the frequency $\boldsymbol{\omega}$ survives the perturbation, where the action angle variables of the unperturbed system $\mathbf{I}, \boldsymbol{\theta}$ go to new values $\tilde{\mathbf{I}}, \tilde{\boldsymbol{\theta}}$, meaning that the torus gets slightly deformed compared to the unperturbed case. For the theorem to be applicable, the following conditions must be fulfilled [126, 128, 132, 133]

- The $\boldsymbol{\omega}$ should be linearly independent,

$$\det \frac{\partial \omega_i}{\partial \tilde{I}_j} \neq 0. \quad (2.19)$$

- The perturbation needs to be a sufficiently smooth function of \mathbf{I} and $\boldsymbol{\theta}$.
- The frequency needs to be sufficiently different compared to rationals

$$|\mathbf{m}\boldsymbol{\omega}| \geq \frac{K(\varepsilon)}{(\sum_i |m_i|)^\tau} \quad (2.20)$$

with $K, \tau > 0$. K goes to zero in the unperturbed case and grows with ε . Since the left-hand side of equation (2.20) is constant for a given $\boldsymbol{\omega}$ more and more tori violate the condition of sufficient irrationality for increasing ε resulting in a break-up of the torus structures.

2.3.2 Poincaré-Birkhoff theorem

We will now discuss the case of resonant tori $\mathbf{m}\boldsymbol{\omega} = 0$. In this case the perturbation series (2.18) diverges and the corresponding tori break up immediately when a small perturbation is applied. In the two-dimensional case the Poincaré-Birkhoff [8–10] theorem provides the basis for understanding how this break-up takes place. It states that an area preserving map on an annulus which rotates the different boundaries in opposite directions has at least two fixed points.

In an integrable Hamiltonian system such a map can be constructed by introducing a surface of section obtained by setting $\theta_2 = 0$. An orbit on the corresponding 2 torus passes through $\theta_2 = 0$ after times

$$t_n = \frac{2\pi n}{\omega_2}, \quad (2.21)$$

with $n \in \mathbb{N}$. The other angle $\theta_{1,n}$ is then given by

$$\theta_{1,n} = \frac{\omega_1}{\omega_2} 2\pi n. \quad (2.22)$$

The action variable is a constant of motion and thus remains unchanged. For a resonant torus the ratio ω_1/ω_2 is given by a rational number

$$\frac{\omega_1}{\omega_2} = \frac{p}{q}, \quad (2.23)$$

with $p, q \in \mathbb{N}$. If $n = q$ then the mapping (2.22) keeps the point on the torus unchanged. We now consider $\boldsymbol{\omega}$ to be a smooth, monotonic function of \mathbf{I} . In proximity of the resonant torus we can find two non-resonant tori with ω_{1+} and ω_{1-} which enclose the

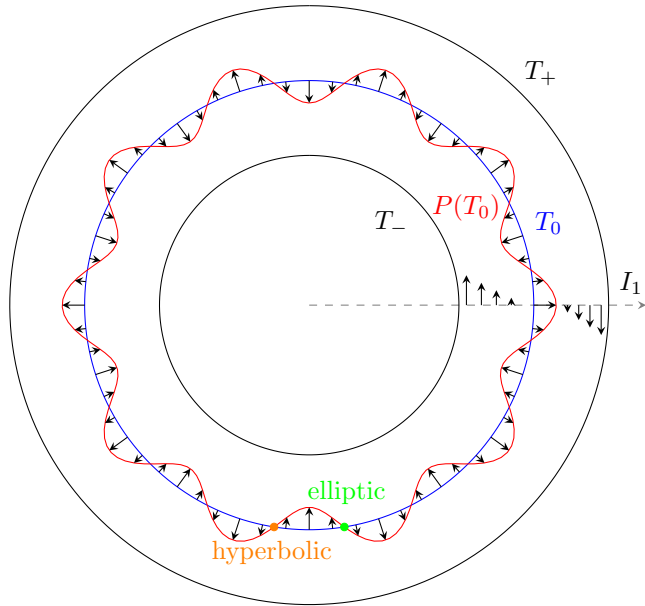


Figure 2.2.: The non-resonant tori T_+ and T_- with frequencies ω_{1+} and ω_{1-} survive a small perturbation. Due to the monotonic behavior of ω_1 between T_+ and T_- there exists a point in between that does not get rotated by the map T_0 indicated by the blue line. The map P however changes the value of I_1 leading to the red curve $P(T_0)$. Due to the area preserving property of Hamiltonian systems there exists an even number of fixed points of $P(T_0)$. Their behavior can be examined following the flow lines of P , resulting in elliptic and hyperbolic fixed points. An example is marked in green and orange, respectively.

resonant tori in the surface of section, where $\omega_{1-} < \omega_1 < \omega_{1+}$. The mapping (2.22) will then rotate the points on the two non-resonant tori in opposite directions.

With the onset of a small perturbation the resonant torus breaks up while the non-resonant tori survive a small perturbation in accordance with the KAM theorem. Due to the monotonic behavior of ω_1 there must exist a point between the two non-resonant tori that does not get rotated by the map (2.22), however, the action variable of the unperturbed system I_1 is no longer a constant of motion, meaning that the mapping changes the value of I_1 to I_1' . Due to Liouville's theorem [134] the area of neighboring phase space trajectories has to be conserved. This means that the curve of points that are not rotated and its image have to intersect, resulting in an even number of fixed points (at minimum two). When considering the sense of rotation of the bordering tori as well as the alternating behavior in the shift of the action variable, one observes that the fixed points alternate between elliptical and hyperbolic behavior. The situation is sketched in figure 2.2.

2.4 Methods to sample phase space

Finally, we want to introduce different methods for analyzing the classical dynamics of Hamiltonian systems. For two-dimensional systems the Poincaré surfaces of section is a useful tool for analyzing the dynamics. For the analysis of higher-dimensional systems we introduce the stability matrix and the Lyapunov exponents as well as Lagrangian descriptors.

2.4.1 Poincaré surfaces of section

In case of a classical dynamics in a two-dimensional plane with coordinates, e.g., x and y the corresponding four-dimensional phase space can be analyzed by using a PSOS. Therefore, we choose the y axis as 1D-sectional plane and denote the coordinate y and momentum p_y whenever an orbit passes the sectional plane. By choosing, e.g., $x = 0$ the remaining momentum p_x is given by the conservation of energy. In the integrable case action angle variables can be constructed, and the motion is confined to tori, leading to a completely regular phase space. When adding a small non-integrable perturbation the KAM theorem states that almost all non-resonant tori survive the perturbation as discussed in section 2.3.1. When the perturbation grows more and more tori start to break up, leading to stochastic areas in the PSOS. According to the Poincaré-Birkhoff theorem, presented in section 2.3.2, the resonant tori break up leading to an equal number of elliptic and hyperbolic fixed points in the PSOS and eventually to the onset of chaos.

2.4.2 Stability of orbits

A more quantitative measure for the stability of individual trajectories can be obtained by investigating Lyapunov exponents of orbits, which describe the rate with which a deviation between neighboring trajectories grows in the corresponding direction. For periodic orbits with period T the Lyapunov exponent Λ_i is given by

$$\Lambda_i = \frac{1}{T} \ln(|\lambda_i(0, T)|), \quad (2.24)$$

with $\lambda_i(0, T)$ the eigenvalues of the stability matrix $\mathbf{M}(0, T)$, which is a linearization for the time evolution for deviations of the phase-space vector $\boldsymbol{\gamma} = (\mathbf{r}, \mathbf{p})^\top$, i.e.

$$\Delta\boldsymbol{\gamma}(T) = \mathbf{M}(0, T)\Delta\boldsymbol{\gamma}(0). \quad (2.25)$$

For eigenvalues $|\lambda_i(0, T)| = 1$ the perturbed orbit stays in the vicinity of its periodic counterpart, meaning a Lyapunov exponent $\Lambda_i = 0$ indicates a stable direction. Lyapunov exponents $\Lambda_i > 0$ correspond to an unstable direction. To obtain the Lyapunov

exponents we integrate the stability matrix along the periodic orbit. For Hamiltonian systems its equation of motion is given by

$$\frac{d}{dt}\mathbf{M} = \mathbf{J} \frac{\partial^2 H}{\partial \boldsymbol{\gamma}^2} \mathbf{M}, \quad (2.26)$$

with the symplectic matrix (2.5) and the initial configuration of the stability matrix

$$\mathbf{M}(t = 0) = \begin{pmatrix} \mathbb{1} & 0 \\ 0 & \mathbb{1} \end{pmatrix}. \quad (2.27)$$

2.4.3 Lagrangian descriptors

While the dynamics in a two-dimensional plane can be visualized through a PSOS, this method is no longer well suited for the analysis of fully three-dimensional or even higher-dimensional motion. One possible method to gain a better understanding of the phase space is to investigate the dynamics using an LD [11, 12]. It is defined as the arc length of a trajectory with given initial conditions $\boldsymbol{\gamma}_0$

$$\text{LD}(\boldsymbol{\gamma}_0, T) = \int_0^T \|\mathbf{v}\| dt, \quad (2.28)$$

in a given time interval $[0, T]$. The general idea is that in regular regions, where a small change of the initial conditions leads to a qualitatively similar picture, the LD also will not change much, whereas one would expect stronger changes when entering a phase space region with qualitatively different behavior. While this already provides a useful tool for obtaining an overview over the general global phase space structures, the challenge of this approach is that locally the detailed phase space structures cannot be well resolved, when the arc length has a strong dependence on the initial conditions of the orbit. To gain a better resolution of the local fluctuations, recently an indicator for chaos based on the second derivatives of the LD with respect to the initial conditions $\boldsymbol{\gamma}_{0i}$ has been introduced [13], which reads

$$\Delta\text{LD} = \sum_{i=1}^N \left| \frac{\partial^2 \text{LD}}{\partial \boldsymbol{\gamma}_{0i}^2} \right|. \quad (2.29)$$

Stochastic regions with large values of the ΔLD indicator reveal stochastic dynamics, while low values with smooth behavior indicate regular phase space regions.

3

Semiclassical description of Hamiltonian systems

At the end of the 19th century it became evident that classical dynamics are incapable of describing all the phenomena prevalent in microscopic systems. This was resolved by the introduction of quantum mechanics. The connection of quantum mechanics and classical physics is given by semiclassical approaches. In this chapter we introduce the foundations of semiclassical physics relevant for our purposes. The presentation follows Ref. [125]. A detailed introduction can be found e.g. in Refs. [27, 126, 130, 135].

3.1 Integrable systems

The first explanation for quantum properties of a system were introduced through Bohr's atomic model [18]. He postulated that the electron can only move on circular classical orbits fulfilling a quantization condition for the angular momentum

$$L = n\hbar \quad (3.1)$$

with $n \in \mathbb{N}$. From this model one can derive the Rydberg formula which to this point was only given empirically. This model was further expanded by Sommerfeld giving a quantization condition for every coordinate

$$\oint p_i dr_i = n_i \hbar. \quad (3.2)$$

Sommerfeld used spherical coordinates resulting in a description by a radial quantum number n_r , an azimuthal quantum number l , and magnetic quantum number m . This allows now also to include ellipses instead of only circular orbits used first in the Bohr model [19].

However, Sommerfeld's quantization scheme was dependent on the chosen coordinate system. This was resolved by Einstein [20] who realized that the action variables of the

3. Semiclassical description of Hamiltonian systems

invariant tori should be quantized

$$I_i = \frac{1}{2\pi} \oint_{c_i} \mathbf{p} d\mathbf{r} = n_i \hbar. \quad (3.3)$$

This also led him to the realization that the approach would break down for non-integrable systems and a different treatment needs to be developed in this case.

The works by Bohr, Sommerfeld, and Einstein preceded the modern formulation of quantum mechanics where the particles are described by a wave function. A semiclassical treatment reveals that additional modifications become necessary. As a first step we want to discuss the WKB method (Wenzel, Kramer, Brillouin) [136–138]. The fundamental description of modern quantum mechanics is given by the Schrödinger equation

$$H\psi = E\psi. \quad (3.4)$$

Here, we consider a one-dimensional system with Hamilton operator

$$H = -\frac{\hbar^2}{2m} \partial_x^2 + V(x). \quad (3.5)$$

We now use an ansatz

$$\psi(x) = A(x) e^{iS(x)/\hbar}. \quad (3.6)$$

Inserting this into the Schrödinger equation results in an equation for the real part

$$\left(\frac{\partial S}{\partial x} \right)^2 - 2m(E - V(x)) = \frac{\hbar^2}{A} \frac{\partial^2 A}{\partial x^2}, \quad (3.7)$$

and an imaginary part

$$2 \frac{\partial A}{\partial x} \frac{\partial S}{\partial x} + A \frac{\partial^2 S}{\partial x^2} = 0. \quad (3.8)$$

Equation (3.8) can be solved for A resulting in

$$A = c \left(\left| \frac{\partial S}{\partial x} \right| \right)^{-1/2}, \quad (3.9)$$

with a constant c . In the limit $\hbar \rightarrow 0$ the real part (3.7) is simply given by the Hamilton-Jacobi equation, with the solution

$$S(x) = \pm \int_{x_0}^x \sqrt{2m(E - V(x'))} dx' = \pm \int_{x_0}^x p dx'. \quad (3.10)$$

The region where $E - V(x') \geq 0$ is the classically allowed region where $S(x)$ takes real values while areas with $E - V(x') < 0$ are classically forbidden. In the forbidden region S becomes imaginary, leading to an exponential decay of the wave function, allowing the

particle to tunnel into the forbidden region. The wave function in the classically allowed region takes the form

$$\psi = \frac{C}{\sqrt{|p|}} \sin\left(\frac{1}{\hbar} \int_{x_0}^x p dx' + \phi\right), \quad (3.11)$$

with a constant C and a constant phase ϕ . Let us now consider bound motion between two classical turning points $a < x < b$. At the turning points $|p| = 0$ and the wave function diverges. We thus want to take a closer look at the situation at the turning points. It can be shown that ϕ has to take the value $\phi = \pi/4$ when requiring continuity of the wave function ψ and its derivative ψ' at the transition from the classically allowed to the classically forbidden region at a turning point a

$$\psi_a = \frac{A}{\sqrt{|p|}} \sin\left(\frac{1}{\hbar} \int_a^x p dx' + \frac{\pi}{4}\right), \quad (3.12)$$

with a constant A . On the other hand we could have also chosen the other turning point b as starting point of the integration x_0 , the wave function would then take the form

$$\psi_b = \frac{B}{\sqrt{|p|}} \sin\left(\frac{1}{\hbar} \int_b^x p dx' - \frac{\pi}{4}\right) = \frac{-B}{\sqrt{|p|}} \sin\left(\frac{1}{\hbar} \int_x^b p dx' + \frac{\pi}{4}\right), \quad (3.13)$$

with a constant B . Since the wave function has to be unique both expressions should be the same. To achieve this we divide the integral

$$\int_a^x p dx' = \int_a^b p dx' + \int_b^x p dx' \quad (3.14)$$

into a part going from turning point a to turning point b and then back from b to x . If we interchange the boundaries of the integrals and pull the minus sign out of the sin function in ψ_a we have accumulated a phase loss of $\pi/2$ by passing through the turning point in b . Setting $\psi_a = \psi_b$ results in the conditions $A = B(-1)^n$ and

$$\int_b^a p dx' - \frac{\pi}{2} = \pi n \quad (3.15)$$

with $n \in \mathbb{N}_0$. Considering a closed orbit this can be rewritten as

$$\oint p dx' = 2\pi \left(n + \frac{1}{2}\right). \quad (3.16)$$

The additional summand $1/2$ was missing in the quantization conditions of the old quantum mechanics. As we have seen it is due to the topology of the orbit, accounting for the turning points passed along the way. The WKB method is however only suitable for one-dimensional systems.

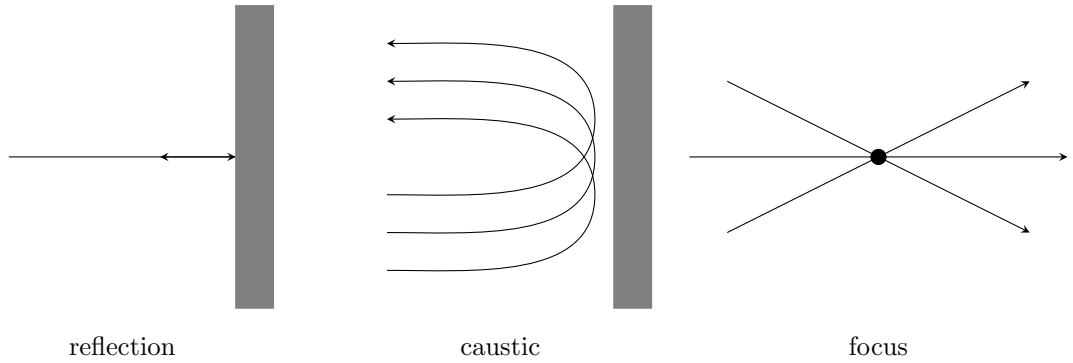


Figure 3.1.: Sketch of the different singular points. Gray areas indicate classically forbidden regions.

For higher-dimensional systems a semiclassical quantization can be achieved by applying the Einstein-Brillouin-Keller (EBK) method [20–22]. This approach was first introduced by Keller in 1958 [21] who extended the quantization scheme (3.3) of Einstein

$$I_i = \frac{1}{2\pi} \oint_{C_i} \mathbf{p} d\mathbf{r} = \hbar \left(n_i + \frac{\alpha_i}{4} \right). \quad (3.17)$$

In addition to classical turning points additional singular points where the semiclassical wave function diverges can appear in higher dimensions. In addition to the reflection at a potential barrier there are caustics, which provide a border for a set of trajectories, as well as focal points, which are points in which a set of trajectories intersect. The singular behavior of the wave function at these points can be omitted by going to momentum space. The different singular points are sketched in Fig. 3.1. As Maslov has shown this however leads to a phase loss of $\pi/2$ [139]. The Maslov indices α_i count the number of singular points through which the orbit passes, these then need to be accounted for in the quantization condition. The energy spectrum can be computed with the help of the Hamilton function

$$E(\mathbf{n}) = H \left(\mathbf{I} = \hbar \left(\mathbf{n} + \frac{\boldsymbol{\alpha}}{4} \right) \right). \quad (3.18)$$

Now we want to find a semiclassical expression for the quantum mechanical density of states

$$d(E) = \sum_{\mathbf{n}} \delta(E - E(\mathbf{n})). \quad (3.19)$$

First we use the Poisson formula [135, 140]

$$\sum_{n=0}^{\infty} f(n) = \sum_{M=-\infty}^{\infty} \int_0^{\infty} f(n) \exp(2\pi i M n) dn + \frac{1}{2} f(0), \quad (3.20)$$

for each of the n_i . The terms including contributions for the last term in Eq. (3.20) are neglected, these include among others corrections of higher order in \hbar [135]. The relevant part is

$$d(E) = \sum_{\mathbf{M}} \int_0^\infty d^N \mathbf{n} \delta(E - E(\mathbf{n})) \exp[2\pi i \mathbf{M} \mathbf{n}], \quad (3.21)$$

which can be expressed by action variables using equation (3.17)

$$d(E) = \frac{1}{\hbar^N} \sum_{\mathbf{M}} \exp\left[-\frac{\pi}{2} i \mathbf{M} \boldsymbol{\alpha}\right] \int_{\hbar \boldsymbol{\alpha}_i/4}^\infty d^N \mathbf{I} \delta(E - E(\mathbf{I})) \exp[2\pi i \mathbf{M} \mathbf{I} / \hbar]. \quad (3.22)$$

The term at $\mathbf{M} = 0$ gives the Thomas-Fermi term [135] when considering that the lower integral limits goes to 0 for $\hbar \rightarrow 0$,

$$\bar{d}(E) = \frac{1}{(2\pi\hbar)^N} \int \int d\mathbf{p} d\mathbf{r} \delta(E - H(\mathbf{p}, \mathbf{r})), \quad (3.23)$$

which provides an average of the density of states. The other terms give a fluctuating part $\tilde{d}(E)$. The full expression for the semiclassical density of states for integrable system was first derived by Berry and Tabor [23, 24]. They evaluated the additional terms after using appropriate coordinates and applying a stationary phase approximation when evaluating the integrals. The stationary-phase condition only allows for periodic orbits with winding numbers \mathbf{M} providing sinusoidal fluctuation to the Berry-Tabor formula. Here we give an equivalent formulation later found by Creagh and Littlejohn [135, 141]

$$d(E) = \bar{d}(E) + \frac{1}{\pi} \left(\frac{2\pi}{\hbar}\right)^{(N+1)/2} \sum_{\mathbf{M}} \frac{\cos[S_{\mathbf{M}}\hbar - \frac{\pi}{2}\sigma_{\mathbf{M}} + \frac{\pi}{4}(N+1)]}{T_{\mathbf{M}}^{(N-1)/2} |\det \mathcal{K}|^{1/2} |\boldsymbol{\omega}_{\mathbf{M}} \mathcal{K}^{-1} \boldsymbol{\omega}_{\mathbf{M}}|^{1/2}}, \quad (3.24)$$

where the subscript \mathbf{M} indicates that the quantities belong to the orbit with winding numbers \mathbf{M} . The matrix \mathcal{K} is given by

$$\mathcal{K} = \frac{\partial \boldsymbol{\omega}}{\partial \mathbf{I}} = \frac{\partial^2 H}{\partial \mathbf{I} \partial \mathbf{I}}, \quad (3.25)$$

and $\sigma_{\mathbf{M}}$ is a phase

$$\sigma_{\mathbf{M}} = \mathbf{M} \boldsymbol{\alpha}_{\mathbf{M}} + \beta_{\mathbf{M}}, \quad (3.26)$$

where $\beta_{\mathbf{M}}$ is related to the number of positive eigenvalues of the matrix \mathcal{K} , being equal for positive $\boldsymbol{\omega}_{\mathbf{M}} \mathcal{K}^{-1} \boldsymbol{\omega}_{\mathbf{M}}$ or appended by one otherwise.

The semiclassical density of states (3.24) requires the knowledge of the Hamilton function in terms of the action variables \mathbf{I} . This is problematic for non-separable and near-integrable systems where this expression is not always available. We now want to focus on two-dimensional systems $N = 2$. In this case one can construct the implicit function

$$I_2 = g_E(I_1) \quad (3.27)$$

relating the two action variables at a given energy. The Berry-Tabor formula can then be expressed in terms of $g_E(I_1)$ [142]

$$d(E)^{(2)} = \bar{d}(E)^{(2)} + \frac{1}{\pi\hbar} \sum_M \frac{T_M}{\sqrt{\hbar M^3 |g''_E|}} \cos\left(S_M/\hbar - \frac{\pi}{2}\alpha_M - \frac{\pi}{4}\right). \quad (3.28)$$

3.2 Non-integrable systems

For non-integrable systems the previously introduced methods can not be applied, and different approaches need to be used. A suitable framework for the semiclassical treatment of non-integrable systems was first introduced by Gutzwiller [25–27]. Gutzwiller’s trace formula relates the density of states to properties of the periodic orbits in the system. In the following we want to give a short summary of the derivation of Gutzwiller’s trace formula.

For this, we first look at the quantum mechanical propagator which transfers the wave function from a point $x'(t')$ to $x(t)$

$$\psi(x, t) = \int K(x, t, x', t') \psi(x', t') dx'. \quad (3.29)$$

In path integral formulation the quantum mechanical propagator is given by

$$K(x, t, x', t') = \int \mathcal{D}q e^{\frac{i}{\hbar} \int_{t'}^t dt'' \mathcal{L}(q, \dot{q}, t'')}, \quad (3.30)$$

where $\mathcal{D}q$ implies the integration over all paths with starting point $x'(t')$ and endpoint $x(t)$. This also includes classically forbidden orbits, the energy is variable. Using the stationary phase approximation leads to Hamilton’s principle in consequence only allowing for classical paths. The result is the Van-Fleck formula [25, 143]

$$K(x, t, x', 0) = (2\pi i\hbar)^{N/2} \sum_{\text{c.o.}} \sqrt{|c|} e^{\frac{i}{\hbar} R(x, x', t) - i\frac{\pi}{2}\kappa}, \quad (3.31)$$

where we set $t' = 0$, R is Hamilton’s principle function

$$R(x, x', t) = \int_0^t dt'' \mathcal{L}(q, \dot{q}, t''), \quad c = \frac{\partial^2 R}{\partial x \partial x'}, \quad (3.32)$$

and κ the number of caustics on a given path. Fourier transforming from time to energy domain results in the semiclassical Green’s function

$$G(x, x', E) = \frac{1}{i\hbar} \int_0^\infty dt e^{iEt/\hbar} K(x, t, x', 0). \quad (3.33)$$

Inserting (3.31) into the expression for the Green's function (3.33) leads to its semiclassical expression

$$G(x, x', E) = \frac{(2\pi i\hbar)^{N/2}}{i\hbar} \sum_{\text{c.o.}} \int_0^\infty dt \sqrt{|c|} e^{\frac{i}{\hbar} S(x, x', E) - i\frac{\pi}{2}\kappa}, \quad (3.34)$$

where the classical action

$$S(x, x', E) = R(x, x', t) + Et \quad (3.35)$$

appears in the exponent. This fixes the energy for a given classical path. The density of states can then be computed from the semiclassical Green's function via

$$d(E) = \int d^N x G(x, x, E), \quad (3.36)$$

where $x' = x$, meaning that only orbits returning to their starting point contribute. The contribution of the path with length zero results in the Thomas-Fermi term (3.23). The other paths lead to oscillatory contributions. Evaluating the integral in stationary phase approximation allows only for orbits with $p' = p$ meaning that only periodic orbits contribute. The result is finally given by Gutzwiller's trace formula

$$d(E) = \bar{d}(E) + \frac{1}{\pi\hbar} \sum_{\text{ppo}} \frac{T_{\text{ppo}}}{\sqrt{|\det(\mathbf{M}_{\text{ppo}} - \mathbf{1})|}} \cos\left(S_{\text{ppo}}/\hbar - \frac{\pi}{2}\alpha_{\text{ppo}}\right), \quad (3.37)$$

where po stands for periodic orbit and ppo for primitive periodic orbit counting only one repetition of the orbit. \mathbf{M} is the monodromy matrix which summarizes the stability properties of the system for directions orthogonal to the orbit.

4

From solid state systems to excitons in cuprous oxide

Excitons are the fundamental electronic excitations in semiconductors like cuprous oxide. To arrive at a theoretical description of excitons in the cuprous oxide crystal, we first discuss the electronic structure of solid state systems. Cuprous oxide forms a crystalline solid. For such systems the periodic arrangement of the atoms leads to the formation of energy bands. When an electron in a semiconductor is excited from the valence into the conduction band, it leaves behind an unoccupied state in the valence band. Instead of treating the interaction of the electron in the conduction band with all nuclei and the remaining electrons, one treats the missing electron in the valence band as a positively charged quasi particle, the hole. Electron and hole interact through the Coulomb-Interaction and can thus form bound states called excitons. This effective two-particle problem can be seen as the solid state analogue of the hydrogen atom. Starting from a hydrogen-like model, we expand the theoretical description to accurately model the situation in cuprous oxide.

4.1

Electronic structure of solid state systems

In this section we give a brief introduction to the theoretical description of the electronic structure in semiconductor systems. A more detailed introduction to solid state systems can for example be found in Refs. [144–147]. The presentation here is mainly based on Refs. [144, 148].

The description of a solid state system constitutes a complicated many-body problem.

The full Hamiltonian includes all N_e electrons and all N_N nuclei

$$H_0 = \sum_{i=1}^{N_e} \frac{\mathbf{p}_i^2}{2m_0} + \sum_{i=1}^{N_N} \frac{\mathbf{P}_i^2}{2M_i} + \sum_{i=1}^{N_e} \sum_{j=i+1}^{N_e} \frac{e^2}{4\pi\epsilon_0|\mathbf{r}_i - \mathbf{r}_j|} + \sum_{i=1}^{N_N} \sum_{j=i+1}^{N_N} \frac{Q_i Q_j}{4\pi\epsilon_0|\mathbf{R}_i - \mathbf{R}_j|} - \sum_{i=1}^{N_e} \sum_{j=1}^{N_N} \frac{eQ_j}{4\pi\epsilon_0|\mathbf{r}_i - \mathbf{R}_j|}, \quad (4.1)$$

with coordinates and momenta of electrons \mathbf{r}_i , \mathbf{p}_i and nuclei \mathbf{R}_i , \mathbf{P}_i . The first two terms are the kinetic energy of electrons and nuclei with masses M_i , while the following terms describe the Coulomb-interaction between electrons, nuclei with charges Q_i , and the interaction between electrons and nuclei. The full Hamiltonian (4.1) couples the different degrees of freedom. For this reason analytical and numerical solutions for the problem are not feasible and further simplifications are necessary.

4.1.1 Born-Oppenheimer approximation

In a first step one can consider the timescale on which the dynamics of electrons and nuclei take place. In thermal equilibrium electrons and nuclei have the same temperature and thus the same kinetic energy per degree of freedom

$$\left\langle \frac{p^2}{2m_0} \right\rangle = \left\langle \frac{P^2}{2M_i} \right\rangle, \quad (4.2)$$

however, the mass of the nuclei is much larger than that of the electron. Consequently, the electrons have to move much faster than the nuclei. From the perspective of the electron the nuclei almost stand still. This allows for a separate treatment of the different types of particles, which was first introduced by Born and Oppenheimer [149]. When solving the Schrödinger equation for the electrons the kinetic energy of the nuclei is neglected, leading to a Hamiltonian of the form

$$H_e = \sum_{i=1}^{N_e} \frac{\mathbf{p}_i^2}{2m_0} + v(\mathbf{r}_i) + \sum_{i=1}^{N_e} \sum_{j=i+1}^{N_e} \frac{e^2}{4\pi\epsilon_0|\mathbf{r}_i - \mathbf{r}_j|}, \quad (4.3)$$

where the potential $v(\mathbf{r}_i)$ results from the interaction of the electron with the nuclei and nuclei among each other and depends on the positions of the nuclei \mathbf{R}_i implicitly. The energy eigenvalues $E_e(\mathbf{R}_i, \mathbf{R}_j)$ inherit this \mathbf{R}_i dependence. This results in a Hamiltonian for the nuclei of the form

$$H_N = \sum_{i=1}^{N_N} \frac{\mathbf{P}_i^2}{2M_i} + \sum_{i=1}^{N_N} \sum_{j=i+1}^{N_N} E_e(\mathbf{R}_i, \mathbf{R}_j). \quad (4.4)$$

The Hamiltonian (4.4) describes the dynamics of the nuclei. In the following we will assume that the nuclei have settled into an equilibrium position and the dynamical processes causing a displacement out of the equilibrium can be neglected.

4.1.2 Free electron model

We now consider weakly bound valence electrons which mainly determine the electronic properties of the solid. When focusing on a single electron it experiences a potential due to the other electrons and the nuclei. While the core electrons are located at their respective nucleus, screening the Coulomb potential of the nucleus, the valence electrons are only weakly bound and can move almost freely through the solid. In a first approximation the potential produced by the ionic cores is screened by the other valence electrons, leading to a homogenous background thus only a constant potential experienced by the valence electron. Choosing the energy scale accordingly the Hamiltonian inside the solid is given by the kinetic energy of the N valence electrons

$$H_N = \sum_{i=1}^N \frac{\mathbf{p}_i^2}{2m_0} = \sum_{l=1}^N H_l. \quad (4.5)$$

The corresponding Schrödinger equation can then be solved using plane waves

$$\psi_{\mathbf{k}}(\mathbf{r}_i) = A e^{i\mathbf{k}\mathbf{r}_i}, \quad (4.6)$$

with a wave vector k and amplitude A . This ansatz leads to a parabolic dispersion of the electrons

$$E_{\mathbf{k}} = \frac{\hbar^2 \mathbf{k}^2}{2m_0}. \quad (4.7)$$

If we consider a solid with finite extension in the shape of a cuboid with lengths L_1 , L_2 , and L_3 , leading to a potential

$$V(\mathbf{r}_i) = \begin{cases} 0, & \text{if } 0 \leq r_i \leq L_i \\ \infty, & \text{otherwise,} \end{cases} \quad (4.8)$$

the boundary condition at 0 and L_i allow only for wave functions

$$\psi_{\mathbf{n}} = A_{\mathbf{n}} \sin(n_1 \pi r_1 / L_1) \sin(n_2 \pi r_2 / L_2) \sin(n_3 \pi r_3 / L_3), \quad (4.9)$$

with $n_i \in \mathbb{N}$, and thus only discrete energy levels

$$E_{\mathbf{n}} = \frac{\hbar^2 \mathbf{k}_{\mathbf{n}}^2}{2m_0}, \quad (4.10)$$

with $\mathbf{k}_{\mathbf{n}} = (n_1 \pi / L_1, n_2 \pi / L_2, n_3 \pi / L_3)^\top$. In the ground state the electrons occupy only the lowest possible energy levels, where each level can admit two electrons (spin up and down), due to Pauli's exclusion principle. The highest occupied energy is called Fermi energy E_F after Enrico Fermi who first gave an expression for the zero point energy of a fermionic gas [150].

4.1.3 Structure of crystalline solids

In crystalline solids the fundamental constituents exhibit a periodic structure. The solid state system can be described by a crystal lattice and a basis which can consist of single or multiple atoms, molecules, or ions. Placing the basis at the origin the crystal can be constructed by translations

$$\mathbf{T} = \sum_{i=1}^3 n_i \mathbf{a}_i, \quad n_i \in \mathbb{Z}, \quad (4.11)$$

with the primitive translation vectors \mathbf{a}_i . The length of these vectors $|\mathbf{a}_i| = a_i$ are called lattice constants. The object spanned by the primitive translation vectors is the primitive cell with volume

$$V_{\text{pc}} = (\mathbf{a}_1 \times \mathbf{a}_2) \cdot \mathbf{a}_3 = (\mathbf{a}_3 \times \mathbf{a}_1) \cdot \mathbf{a}_2 = (\mathbf{a}_2 \times \mathbf{a}_3) \cdot \mathbf{a}_1. \quad (4.12)$$

Another choice of primitive cell is obtained by drawing the connection between a lattice point and its neighbors and then intersecting the line on the halfway point by an orthogonal plane, the resulting primitive cell is called Wigner-Seitz cell [151]. The full set of points reached by vectors \mathbf{T} is also called Bravais lattice. Depending on the structure of the lattice different symmetry operations can map the lattice onto itself. One distinguishes reflections at a mirror plane σ , the inversion i , rotation by $\phi_n = 2\pi/n$ around an n -fold rotational axis C_n and roto reflections S_n . To obtain a space filling Bravais lattice only $n = 2, 3, 4, 6$ is possible, allowing for 14 distinct Bravais lattices [152, 153]. The translational symmetry of the Bravais lattice should also manifest in the Hamiltonian and the fundamental properties of the solids. A function with the translational symmetry should obey

$$f(\mathbf{r}) = f(\mathbf{r} + \mathbf{T}). \quad (4.13)$$

Since the function is periodic in \mathbf{r} it can be expanded into a multidimensional Fourier series

$$f(\mathbf{r}) = \sum_{\mathbf{G}} f_{\mathbf{G}} e^{i\mathbf{G}\mathbf{r}}, \quad (4.14)$$

with coefficients

$$f_{\mathbf{G}} = \frac{1}{V_{\text{pc}}} \int_{V_{\text{pc}}} f(\mathbf{r}) e^{-i\mathbf{G}\mathbf{r}} dV, \quad (4.15)$$

and the lattice vectors \mathbf{G} of the reciprocal lattice. Due to the translational symmetry (4.13) it follows that

$$f(\mathbf{r} + \mathbf{T}) = \sum_{\mathbf{G}} f_{\mathbf{G}} e^{i\mathbf{G}\mathbf{r} + i\mathbf{G}\mathbf{T}} = \sum_{\mathbf{G}} f_{\mathbf{G}} e^{i\mathbf{G}\mathbf{r}} e^{i\mathbf{G}\mathbf{T}} \stackrel{!}{=} f(\mathbf{r}), \quad (4.16)$$

and thus $\mathbf{G}\mathbf{T} = 2\pi N$ with $N \in \mathbb{Z}$. This can be achieved by setting

$$\mathbf{G} = \sum_{i=1}^3 m_i \mathbf{b}_i, \quad m_i \in \mathbb{Z}, \quad (4.17)$$

with the basis vectors of the reciprocal lattice

$$\begin{aligned}\mathbf{b}_1 &= \frac{2\pi}{V_{\text{pc}}}(\mathbf{a}_2 \times \mathbf{a}_3), \\ \mathbf{b}_2 &= \frac{2\pi}{V_{\text{pc}}}(\mathbf{a}_3 \times \mathbf{a}_1), \\ \mathbf{b}_3 &= \frac{2\pi}{V_{\text{pc}}}(\mathbf{a}_1 \times \mathbf{a}_2),\end{aligned}\tag{4.18}$$

which satisfy

$$\mathbf{b}_i \cdot \mathbf{a}_j = 2\pi\delta_{ij}.\tag{4.19}$$

The \mathbf{b}_i have the dimension $[\text{m}^{-1}]$ and thus the same as a wave vector or the momentum after multiplication with \hbar . In analogy to the primitive translational vectors the basis vectors of the reciprocal lattice can also be used to construct a Wigner-Seitz cell. In the reciprocal lattice this cell is called the Brillouin zone [154]. The center of the Brillouin zone at $\mathbf{k} = 0$ is called Γ -point.

4.1.4 Bloch functions

We now want to exploit the periodic structure of the crystal which is inherited to the potential $V_{\text{eff}}(\mathbf{r}) = V_{\text{eff}}(\mathbf{r} + \mathbf{T})$. It can be expressed as a Fourier series

$$V_{\text{eff}}(\mathbf{r}) = \sum_{\mathbf{G}} V_{\mathbf{G}} e^{i\mathbf{G}\mathbf{r}}.\tag{4.20}$$

Using the ansatz

$$\psi(\mathbf{r}) = \sum_{\mathbf{k}} c_{\mathbf{k}} e^{i\mathbf{k}\mathbf{r}},\tag{4.21}$$

the Schrödinger equation reads

$$\sum_{\mathbf{k}} e^{i\mathbf{k}\mathbf{r}} \left[\left(\frac{\hbar^2 \mathbf{k}^2}{2m_0} - E \right) c_{\mathbf{k}} + \sum_{\mathbf{G}} V_{\mathbf{G}} c_{\mathbf{k}-\mathbf{G}} \right] = 0,\tag{4.22}$$

which for arbitrary \mathbf{k} values can only be satisfied if

$$\left(\frac{\hbar^2 \mathbf{k}^2}{2m_0} - E \right) c_{\mathbf{k}} + \sum_{\mathbf{G}} V_{\mathbf{G}} c_{\mathbf{k}-\mathbf{G}} = 0.\tag{4.23}$$

As can be seen from equation (4.23) only the \mathbf{k} which differ by lattice vectors of the reciprocal lattice \mathbf{G} couple. For a given \mathbf{k} value the wave function reads

$$\psi_{\mathbf{k}}(\mathbf{r}) = \sum_{\mathbf{G}} c_{\mathbf{k}-\mathbf{G}} e^{i(\mathbf{k}-\mathbf{G})\mathbf{r}} = \left(\sum_{\mathbf{G}} c_{\mathbf{k}-\mathbf{G}} e^{-i\mathbf{G}\mathbf{r}} \right) e^{i\mathbf{k}\mathbf{r}}.\tag{4.24}$$

The factor before the plane waves constitutes a Fourier series and thus a lattice periodic function

$$u_{\mathbf{k}}(\mathbf{r}) = \left(\sum_{\mathbf{G}} c_{\mathbf{k}-\mathbf{G}} e^{-i\mathbf{G}\mathbf{r}} \right) = u_{\mathbf{k}}(\mathbf{r} + \mathbf{T}). \quad (4.25)$$

The wave functions $\psi_{\mathbf{k}}(\mathbf{r})$ consisting of the product of such a lattice periodic function and a plane wave are called Bloch functions [155]. It becomes evident that adding a reciprocal lattice vector \mathbf{G} to \mathbf{k} does not change the Bloch function

$$\psi_{\mathbf{k}+\mathbf{G}}(\mathbf{r}) = \left(\sum_{\mathbf{G}'} c_{\mathbf{k}+\mathbf{G}-\mathbf{G}'} e^{-i\mathbf{G}'\mathbf{r}} \right) e^{i(\mathbf{k}+\mathbf{G})\mathbf{r}} = \left(\sum_{\mathbf{G}'} c_{\mathbf{k}-(\mathbf{G}'-\mathbf{G})} e^{-i(\mathbf{G}'-\mathbf{G})\mathbf{r}} \right) e^{i\mathbf{k}\mathbf{r}} = \psi_{\mathbf{k}}(\mathbf{r}). \quad (4.26)$$

Consequently, also the physical meaning remains unchanged when adding a reciprocal lattice vector \mathbf{G} . It is therefore sufficient to limit oneself to the first Brillouin zone.

4.1.5 Nearly free electrons

We now revisit the case of free electrons considering the symmetry of the crystal. As wave function we use a Bloch function, while considering the coefficients $V_{\mathbf{G}}$ as negligibly small. The Hamiltonian reduces to the case of the free electron model (4.5). Inserting the wave function (4.24) into the Schrödinger equation leads to energy eigenvalues

$$E_{\mathbf{k},\mathbf{G}} = \sum_{\mathbf{G}} \frac{\hbar^2 |\mathbf{k} + \mathbf{G}|^2}{2m_0}, \quad (4.27)$$

where the different parabolas intersect at the edge of the Brillouin zone and at its center. The first Brillouin zone for this situation is sketched in figure 4.1 for a one-dimensional lattice. When considering small coefficients $V_{\mathbf{G}}$ and investigating the intersection point of two parabolas with different reciprocal lattice vectors \mathbf{G}' and \mathbf{G}'' only the coefficients $c_{\mathbf{k}-\mathbf{G}'}$ and $c_{\mathbf{k}-\mathbf{G}''}$ are relevant for the wave function. This can be seen from equation (4.23) since

$$E \approx \frac{\hbar^2 |\mathbf{k} - \mathbf{G}'|^2}{2m_0} = \frac{\hbar^2 |\mathbf{k} - \mathbf{G}''|^2}{2m_0}, \quad (4.28)$$

which at negligibly small coefficients $V_{\mathbf{G}}$ only allows nonzero $c_{\mathbf{k}-\mathbf{G}'}$ and $c_{\mathbf{k}-\mathbf{G}''}$. When only considering this contribution, equation (4.23) reduces to the system of equations

$$\begin{aligned} \left(\frac{\hbar^2 |\mathbf{k} - \mathbf{G}'|^2}{2m_0} + V_0 - E \right) c_{\mathbf{k}-\mathbf{G}'} + V_{\mathbf{G}'-\mathbf{G}''} c_{\mathbf{k}-\mathbf{G}''} &= 0, \\ \left(\frac{\hbar^2 |\mathbf{k} - \mathbf{G}''|^2}{2m_0} + V_0 - E \right) c_{\mathbf{k}-\mathbf{G}''} + V_{\mathbf{G}''-\mathbf{G}'} c_{\mathbf{k}-\mathbf{G}'} &= 0. \end{aligned} \quad (4.29)$$

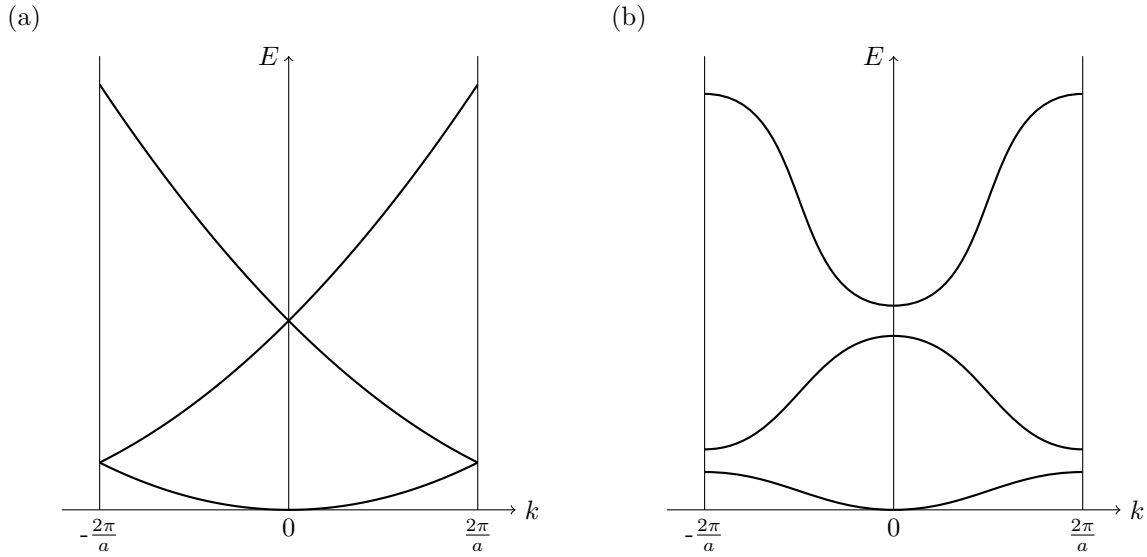


Figure 4.1.: First Brillouin zone for nearly free electrons (a) with vanishing potential and (b) small perturbing potential. The perturbing potential leads to a splitting of the degenerate energy eigenvalues at the center and at the edges of the Brillouin zone.

In the following we set $V_0 = 0$ which only constitutes a shift of the energy axis. This leads to energy eigenvalues

$$E_{\pm} = \frac{E_{\mathbf{k}-\mathbf{G}'} + E_{\mathbf{k}-\mathbf{G}''}}{2} \pm \frac{\sqrt{(E_{\mathbf{k}-\mathbf{G}'} - E_{\mathbf{k}-\mathbf{G}''})^2 + 4V_{\mathbf{G}''-\mathbf{G}'}V_{\mathbf{G}'-\mathbf{G}''}}}{2}. \quad (4.30)$$

At the intersection point $E_{\mathbf{k}-\mathbf{G}'} = E_{\mathbf{k}-\mathbf{G}''} = \tilde{E}$ and thus

$$E_{\pm} = \tilde{E} \pm \sqrt{V_{\mathbf{G}''-\mathbf{G}'}V_{\mathbf{G}'-\mathbf{G}''}}, \quad (4.31)$$

resulting in a splitting of the energies by $2\sqrt{V_{\mathbf{G}''-\mathbf{G}'}V_{\mathbf{G}'-\mathbf{G}''}}$. Expanding the dispersion (4.30) at the intersection point $(\mathbf{G}' + \mathbf{G}'')/2$ results in a parabolic behavior of the energy near the intersection point. The dispersion of electron at the Γ point and the edges of the Brillouin zone thus can be approximated by parabolas. The situation is shown in figure 4.1 for a one-dimensional lattice. The avoided crossing at the center and edges of the Brillouin zone lead to energy regions which can not be accessed by electrons. The allowed regions are called energy bands, whereas the forbidden regions are called energy gaps. One distinguishes valence bands, which in the ground state of the crystal are occupied by electrons and conduction bands which are not occupied. Materials can then be classified by the position of the Fermi energy and the gap energy between the uppermost valence and lowest conduction band. Materials where the Fermi level is located within a valence band which hence is not fully occupied are called conductor or

metal. If the Fermi level is located in the band gap, resulting in a fully occupied valence band and an empty conduction band, the size of the gap energy is the decisive factor. Materials with a small energy gap, where an electron can easily be excited from the valence to the conduction band are called semiconductor, whereas material with a large band gap are called insulator.

4.1.6 Effective mass and electron holes

When considering the expansion of equation (4.30) at the intersection point one notices that the pre-factor of \mathbf{k}^2 is no longer given by

$$c_{\mathbf{k}^2} = \frac{\hbar^2}{2m_0}. \quad (4.32)$$

To achieve a similar description one can introduce the effective mass m^*

$$\frac{1}{m^*} = \frac{1}{\hbar^2} \frac{d^2 E(\mathbf{k})}{d\mathbf{k}^2}. \quad (4.33)$$

Note that for a parabolic maximum the effective mass is now negative. In general the effective mass is given by a tensor. When an electron is excited from the valence band into the conduction band it leaves behind an unoccupied place in the valence band. Instead of treating the interaction of the conduction electron with all the remaining valence electrons and nuclei it is convenient to treat the unoccupied place in the valence band as a positively charged quasi particle called the hole. As the total charge, mass, momentum and energy need to be conserved in the system the material parameters of the hole are the same as the ones of the missing electron apart from a minus sign. The properties of the hole in comparison to the missing electron in the valence band are shown in table 4.1.

4.2 | Excitons in cuprous oxide

In this section we discuss the weakly bound Wannier excitons with large extensions which show hydrogen-like behavior in a first approximation [40]. After a discussion of

Table 4.1.: Comparison of the material parameters of hole and the corresponding missing electron in the valence band (vb).

particle	charge	mass	momentum	energy
electron	$-e$	$m_{e,vb}$	$\mathbf{p}_{e,vb}$	$E_{e,vb}$
hole	e	$m_h = -m_{e,vb}$	$\mathbf{p}_h = -\mathbf{p}_{e,vb}$	$E_h = -E_{e,vb}$

the hydrogen-like model we expand our description to include the complex valence band structure of cuprous oxide. For a more detailed treatment of Wannier excitons as well as an introduction to the tightly bound Frenkel excitons [36–38] see for example [41].

4.2.1 Hydrogen-like model for excitons

In a simple model we can consider the valence and conduction band having a parabolic dispersion with their extrema located at the Γ -point where $\mathbf{k} = 0$. The Hamiltonian for the electron in the conduction band is then given by

$$H_e(\mathbf{p}_e) = \frac{\mathbf{p}_e^2}{2m_e} + E_g, \quad (4.34)$$

with the momentum of the electron \mathbf{p}_e and its effective mass m_e which in general differs from the free electron mass m_0 . The term E_g denotes the gap energy by which the conduction band is shifted upwards compared to the valence band. For parabolic bands the Hamiltonian for the hole then takes a similar form

$$H_h(\mathbf{p}_h) = \frac{\mathbf{p}_h^2}{2m_h}, \quad (4.35)$$

where \mathbf{p}_h is the momentum of the hole and its effective mass is given by m_h . Electron and hole are then bound by the Coulomb interaction

$$V_C = -\frac{e^2}{4\pi\epsilon_0\epsilon} \frac{1}{|\mathbf{r}_e - \mathbf{r}_h|}, \quad (4.36)$$

which due to the crystal environment is screened by the permittivity ϵ . $\mathbf{r}_{e,h}$ are the coordinates of electron and hole, respectively. The full Hamiltonian of the hydrogen-like model then reads

$$H = E_g + \frac{\mathbf{p}_e^2}{2m_e} + \frac{\mathbf{p}_h^2}{2m_h} - \frac{e^2}{4\pi\epsilon_0\epsilon|\mathbf{r}_e - \mathbf{r}_h|}. \quad (4.37)$$

Since this problem only depends on the coordinate differences $\mathbf{r}_e - \mathbf{r}_h$ it can be simplified by introducing relative and center-of-mass coordinates

$$\begin{aligned} \mathbf{r} &= \mathbf{r}_e - \mathbf{r}_h, \\ \mathbf{R} &= \frac{m_e\mathbf{r}_e + m_h\mathbf{r}_h}{M}, \\ \mathbf{p} &= \frac{m_h\mathbf{p}_e - m_e\mathbf{p}_h}{M}, \\ \mathbf{P} &= \mathbf{p}_e + \mathbf{p}_h, \end{aligned} \quad (4.38)$$

with $M = m_e + m_h$. Inserting this transformation into (4.37), the relative and center-of-mass motion decouple

$$H = E_g + \frac{\mathbf{p}^2}{2\mu} - \frac{e^2}{4\pi\epsilon_0\epsilon|\mathbf{r}|} + \frac{\mathbf{P}^2}{2M}, \quad (4.39)$$

yielding a Coulomb problem for the relative coordinates with reduced mass $\mu = m_e m_h / M$ and the problem of a free particle for the center-of-mass motion. Since the total momentum is conserved, the center-of-mass motion gets its momentum \mathbf{P} from the exciting photon. However, the corresponding values are low, therefore we will in the following neglect the center-of-mass motion. The quantum-mechanical solution for the Coulomb problem is given by the Rydberg series

$$E_n = E_g - \frac{E_{\text{Ryd}}}{n^2}, \quad (4.40)$$

with principle quantum number n where the Rydberg energy of the exciton E_{Ryd} is now scaled by the material parameters compared to the hydrogen-like case $E_{\text{Ryd,H}}$

$$E_{\text{Ryd}} = \frac{\mu}{m_0 \varepsilon^2} E_{\text{Ryd,H}} = \frac{\mu e^4}{8 \varepsilon_0^2 \varepsilon^2 \hbar^2}, \quad (4.41)$$

in addition the energy is shifted by the band gap E_g . The expected radius of an exciton in a state with principle quantum number n and angular momentum quantum number l is then given by

$$\langle r \rangle_{n,l} = \frac{a_{\text{exc}}}{2} [3n^2 - l(l+1)], \quad (4.42)$$

with the Bohr radius of the exciton a_{exc} , which also needs to be screened compared to the hydrogen-like version a_{H} , i.e.,

$$a_{\text{exc}} = \frac{m_0 \varepsilon}{\mu} a_{\text{H}} = \frac{4\pi \varepsilon_0 \varepsilon \hbar^2}{e^2 \mu}. \quad (4.43)$$

4.2.2 Cuprous oxide

Cuprous oxide with the formula Cu_2O forms a red colored solid where the oxygen atoms form a body centered cubic sublattice which is shifted by 1/4 of the space diagonal compared to the copper atoms forming a face centered cubic sublattice [156, 157]. The resulting lattice structure is sketched in figure 4.2. The lattice constant for cuprous oxide is given by $a \approx 4.2696 \text{ \AA}$ [158]. The point group of cuprous oxide is given by O_{h} [43, 158]. In a first approximation the excitons can be described within a hydrogen-like model.

Cuprous oxide is a direct semiconductor with band gap $E_g = 2.17208 \text{ eV}$ [43]. As such electrons can be excited from the valence to the conduction band using light in the yellow part of the visible spectrum. This allows for a comparably easy experimental treatment. Electrons can form bound exciton states with the remaining hole in the valence band leading to a yellow exciton series. The yellow series can in a good approximation be understood as a Rydberg series, where the material parameters now differ from the hydrogen atom case. The effective mass of the electron in the conduction band is given by $m_e = 0.99 m_0$ and the effective mass of the hole in the valence band by $m_h = 0.58 m_0$ [159]. The permittivity of cuprous oxide is given by $\varepsilon = 7.5$ [160]. A

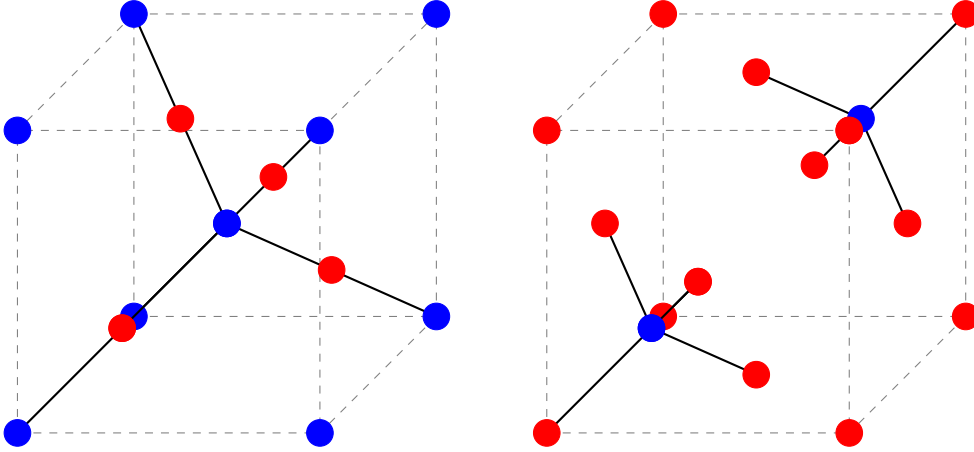


Figure 4.2.: Two possible choices for the unit cell of cuprous oxide. On the left the bcc sublattice of the oxygen atoms (blue) is chosen as a basis while on the right we choose the fcc sublattice of the copper atoms (red). Chemical bonds are indicated by black lines. Taken from Ref. [114].

summary of the material parameters used in this thesis can be found in appendix A. Using equation (4.41) the Rydberg energy is given by $E_{\text{Ryd}} = 86 \text{ meV}$ which is high compared to other semiconductors. This allows for the observation of yellow excitons up to high principle quantum numbers at $n = 25$ in 2014 [43] and more recently up to $n = 30$ [44]. These highly excited states were found in natural crystals. It is also possible to artificially grow crystals [161–163]. However, up to now the synthetic samples are only capable of accessing states up to $n \approx 10$ [88, 164].

For subsequent calculations we introduce exciton-Hartree units obtained by setting $\hbar = e = m_0/\gamma'_1 = 1/(4\pi\epsilon_0\epsilon) = 1$ in analogy to atomic-Hartree units [165, 166]. A summary of this unit system can be found in appendix B. The excitonic Bohr radius for cuprous oxide can be calculated by equation (4.43), giving $a_{\text{exc}} = 1.1 \text{ nm}$. Using equation (4.42) we can see that the highly excited Rydberg states at $n = 30$ take up huge extensions in the μm range. For atomic systems these ranges are only reached at $n \approx 135$. Such exaggerated properties can also be found for external fields. Comparing the atomic-Hartree units to the exciton-Hartree units (see appendix B) for electric field strength F and magnetic flux density B

$$\frac{B_{\text{H}}}{B_{\text{exc}}} \approx 432, \quad \frac{F_{\text{H}}}{F_{\text{exc}}} = 3236, \quad (4.44)$$

it can be seen that the region of high field strength is reached much faster compared to atomic systems. This makes cuprous oxide a promising candidate for the observation of phenomena, for which the field strengths needed in atomic systems are experimentally not accessible [104, 167].

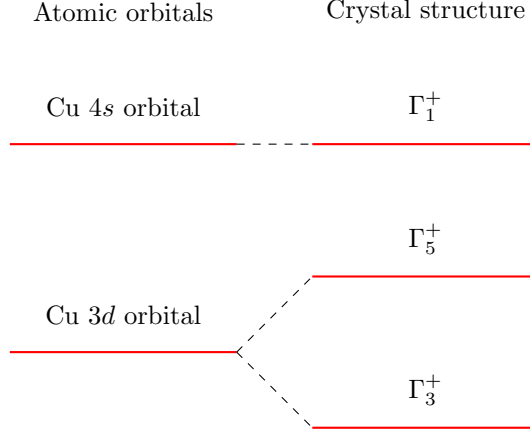


Figure 4.3.: Splitting of the atomic orbitals due to the crystal symmetry.

A more detailed investigation of the exciton spectra reveals deviations from the purely hydrogen-like behavior [45, 48]. These deviations can be understood when considering the complicated band structure of cuprous oxide [46]. There the valence band stems from copper 3d electrons and the conduction band stems from copper 4s electrons [168]. Considering the cubic O_h symmetry of the crystal, the irreducible representation of angular momentum $l = 2$ reduces to $\Gamma_3 + \Gamma_5$ and the one for $l = 0$ to Γ_1 [169]. The splitting of the orbitals is sketched in figure 4.3. The Γ_1 conduction band transforms like unity [169]. It is thus sufficient to model the conduction band by using a parabolic band

$$H_e(\mathbf{p}_e) = E_g + \frac{1}{2m_e} \mathbf{p}_e^2, \quad (4.45)$$

with effective mass m_e . A convenient way of modeling the three-fold degenerate Γ_5 band was introduced by Luttinger and Kohn [49, 50]. In this model the degree of freedom describing the valence band can be expressed by three 3×3 matrices \mathbf{I}_i satisfying $[\mathbf{I}_i, \mathbf{I}_j] = i\hbar \varepsilon_{ijk} \mathbf{I}_k$ and $\mathbf{I}^2 = 2$, which behave just like an angular momentum $L = 1$. We choose our basis such that the \mathbf{I}_i coincide with the matrices belonging to an angular momentum $L = 1$ where we chose the quantization axis to be aligned with the z axis

$$\mathbf{I}_x = \frac{\hbar}{\sqrt{2}} \begin{pmatrix} 0 & 1 & 0 \\ 1 & 0 & 1 \\ 0 & 1 & 0 \end{pmatrix}, \quad \mathbf{I}_y = \frac{\hbar}{\sqrt{2}} \begin{pmatrix} 0 & -i & 0 \\ i & 0 & -i \\ 0 & i & 0 \end{pmatrix}, \quad \mathbf{I}_z = \hbar \begin{pmatrix} 1 & 0 & 0 \\ 0 & 0 & 0 \\ 0 & 0 & -1 \end{pmatrix}. \quad (4.46)$$

Note that the Bloch functions of Γ_5^+ transform like xy , yz , and xz and not like x, y , and z , the basis function for angular momentum $L = 1$ which would belong to Γ_4^- . This

must be taken into account when assigning the symmetry of states. To distinguish I from an angular momentum it is called quasispin. Considering the spin of the hole S_h in the valence band and the cubic symmetry of the system this leads to an effective 6×6 Hamiltonian for the hole in the valence band [48–51]

$$\begin{aligned}
 H_h(\mathbf{p}_h, \hat{\mathbf{I}}, \hat{\mathbf{S}}_h) &= \frac{\gamma_1}{2m_0} \mathbf{p}_h^2 + \frac{1}{2\hbar^2 m_0} [4\gamma_2 \hbar^2 \mathbf{p}_h^2 \\
 &- 6\gamma_2 (p_{h1}^2 \mathbf{I}_1^2 + \text{c.p.}) - 12\gamma_3 (\{p_{h1}, p_{h2}\} \{\mathbf{I}_1, \mathbf{I}_2\} + \text{c.p.}) \\
 &- 12\eta_2 (p_{h1}^2 \mathbf{I}_1 \mathbf{S}_{h1} + \text{c.p.}) + 2(\eta_1 + 2\eta_2) \mathbf{p}_h^2 (\mathbf{I} \cdot \mathbf{S}_h) \\
 &- 12\eta_3 (\{p_{h1}, p_{h2}\} (\mathbf{I}_1 \mathbf{S}_{h2} + \mathbf{I}_2 \mathbf{S}_{h1}) + \text{c.p.})] + H_{\text{SO}}, \tag{4.47}
 \end{aligned}$$

with the symmetrized product $\{a, b\} = (ab+ba)/2$ and c.p. denoting cyclic permutations. The Luttinger parameters γ_i and η_i are material dependent parameters which can be obtained by fitting the Hamiltonian to full band structure calculations [47, 48]. The first parameter is connected to the effective mass of the hole in the valence band

$$m_h = m_0/\gamma_1, \tag{4.48}$$

the other parameters characterize the deviations of the purely parabolic behavior. The band structure contributions can then be summarized in the Hamiltonian

$$\begin{aligned}
 H_{\text{band}}(\mathbf{p}_h, \mathbf{I}, \mathbf{S}_h) &= \frac{1}{2\hbar^2 m_0} [4\gamma_2 \hbar^2 \mathbf{p}_h^2 \\
 &- 6\gamma_2 (p_{h1}^2 \mathbf{I}_1^2 + \text{c.p.}) - 12\gamma_3 (\{p_{h1}, p_{h2}\} \{\mathbf{I}_1, \mathbf{I}_2\} + \text{c.p.}) \\
 &- 12\eta_2 (p_{h1}^2 \mathbf{I}_1 \mathbf{S}_{h1} + \text{c.p.}) + 2(\eta_1 + 2\eta_2) \mathbf{p}_h^2 (\mathbf{I} \cdot \mathbf{S}_h) \\
 &- 12\eta_3 (\{p_{h1}, p_{h2}\} (\mathbf{I}_1 \mathbf{S}_{h2} + \mathbf{I}_2 \mathbf{S}_{h1}) + \text{c.p.})] + H_{\text{SO}}. \tag{4.49}
 \end{aligned}$$

A list of the material parameters used in this thesis can be found in appendix A. At the Γ point where $\mathbf{p}_h = 0$ the only remaining term in the hole Hamiltonian (4.47) is given by the spin-orbit term

$$H_{\text{SO}} = \frac{2}{3} \Delta \left(1 + \frac{1}{\hbar^2} \mathbf{I} \cdot \mathbf{S}_h \right), \tag{4.50}$$

which couples quasispin \mathbf{I} and hole spin \mathbf{S}_h to form an effective hole spin

$$\mathbf{J} = \mathbf{I} + \mathbf{S}_h, \tag{4.51}$$

which takes the values $J = 1/2$ and $J = 3/2$. The coupling scheme is sketched in figure 4.4. Since a spin $S = 1/2$ belongs to irreducible representation Γ_6 [169], the irreducible representation of the bands is obtained from the direct product with the irreducible representation of the Bloch functions. The uppermost valence band then

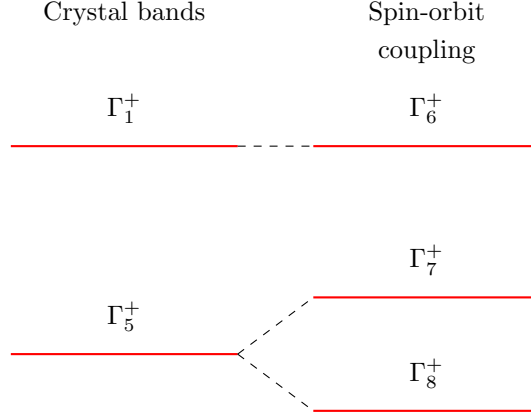


Figure 4.4.: Influence of the spin-orbit coupling for the electron in the conduction and the hole in the valence band. The Γ_7^+ band corresponds to $J = 1/2$ and the Γ_8^+ band to $J = 3/2$.

splits as $\Gamma_5 \otimes \Gamma_6 = \Gamma_7 \oplus \Gamma_8$ [169]. Evaluating the spin orbit term for the basis states $|J, m_J\rangle$ with magnetic quantum numbers m_J one finds the eigenvalues

$$\begin{aligned} H_{\text{SO}} \left| \frac{1}{2}, m_J \right\rangle &= 0 \left| \frac{1}{2}, m_J \right\rangle, \\ H_{\text{SO}} \left| \frac{3}{2}, m_J \right\rangle &= \Delta \left| \frac{3}{2}, m_J \right\rangle, \end{aligned} \quad (4.52)$$

where the energy of the fourfold-degenerate states with $J = 3/2$ are shifted by the spin-orbit coupling Δ and the twofold-degenerate states with $J = 1/2$ remain unchanged. Moving away from the Γ point the fourfold-degenerate band splits into two twofold-degenerate bands giving a description with light and heavy holes. The twofold degeneracy of the three distinct band remains due to Kramers' theorem for half integer spin [170]. For cuprous oxide the spin-orbit coupling takes a value of $\Delta = 131$ meV [48]. Considering transitions from the lower-lying valence bands one needs an energy $E_g + \Delta$ and thus light from the green part of the visible spectrum, to excite an electron to the conduction band, leading to a green exciton series. A schematic of the band structure is shown in figure 4.5. The full exciton Hamiltonian can then be constructed by adding the contributions of the electron in the conduction band and the hole in the valence band and their coupling via the Coulomb interaction

$$H = H_e(\mathbf{p}_e) + H_h(\mathbf{p}_h, \hat{\mathbf{I}}, \hat{\mathbf{S}}_h) - \frac{e^2}{4\pi\epsilon_0\epsilon|\mathbf{r}_e - \mathbf{r}_h|}. \quad (4.53)$$

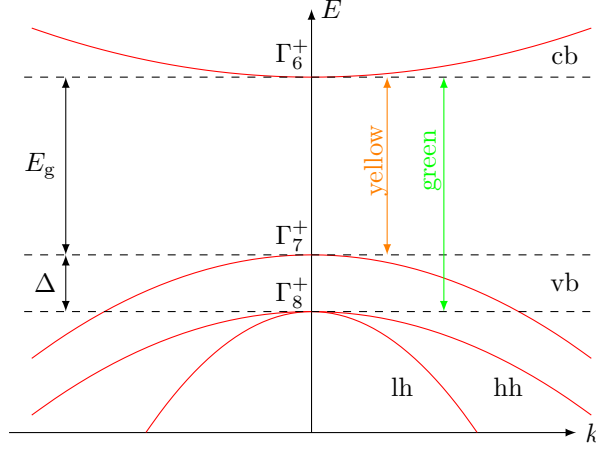


Figure 4.5.: Schematic view of the band structure of Cu_2O . The valence band consists of a band with light holes (lh) and heavy holes (hh) as well as a split off band separated by the spin-orbit splitting Δ . The light needed to excite an electron from the valence band (vb) to the conduction band (cb) belongs to the green and the yellow part of the spectrum, resulting in two green and a yellow exciton series. We already presented similar pictures in Refs. [118, 119].

Transforming to relative and center-of-mass coordinates and neglecting the center-of-mass motion results in the Hamiltonian

$$H = E_g + H_{\text{kin}}(\mathbf{p}, \mathbf{I}, \mathbf{S}_h) - \frac{e^2}{4\pi\epsilon_0\epsilon|\mathbf{r}|} + H_{\text{SO}}, \quad (4.54)$$

where H_{kin} includes all the terms dependent on the relative momenta

$$\begin{aligned} H_{\text{kin}}(\mathbf{p}, \mathbf{I}, \mathbf{S}_h) = & \frac{\gamma'_1}{2m_0}\mathbf{p}^2 + \frac{1}{2\hbar^2m_0} [4\gamma_2\hbar^2\mathbf{p}^2 \\ & - 6\gamma_2(p_1^2\mathbf{I}_1^2 + \text{c.p.}) - 12\gamma_3(\{p_1, p_2\}\{\mathbf{I}_1, \mathbf{I}_2\} + \text{c.p.}) \\ & - 12\eta_2(p_1^2\mathbf{I}_1\mathbf{S}_{h1} + \text{c.p.}) + 2(\eta_1 + 2\eta_2)\mathbf{p}^2(\mathbf{I} \cdot \mathbf{S}_h) \\ & - 12\eta_3(\{p_1, p_2\}(\mathbf{I}_1\mathbf{S}_{h2} + \mathbf{I}_2\mathbf{S}_{h1}) + \text{c.p.})], \end{aligned} \quad (4.55)$$

whit

$$\gamma'_1 = \gamma_1 + m_0/m_e. \quad (4.56)$$

To better distinguish spherically symmetric contributions and contributions with cubic symmetry it is convenient to express the Hamiltonian (4.54) in terms of irreducible

tensors [46, 171–175]

$$\begin{aligned}
 H = & E_g - \frac{e^2}{4\pi\epsilon_0\epsilon} \frac{1}{r} + \frac{2}{3}\Delta \left(1 + \frac{1}{\hbar^2} I^{(1)} \cdot S_h^{(1)} \right) \\
 & + \frac{\gamma'_1}{2\hbar^2 m_0} \left[\hbar^2 p^2 - \frac{\mu'}{3} P^{(2)} \cdot I^{(2)} \right. \\
 & \quad \left. + \frac{\delta'}{3} \left(\sum_{k=\pm 4} [P^{(2)} \times I^{(2)}]_k^{(4)} + \frac{\sqrt{70}}{5} [P^{(2)} \times I^{(2)}]_0^{(4)} \right) \right] \\
 & + \frac{3\eta_1}{\hbar^2 m_0} \left[\frac{1}{3} p^2 \left(I^{(1)} \cdot S_h^{(1)} \right) - \frac{\nu}{3} P^{(2)} \cdot D^{(2)} \right. \\
 & \quad \left. + \frac{\tau}{3} \left(\sum_{k=\pm 4} [P^{(2)} \times D^{(2)}]_k^{(4)} + \frac{\sqrt{70}}{5} [P^{(2)} \times D^{(2)}]_0^{(4)} \right) \right]. \quad (4.57)
 \end{aligned}$$

Here we use the same convention for the tensor operators as in Refs. [46, 175]. The coefficients

$$\mu' = \frac{6\gamma_3 + 4\gamma_2}{5\gamma'_1}, \quad \nu = \frac{6\eta_3 + 4\eta_2}{5\eta_1} \quad (4.58)$$

characterize the spherically symmetric contributions and

$$\delta' = \frac{\gamma_3 - \gamma_2}{\gamma'_1}, \quad \tau = \frac{\eta_3 - \eta_2}{\eta_1} \quad (4.59)$$

the terms with cubic symmetry. Since this thesis aims to establish a semiclassical description for excitons in cuprous oxide we neglect the central-cell corrections [60, 89, 91] which only affect the lowest exciton states. The Hamiltonian (4.54) provides the basis for understanding quantum mechanical exciton spectra. These can for example be obtained by diagonalizing the Hamiltonian in a complete basis [46], perturbative approaches on basis of the hydrogen-like model [66], or solving integro-differential equation in momentum space [48]. However, an interpretation of exciton spectra in terms of classical dynamics is still missing.

5

Adiabatic approach for the exciton dynamics in cuprous oxide

The aim of this thesis is to provide a classical interpretation of exciton spectra. In a hydrogen-like model the connection of classical Kepler ellipses and the Rydberg series is well established. Here, one follows the correspondence principle going from quantum mechanical operators to classical observables leading to a classical Hamilton function, providing classical orbits after integrating Hamilton's equations of motion.

For excitons in cuprous oxide the situation is more complicated. The full Hamiltonian (4.54) includes additional spin degrees of freedom and thus quantities with no direct classical counterpart. To deal with these additional degrees of freedom we introduce an adiabatic approach [114].

Essential parts of this chapter have been published [115] and submitted for publication [119].

5.1 Adiabatic approach

In the previous chapter 4 we introduced the Hamiltonian for excitons in cuprous oxide. We have seen that, in a first approximation, their spectra can be understood in terms of a hydrogen-like Rydberg series. A full theoretical description, however, needs to include additional spin degrees of freedom to accurately capture the valence band structure. The lowest order of these band structure corrections is given by the spin-orbit term (4.50). If we neglect the correction terms of higher order in the momenta the Hamiltonian separates into the hydrogen-like system defining the dynamics in the relative configuration and a Hamiltonian for the spin degrees of freedom. We can now investigate the timescales on which the dynamics of the two subsystems takes place. These should be given by $T \sim \hbar/\Delta E$ with the energy spacing ΔE between adjacent levels. For the Rydberg series

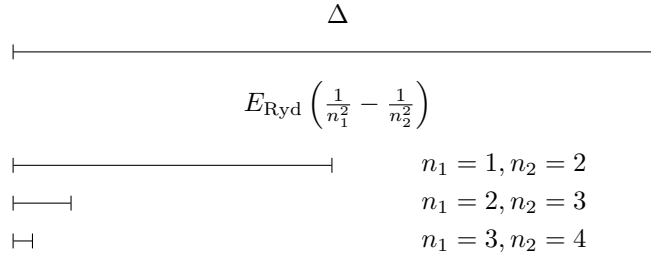


Figure 5.1.: Comparison of the spin orbit splitting Δ and the first three spacings between adjacent Rydberg levels. We already presented this figure in Ref. [119].

the energy spacings are given by

$$\Delta E = E_{\text{Ryd}} \left(\frac{1}{n_1^2} - \frac{1}{n_2^2} \right). \quad (5.1)$$

With increasing principle quantum number n the energy spacing becomes smaller and smaller, for large values going as $\Delta E \sim 1/n^3$, leading to an increase of the characteristic timescale on which the dynamics in the relative coordinate takes place. For the spin degrees of freedom on the other hand, the spacing between adjacent levels always stays constant at the value of the spin-orbit splitting

$$\Delta E = \Delta. \quad (5.2)$$

The situation is visualized in figure 5.1 for the lowest Rydberg states in comparison to the spin-orbit splitting Δ . It becomes apparent that the energy splitting for the Rydberg series decreases rapidly, being an order of magnitude lower compared to the spin-orbit splitting already for $n = 2$. As a result, the corresponding timescale for the dynamics in coordinate space becomes much slower compared to the dynamics of the spin degrees of freedom.

This is the basis for the adiabatic approach. When considering the full Hamiltonian (4.54), the relative motion couples to the spin motion. However, the spin motion is much faster. In analogy to the Born-Oppenheimer approximation (4.3) where the fast electrons react instantaneously to a new configuration of the nuclei, we assume that the spin degrees of freedom react instantaneously to a new configuration in coordinate space.

To achieve this we first neglect the hydrogen-like part of the Hamiltonian, leading to a Schrödinger equation for the spin degrees of freedom

$$H_{\text{band}}(\mathbf{p}_h, \mathbf{I}, \mathbf{S}_h) \chi_n(\mathbf{p}; \mathbf{I}, \mathbf{S}_h) = W_n(\mathbf{p}) \chi_n(\mathbf{p}; \mathbf{I}, \mathbf{S}_h), \quad (5.3)$$

which depends on the momenta as a parameter. The $W_n(\mathbf{p})$ form energy surfaces in momentum space. They are the energy eigenvalues of the Hamiltonian H_{band} with cor-

responding eigenfunctions

$$\chi_n(\mathbf{p}; \mathbf{I}, \mathbf{S}_h) = \sum_{m_I, m_{S_h}} c_{m_I, m_{S_h}}(\mathbf{p}) |m_I, m_{S_h}\rangle. \quad (5.4)$$

This leads to three distinct energy surfaces corresponding to the yellow exciton series $W_y(\mathbf{p})$, the green series with heavy holes $W_{g, \text{hh}}(\mathbf{p})$, and the green series with light holes $W_{g, \text{lh}}(\mathbf{p})$.

Following this, one chooses the energy surface one wants to investigate and reintroduces it into the Schrödinger equation, resulting in the Hamiltonian for the relative coordinates,

$$\tilde{H} = \frac{\gamma'_1 \mathbf{p}^2}{2m_0} + W_n(\mathbf{p}) - \frac{e^2}{4\pi\epsilon_0\epsilon r}. \quad (5.5)$$

Following the correspondence principle going from quantum mechanical operators to classical observables, the classical dynamics can be calculated by integrating Hamilton's equations of motion for the corresponding Hamilton function.

5.1.1 Formal derivation

We now want to derive the adiabatic approach starting from the Schrödinger equation for the full Hamiltonian (4.54). In momentum space the Schrödinger equation reads

$$\begin{aligned} E\Psi(\mathbf{p}; \mathbf{I}, \mathbf{S}_h) &= H\Psi(\mathbf{p}; \mathbf{I}, \mathbf{S}_h) \\ &= \left(\frac{\gamma'_1 \mathbf{p}^2}{2m_0} + H_{\text{band}}(\mathbf{p}_h, \mathbf{I}, \mathbf{S}_h) + \tilde{V}_C(\mathbf{p}) * \right) \Psi(\mathbf{p}; \mathbf{I}, \mathbf{S}_h) \end{aligned} \quad (5.6)$$

with the convolution

$$\tilde{V}_C(\mathbf{p}) * \Psi(\mathbf{p}; \mathbf{I}, \mathbf{S}_h) = \frac{1}{\sqrt{2\pi\hbar}^3} \int d^3p' \tilde{V}_C(\mathbf{p} - \mathbf{p}') \Psi(\mathbf{p}'; \mathbf{I}, \mathbf{S}_h), \quad (5.7)$$

and the Coulomb potential in momentum space

$$\tilde{V}_C(\mathbf{p}) = \frac{1}{\sqrt{2\pi\hbar}^3} \int d^3r \exp\{-i\mathbf{p}\mathbf{r}/\hbar\} \tilde{V}_C(\mathbf{r}). \quad (5.8)$$

For the ansatz of the wave function we choose a product of the eigenfunctions of the band structure part of the Hamiltonian $\chi_n(\mathbf{p}; \mathbf{I}, \mathbf{S}_h)$ and a function for the motion in the relative coordinate $\phi_n(\mathbf{p})$

$$\Psi(\mathbf{p}; \mathbf{I}, \mathbf{S}_h) = \sum_n \chi_n(\mathbf{p}; \mathbf{I}, \mathbf{S}_h) \phi_n(\mathbf{p}). \quad (5.9)$$

Inserting this ansatz into the Schrödinger equation and multiplying from the left with $\chi_{n'}^*(\mathbf{p}; \mathbf{I}, \mathbf{S}_h)$ gives

$$\left(E - \frac{\gamma'_1 \mathbf{p}^2}{2m_0} - W_n(\mathbf{p})\right) \delta_{n',n} \phi_n = \chi_{n'}^* \tilde{V}_C(\mathbf{p}) * \left(\sum_n \chi_n \phi_n\right). \quad (5.10)$$

While the term on the left is diagonal, the right-hand side of the equation couples the different energy surfaces $W_n(\mathbf{p})$. To further simplify this we acknowledge, that the χ_n are the eigenfunctions for the band structure part of the Hamiltonian H_{band} . Since band structure corrections are employed to accurately model the band structure in the vicinity of the Γ point, the dominant contribution is given by the spin-orbit term (4.50). The eigenfunctions for the spin-orbit term, however, are given by the basis states $|J, m_J\rangle$, meaning that the coefficients $c_{m_I, m_{S_h}}(\mathbf{p})$ in equation (5.4) are just constants, i.e., the Clebsch-Gordon coefficients coupling quasispin $I = 1$ and hole spin S_h to form the corresponding effective hole spin J . Moving away from the Γ point the additional terms in the band Hamiltonian can be seen as a small perturbation. In first order perturbation theory the states should take the form [176]

$$\chi_n \approx |n^0\rangle + \sum_{k \neq n} \frac{\langle k^0 | H_{\text{band}} - H_{\text{SO}} | n^0 \rangle}{\Delta} \left(|k^0\rangle + \sum_{l \neq k} \frac{\langle l^0 | H_{\text{band}} - H_{\text{SO}} | k^0 \rangle}{E_k^1 - E_l^1} |l^0\rangle \right), \quad (5.11)$$

where the states $|n^0\rangle$, $|k^0\rangle$ and $|l^0\rangle$ are chosen such that the degenerate subspaces of the Hamiltonian are diagonalized. The last term is relevant only when one of the $|k^0\rangle$ and $|l^0\rangle$ belongs to the green series with light and the other one to the green series with heavy holes. Since

$$\frac{\langle k^0 | H_{\text{band}} - H_{\text{SO}} | n^0 \rangle}{\Delta} \sim \frac{p_i p_j}{m_0 \Delta} \ll 1 \quad (5.12)$$

in the vicinity of the Γ point, we can consider the χ_n as nearly constant in \mathbf{p} . Since the convolution is associative for the multiplication by a constant factor we can further simplify

$$\tilde{V}_C(\mathbf{p}) * \left(\sum_n \chi_n \phi_n\right) \approx \sum_n \chi_n \tilde{V}_C(\mathbf{p}) * \phi_n. \quad (5.13)$$

The resulting Hamilton operator is diagonal concerning the spin degrees of freedom

$$E \delta_{n',n} \phi_n(\mathbf{p}) = \delta_{n',n} \left(\frac{\gamma'_1 \mathbf{p}^2}{2m_0} + W_n(\mathbf{p}) + \tilde{V}_C(\mathbf{p}) * \right) \phi_n(\mathbf{p}). \quad (5.14)$$

Each exciton series is thus described by an individual Schrödinger equation given through the choice of the corresponding energy surface $W_n(\mathbf{p})$

$$E \phi_n(\mathbf{p}) = \left(\frac{\gamma'_1 \mathbf{p}^2}{2m_0} + W_n(\mathbf{p}) + \tilde{V}_C(\mathbf{p}) * \right) \phi_n(\mathbf{p}). \quad (5.15)$$

These energy surfaces then no longer depend on the spin degrees of freedom but only the operators for the relative motion are relevant. When applying the correspondence principle one arrives at the Hamilton function given by equation (5.5).

5.2 Calculation of energy surfaces

We now want to focus on the calculation of the energy surfaces $W_n(\mathbf{p})$. This can be done by diagonalizing the Hamiltonian H_{band} in a basis for the spin degrees of freedom. The eigenfunctions for the Hamiltonian are given by equation (5.4). Multiplying the eigenvalue equation (5.3) with $\langle m_I, m_{S_h} |$ one arrives at a 6×6 matrix representation of the Hamiltonian leading to the eigenvalue problem

$$\mathbf{H}_{\text{band}}(\mathbf{p})\mathbf{c} = W_n(\mathbf{p})\mathbf{c} \quad (5.16)$$

where the vector \mathbf{c} includes the coefficients $c_{m_I, m_{S_h}}(\mathbf{p})$ from equation (5.4). In general the eigenvalues of a 6×6 matrix can no longer be found analytically. Solutions can then be obtained numerically, e.g., by using an appropriate *LAPACK* routine [177]. This is particularly important for the treatment of magnetoexcitons. Numerical calculations become very time-consuming since for solving Hamilton's equations of motion first derivatives and for the stability matrix even second derivatives need to be evaluated numerically. Without external fields, however, it is possible to exploit Kramers' degeneracy to find analytical expressions for the energy surfaces.

5.2.1 Analytical expressions for the energy surfaces

The expressions for the energy surfaces can be obtained by expanding the band-structure part of the Hamiltonian in a basis for quasispin and hole spin. The eigenvalues of the resulting 6×6 matrix provide the different energy surfaces for the yellow and green exciton series. The characteristic polynomial for this matrix is of degree 6 and takes the form

$$\chi(\lambda) = \lambda^6 + c_5\lambda^5 + c_4\lambda^4 + c_3\lambda^3 + c_2\lambda^2 + c_1\lambda + c_0. \quad (5.17)$$

In general, setting a polynomial equation of degree 5 or higher equal to 0 no solution in radicals can be found. However, for the special case of excitons in cuprous oxide analytical expressions can be obtained by exploiting Kramers' degeneracy. Since every energy surface is twofold degenerate, the characteristic polynomial can be expressed as

$$[W_y(\mathbf{p}) - \lambda]^2 [W_{g, \text{hh}}(\mathbf{p}) - \lambda]^2 [W_{g, \text{lh}}(\mathbf{p}) - \lambda]^2 = 0. \quad (5.18)$$

By comparing the left side of equation (5.18) with equation (5.17) the following system of equations for the energy surfaces can be found, for simplicity we write $W_3 = W_y(\mathbf{p})$,

$W_2 = W_{g,hh}(\mathbf{p})$ and $W_1 = W_{g,lh}(\mathbf{p})$:

$$c_5 = -2(W_1 + W_2 + W_3), \quad (5.19)$$

$$c_4 = (W_1 + W_2 + W_3)^2 + 2W_1W_2 + 2W_1W_3 + 2W_2W_3, \quad (5.20)$$

$$c_3 = -2(W_1^2W_2 + W_1^2W_3 + W_1W_2^2 + W_1W_3^2 + W_2^2W_3 + W_2W_3^2 + 4W_1W_2W_3), \quad (5.21)$$

$$c_2 = W_1^2W_2^2 + W_1^2W_3^2 + W_2^2W_3^2 + 4(W_1^2W_2W_3 + W_1W_2^2W_3 + W_1W_2W_3^2), \quad (5.22)$$

$$c_1 = -2(W_1^2W_2^2W_3 + W_1^2W_2W_3^2 + W_1W_2^2W_3^2), \quad (5.23)$$

$$c_0 = W_1^2W_2^2W_3^2. \quad (5.24)$$

Since there are six equations for three potential surfaces, this system is overdetermined. However, these equations are not independent. To arrive at a solution for the energy surfaces it is therefore sufficient to look at the first three equations (5.19),(5.20) and (5.21). Using these expressions one arrives at a polynomial of degree three for the energy surfaces that needs to vanish

$$W_k^3 + \frac{c_5}{2}W_k^2 + \frac{4c_4 - c_5^2}{8}W_k + \frac{8c_3 - 4c_4c_5 + c_5^3}{16} = 0. \quad (5.25)$$

5.2.2 Solution of cubic polynomial equations

For a general cubic polynomial equation

$$x^3 + ax^2 + bx + c = 0 \quad (5.26)$$

the expression can be transformed to a reduced form by using

$$x = z - \frac{a}{3} \quad (5.27)$$

resulting in

$$z^3 + pz + q = 0 \quad (5.28)$$

with

$$p = b - \frac{a^2}{3}; \quad q = \frac{2a^3}{27} - \frac{ab}{3} + c. \quad (5.29)$$

The solutions for equation (5.28) can be found by applying Cardano's formula [178]

$$z_k = \xi^k \sqrt[3]{-\frac{q}{2} + \sqrt{\frac{q^2}{4} + \frac{p^3}{27}}} + \xi^{-k} \sqrt[3]{-\frac{q}{2} - \sqrt{\frac{q^2}{4} + \frac{p^3}{27}}}, \quad (5.30)$$

with the cubic roots of unity

$$\xi = \frac{-1 + \sqrt{3}i}{2} = e^{i\frac{2\pi}{3}}. \quad (5.31)$$

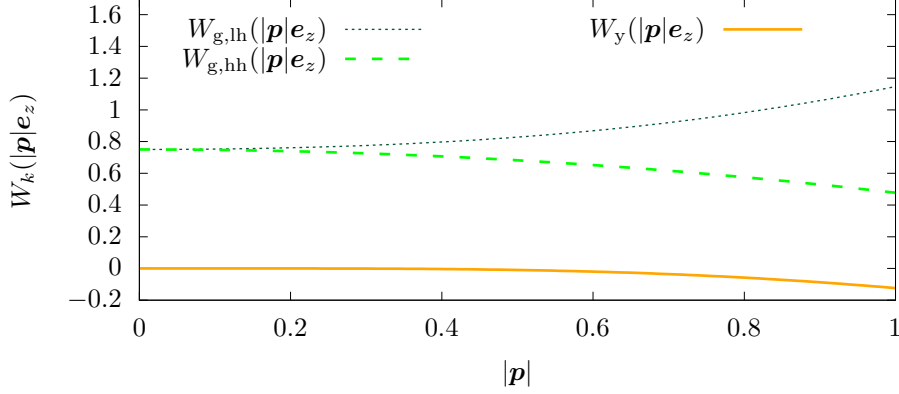


Figure 5.2.: Energy surfaces for momentum aligned with the z axis. The energy surfaces correspond to the green exciton with light holes (glh) and heavy holes (ghh) as well as the yellow series (y). All units are given in exciton-Hartree units. We already have presented similar figures in Refs. [115, 119].

Transforming back using equation (5.27) the energy surfaces then read

$$W_k = -\frac{1}{3} \frac{c_5}{2} + \xi^k C_+ + \frac{-p/3}{\xi^k C_+}, \quad (5.32)$$

with the quantities

$$C_{\pm} = \left(-\frac{q}{2} \pm \sqrt{\frac{q^2}{4} + \frac{p^3}{27}} \right)^{\frac{1}{3}}, \quad (5.33)$$

where p and q are given by the coefficients of the characteristic polynomial c_i

$$p = \frac{c_4}{2} - \frac{5c_5^2}{24}, \quad (5.34)$$

and

$$q = \frac{c_3}{2} - \frac{c_4 c_5}{3} + \frac{5c_5^3}{54}. \quad (5.35)$$

The energy surfaces can be rewritten as

$$W_k = -\frac{1}{3} \frac{c_5}{2} + \xi^k C_+ + \xi^{-k} C_-, \quad (5.36)$$

which is then manifestly real when the radicant in Eq. (5.33) becomes negative. Without the use of complex numbers the real roots of equation (5.25) are given by [178]

$$W_k = -\frac{c_5}{6} + \sqrt{-\frac{4p}{3}} \cos \left[\frac{1}{3} \arccos \left(-\frac{q}{2} \sqrt{-\frac{27}{p^3}} \right) - \frac{2\pi(k-1)}{3} \right]. \quad (5.37)$$

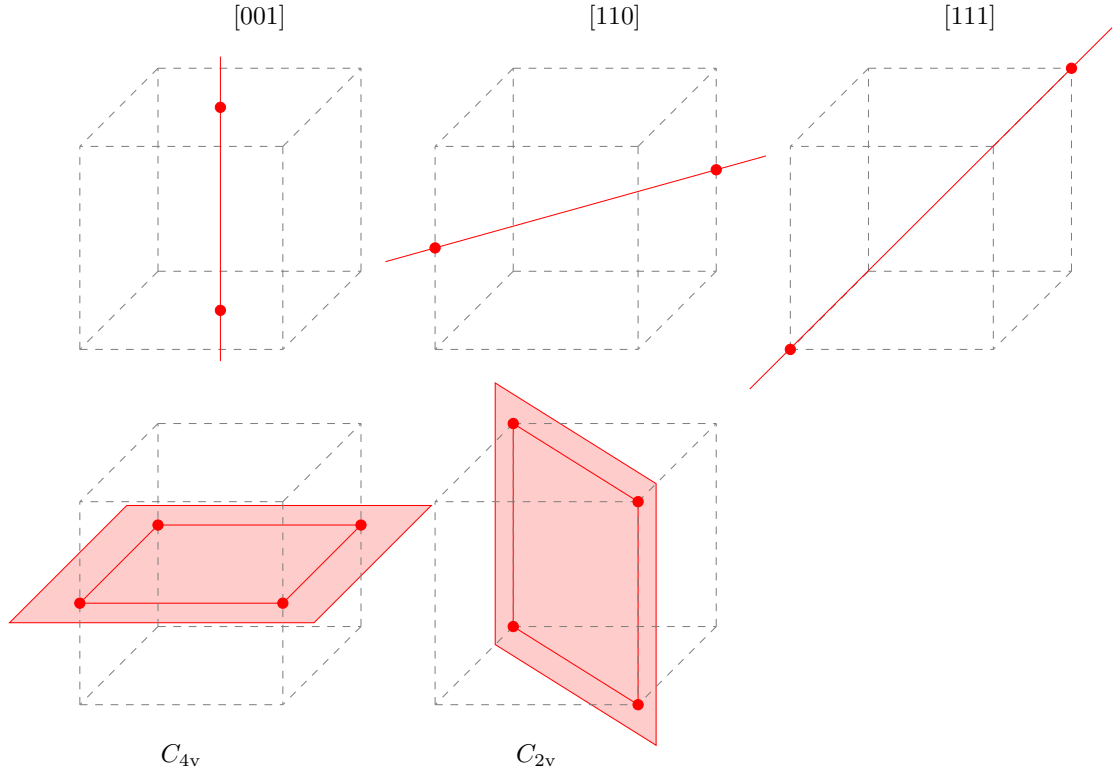


Figure 5.3.: Visualization of the symmetry operations of the cubic O_h group. These include a fourfold rotational axis (top left) as well as a twofold rotational axis (top middle) which are both orthogonal to a corresponding mirror plane (shown below). In addition, a threefold rotational axis (top right) exists.

To calculate the energy surfaces we need the expressions for c_5, p , and q in terms of the momenta \mathbf{p} . These are given in appendix D for the full band-structure Hamiltonian with cubic symmetry. Figure 5.2 shows the three distinct energy surfaces for the momentum oriented along the z axis.

5.2.3 Revisiting the cubic symmetry of cuprous oxide

Since cuprous oxide has the cubic O_h symmetry, this property should be inherited by the energy surfaces

$$W_k(O_h \mathbf{p}) = W_k(\mathbf{p}), \quad (5.38)$$

meaning that the energy surfaces should be invariant under transformations from O_h . To this end we revisit the symmetry operations of the cubic O_h group. The distinct symmetry operations are visualized in figure 5.3. The following symmetry operations

return the cube back onto itself [169]

- The identity E leaves the cube unchanged.
- The inversion I maps the cube onto itself.
- The top left of figure 5.3 shows the rotational axis in $[001]$ direction around which twofold rotations C_2 and fourfold rotations C_4 as well as a fourfold improper rotation S_4 are possible. Below, a mirror plane σ_h normal to the $[001]$ axis is depicted. In addition, there exist two equivalent axis connecting opposing face centers.
- In the top middle of figure 5.3 the rotational axis in $[110]$ direction is shown, which allows for twofold rotations C_2 . Below in the bottom row of figure 5.3 the mirror plane σ_d normal to the $[110]$ axis is shown. This axis has five additional equivalent axes connecting opposing edge centers.
- The top right of figure 5.3 displays the symmetry axis in $[111]$ direction. Around the axis threefold rotations C_3 and sixfold improper rotations S_6 map the cube back onto itself. As can be seen no mirror plane normal to the $[111]$ axis exists. The three additional equivalent axes connect opposite corners.

We now return to the energy surfaces of cuprous oxide. To achieve a two-dimensional representation, we take a look at the symmetry planes normal to $[100]$ and $[1\bar{1}0]$. Figure 5.4 shows the deviation from the spherical symmetry. For this the difference of the value of the energy surface $W_k(\mathbf{p})$ and the corresponding value of the energy surface with the momentum oriented in z direction $W_k(|\mathbf{p}|e_z)$ (presented in figure 5.2) is shown for the three distinct energy surfaces. The plane normal to the $[100]$ is intersected by two mirror planes σ_h connecting the center of opposite edges and two mirror planes σ_d connecting opposite corners on the left of figure 5.4. In addition, the two- and fourfold rotations around the $[100]$ axis are symmetries of the plane. The plane normal to the $[110]$ axis is intersected by one mirror plane σ_h normal to the $[100]$ axis and a mirror plane σ_d normal to the $[110]$ axis. In addition, the twofold rotations around the $[1\bar{1}0]$ axis are still possible. All these symmetries are inherited by the energy surface as can be seen in figure 5.4.

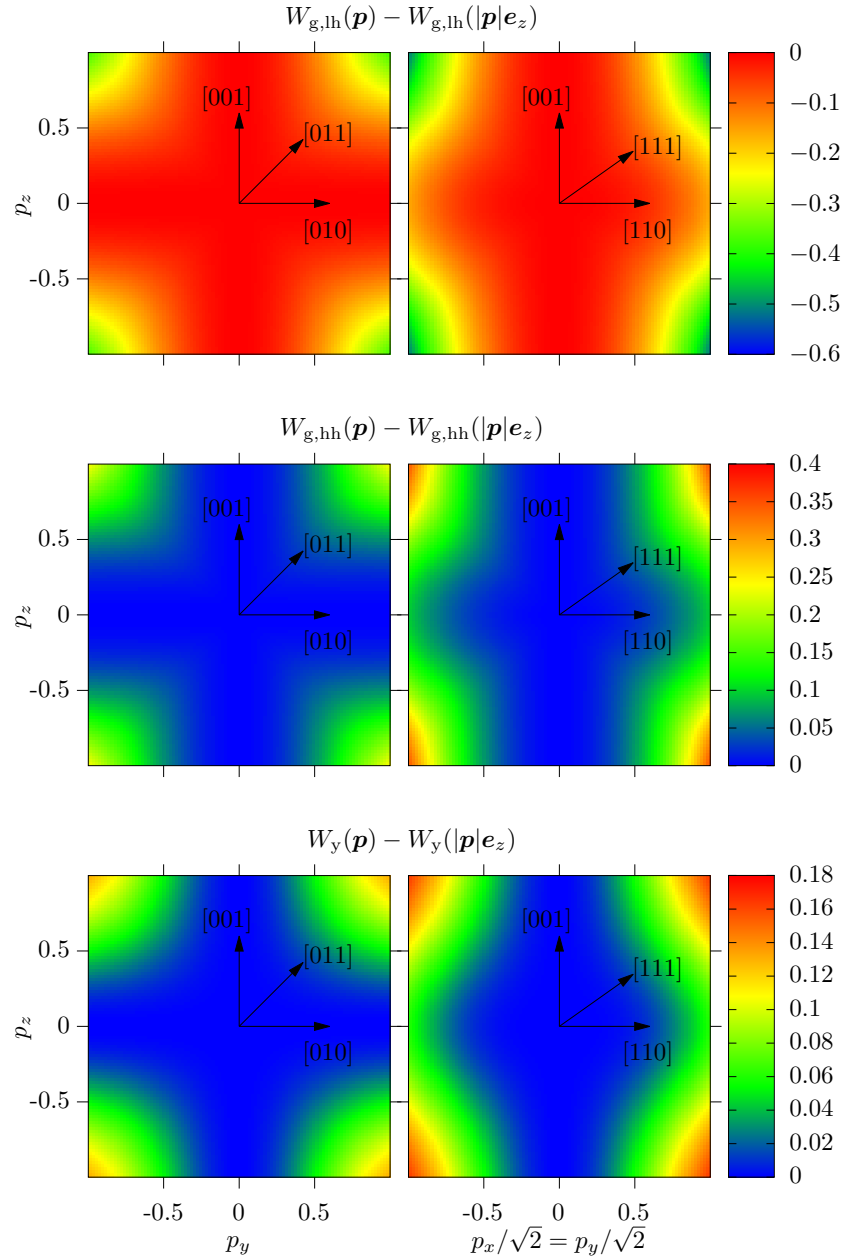


Figure 5.4.: Visualization of the symmetry of the energy surfaces in the plane normal to $[100]$ (left) and normal to $[\bar{1}\bar{1}0]$ (right). The deviation from the corresponding energy surface with momentum aligned with the z axis $W_k(\mathbf{p}) - W_k(|\mathbf{p}|e_z)$ is shown. The C_{4v} symmetry of the plane normal to $[100]$ and the C_{2v} symmetry of the plane normal to $[\bar{1}\bar{1}0]$ becomes apparent. Units are given in exciton-Hartree units. We already have presented similar figures in Refs. [115, 119].

6

Classical dynamics of the yellow exciton series

In this chapter we want to investigate the classical dynamics of the yellow exciton series in cuprous oxide. The classical exciton dynamics of the simple hydrogen-like model with Hamiltonian

$$H_{\text{hyd}} = E_g + \frac{\gamma'_1}{2m_0} \mathbf{p}^2 - \frac{e^2}{4\pi\epsilon_0\epsilon|\mathbf{r}|}, \quad (6.1)$$

is well known. The bound orbits are classical Kepler ellipses, which are obtained as analytical solutions of Hamilton's equations of motion. For the Hamiltonian (6.1) the scaling

$$\mathbf{r} = n_{\text{eff}}^2 \tilde{\mathbf{r}}, \quad \mathbf{p} = \frac{1}{n_{\text{eff}}} \tilde{\mathbf{p}}, \quad (6.2)$$

of the coordinates and momenta with the effective quantum number

$$n_{\text{eff}} \equiv \sqrt{E_{\text{Ryd}}/(E_g - E)}, \quad (6.3)$$

where E_{Ryd} is the exciton Rydberg energy, removes the energy dependence from the Hamiltonian after multiplication with n_{eff}^2 . This means that, up to a scaling of the Kepler ellipses, the classical dynamics is the same at all energies. The situation, however, becomes more complicated when considering the full Hamiltonian (4.54). The additional band structure terms $H_{\text{band}}(\mathbf{p}, \mathbf{I}, \mathbf{S}_h)$ given in equation (4.49), which are neglected in the hydrogen-like model (6.1), depend on the additional degrees of freedom introduced by the quasispin \mathbf{I} and the hole spin \mathbf{S}_h . Note that the spin-orbit term H_{SO} given in Eq. (4.50) disables the scaling procedure described above to remove the energy dependence of the Hamiltonian (4.54).

In this chapter we restrict the analysis of the exciton dynamics to the yellow series described by the classical Hamilton function

$$\mathcal{H} = E_g + \frac{\gamma'_1}{2m_0} \mathbf{p}^2 - \frac{e^2}{4\pi\epsilon_0\epsilon|\mathbf{r}|} + W_y(\mathbf{p}) = E, \quad (6.4)$$

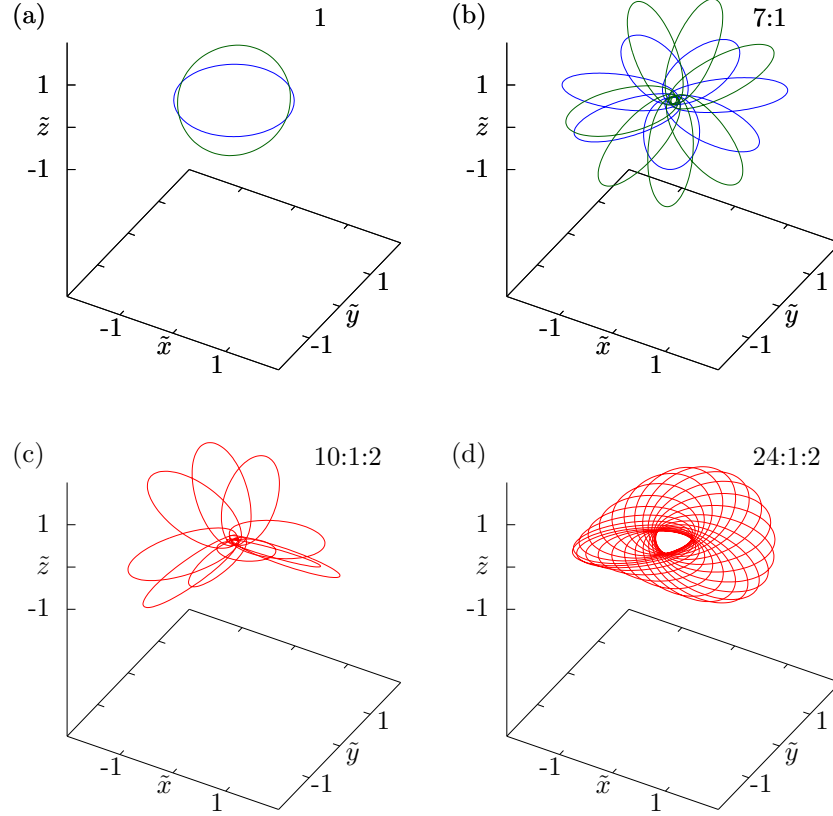


Figure 6.1.: (a) Nearly circular orbits and (b) planar orbits in the two different symmetry planes of the crystal. (c) and (d): Two examples of fully three-dimensional orbits. This figure has already been published in Ref. [121].

with the two-fold degenerate lowest pair of energy surfaces $W_y(\mathbf{p})$. Since the Hamilton function (6.4) only depends on the relative coordinates \mathbf{r} and \mathbf{p} we obtain classical exciton orbits by fixing the energy $E = E_g - E_{\text{Ryd}}/n_{\text{eff}}^2$, i.e., using a fixed value $n_{\text{eff}} = n_0$, and then numerically integrating Hamilton's equations of motion

$$\dot{r}_i = \frac{\gamma'_1}{m_0} p_i + \frac{\partial W_y(\mathbf{p})}{\partial p_i}, \quad \dot{p}_i = -\frac{e^2}{4\pi\epsilon_0\epsilon} \frac{r_i}{|\mathbf{r}|^3}, \quad (6.5)$$

with, e.g., a standard Runge-Kutta algorithm [179].

Due to the additional band structure terms carried by the energy surfaces W_y the spherical $\text{SO}(4)$ symmetry of the hydrogen-like problem is reduced to the cubic O_h

symmetry. For the cubic symmetry nine symmetry planes exist, where a two-dimensional motion is possible. As we have seen in chapter 5 we can distinguish two classes of symmetry planes. The three planes normal to the $[100]$ axis and its equivalents exhibit the same dynamics and likewise the six planes normal to the $[1\bar{1}0]$ axis and its equivalents. In contrast to the hydrogen-like model, where every initial configuration leads to a two-dimensional orbit, three-dimensional orbits are possible when moving the starting configurations out of the symmetry planes. A few examples of periodic orbits are shown in Fig. 6.1. This leads to an intricate phase-space structure for excitons in cuprous oxide. The majority of this chapter has already been published in Refs. [115, 118, 121].

6.1 Classical exciton orbits and PSOS

Since the phase space of the classical exciton dynamics described by the Hamiltonian (6.4) is six-dimensional it cannot easily be visualized. However, the phase space related to the two-dimensional orbits in the symmetry planes normal to the $[100]$ and $[1\bar{1}0]$ axes can be analyzed directly by looking at the corresponding PSOS (see Sec. 2.4.1). For our presentation we choose the (z, p_z) plane, and record the intersection points of orbits when crossing the z axis, i.e., $x = y = 0$. The remaining momenta p_x and p_y are given by the conservation of energy and the choice of the symmetry plane. Such PSOS are shown in Fig. 6.2 for the two different symmetry planes and three different values of n_0 . In all PSOS in Fig. 6.2 one can observe a central fixed point, belonging to a nearly circular orbit shown as inset in the bottom right of the PSOS. This orbit is surrounded by regular tori, which cover the majority of phase space. The outermost parts of the PSOS exhibit small stochastic (chaotic) regions. The area of the chaotic region is larger for the symmetry plane normal to $[1\bar{1}0]$ and decreases with increasing values of n_0 . In the regular, near-integrable regions the two-dimensional orbits are characterized as a secular motion of Kepler ellipses. Here, stable and unstable periodic orbits appear in pairs of elliptic and hyperbolic fixed points in accordance with the Poincaré–Birkhoff theorem as illustrated in the enlarged PSOS in Fig. 6.3.

These periodic orbits can be classified by two integer winding numbers M_1 and M_2 with M_1 the number of Kepler ellipses and M_2 the number of circulations on the torus caused by the secular motion until repetition. Some of them are illustrated in Fig. 6.3 and as insets in Fig. 6.2.

The ratio M_1/M_2 of the winding numbers increases when moving from the outermost part of the PSOS towards the central fixed point, where it takes its maximum value. This is related to a decrease of the eccentricity of the Kepler ellipses and thus to an increase of the angular momentum vector in the direction perpendicular to the symmetry plane. The maximum ratio $(M_1/M_2)_{\max}$ is larger in the symmetry plane normal to $[1\bar{1}0]$ and increases with increasing n_0 . It is important to note that the speed of the secular motion strongly decreases with growing n_0 and thus with growing energy. As can be seen in

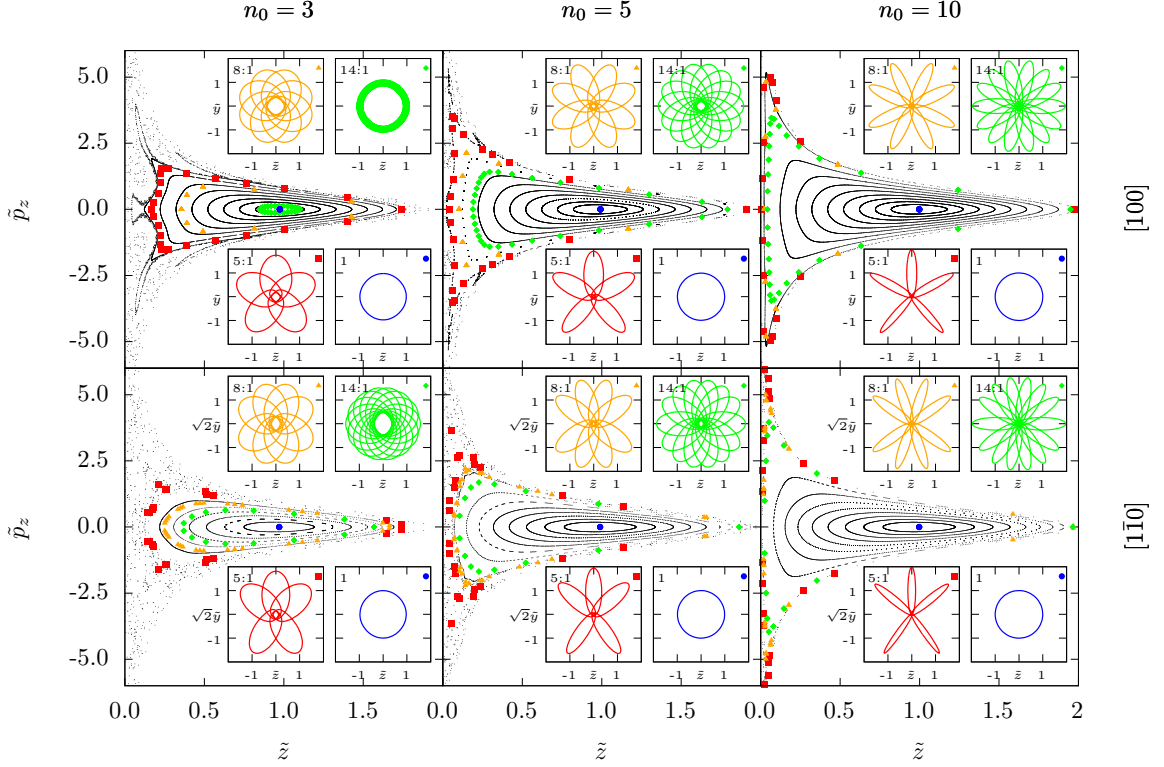


Figure 6.2.: PSOS for the symmetry planes normal to $[100]$ (top row) and normal to $[1\bar{1}0]$ (bottom row) at $n_0 = 3$ (left), $n_0 = 5$ (middle), and $n_0 = 10$ (right). A selection of orbits is shown as insets, labeled by their winding numbers $M_1 = 1$ for the nearly circular orbits and $M_1:M_2$ for the periodic orbits on the two-dimensional tori. Their positions in the PSOS are marked by corresponding symbols. Coordinates and momenta are given in the scaled units (6.2) and thus approximately cover the same range for all values of n_0 . This figure has already been published in Ref. [118].

Fig. 6.2 tori with the same ratio M_1/M_2 of the winding numbers are shifted towards the outer regions of the PSOS with increasing n_0 , which means that the inner regions more and more belong to tori with higher ratios M_1/M_2 related to orbits with slower secular motion, i.e., the band structure of the crystal has a stronger influence on states with low principal quantum numbers and a lower influence on highly excited Rydberg excitons. Furthermore, orbits in the two distinct symmetry planes also differ in their symmetry properties and their orbit parameters. The exciton dynamics outside of the symmetry planes is characterized by three-dimensional orbits, where a secular motion of Kepler ellipses occurs in orientations described by two angles ϑ and φ . Here, periodic orbits can be classified by three winding numbers, where the third winding number M_3

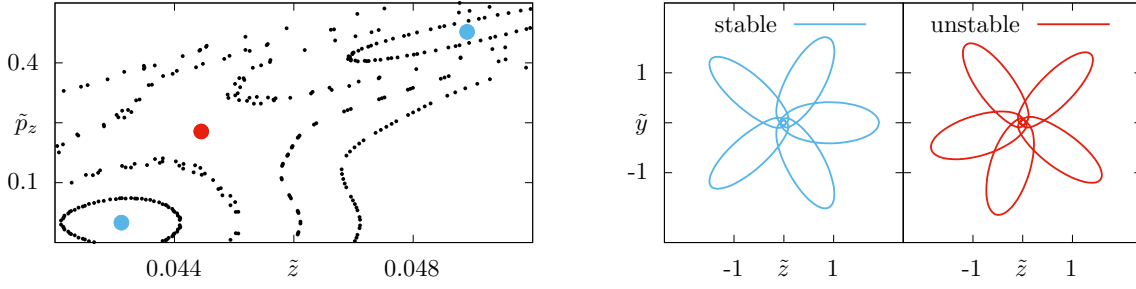


Figure 6.3.: Left: Enlarged part of the PSOS for the plane normal to $[100]$ at $n_0 = 5$, where two fixed points are surrounded by elliptic and hyperbolic structures, respectively. Right: Stable and unstable periodic orbit with winding numbers $M_1:M_2 = 5:1$ corresponding to the two fixed points. Coordinates and momenta are given in the scaled units (6.2). This figure has already been published in Ref. [118].

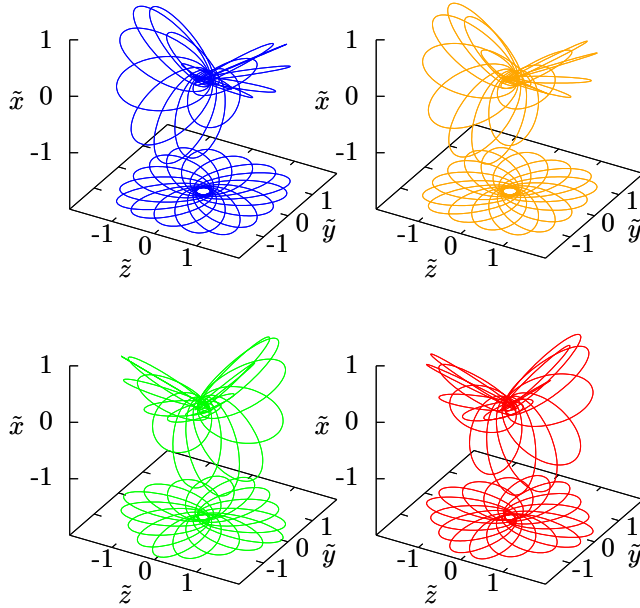


Figure 6.4.: Three-dimensional orbits with winding numbers $M_1:M_2:M_3 = 16:1:2$. Four distinct orbits with different orientation and position of their maxima exist. The projection onto the yz -plane is shown below each orbit. This figure has already been published in Ref. [118].

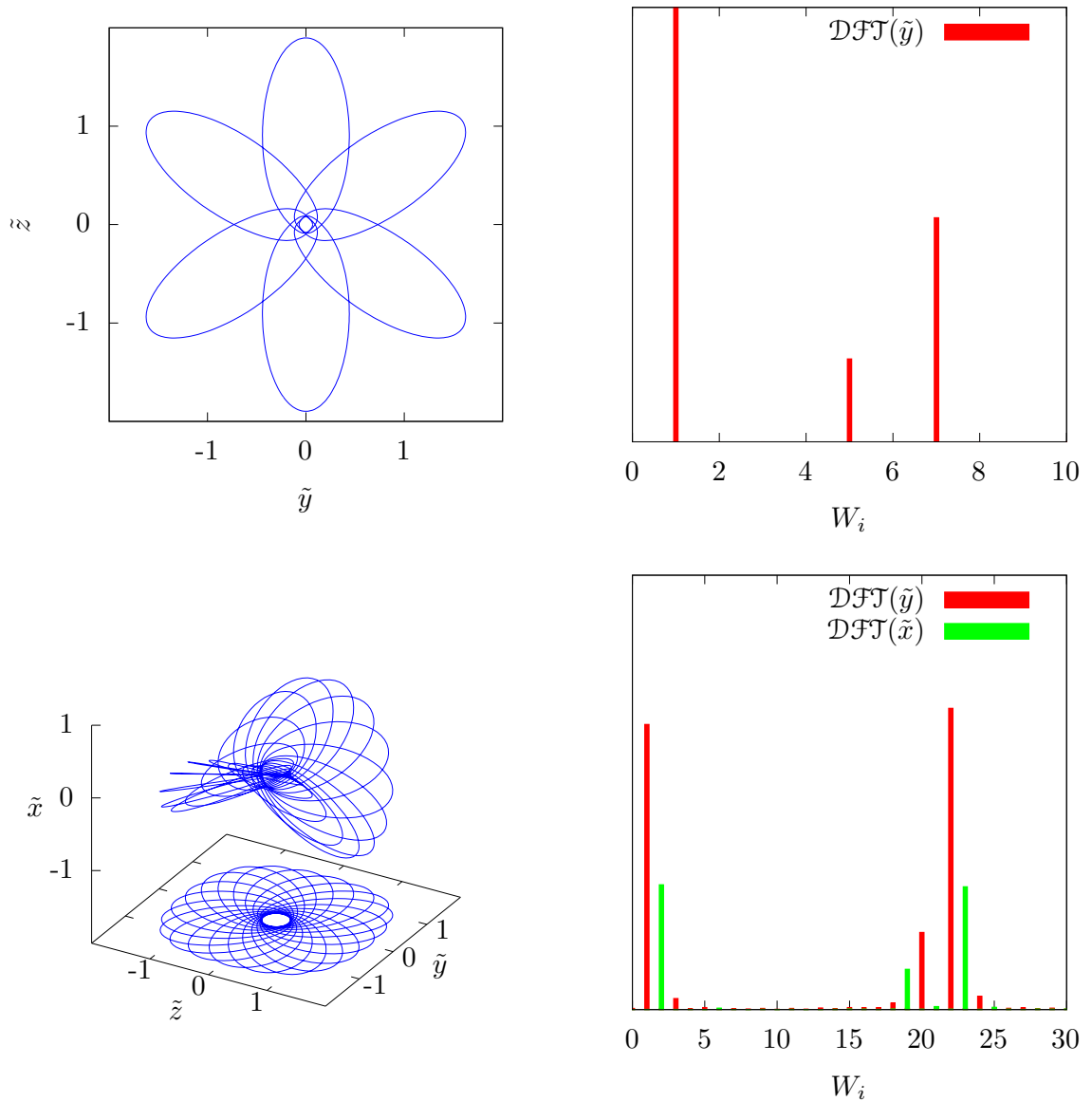


Figure 6.5.: Assignment of winding numbers via the Fourier analysis of orbits. The discrete Fourier transform (\mathcal{DFT}) of the coordinates exhibits peaks at frequencies W_i which can be used to extract the winding numbers M_i . The $\mathcal{DFT}(\tilde{z})$ shows the same behavior as $\mathcal{DFT}(\tilde{y})$ and is thus omitted.

counts the cycles of the secular motion in the additional direction compared to the two-dimensional case. The orbits appear in sets of four distinguished variants, not counting rotations and reflections of the same orbit within the O_h symmetry group. A quadruple

of three-dimensional orbits with $n_0 = 5$ and winding numbers $M_1:M_2:M_3 = 16:1:2$ is illustrated in Fig. 6.4. The projection of the three-dimensional orbits onto the yz plane looks similar to the corresponding two-dimensional orbits, where the orbits in the same column show comparable behavior. The orbits in the same row have identical orientation towards a symmetry plane of the crystal. The orbits in the upper row appear folded towards the plane normal $[001]$, whereas the orbits in the lower row are oriented towards the plane normal to $[011]$.

The assignment of winding numbers can be confirmed by using similar techniques as in Refs. [35, 180]. To this end we perform a Fourier analysis of the periodic orbit coordinate functions $r_i(t)$. In the Fourier space, peaks can be observed at positions $W_1 = \pm M_2 + nM_1$ with $n \in \mathbb{Z}$ for the two-dimensional orbits, for three-dimensional a second class of peaks can be observed at positions $W_2 = \pm M_3 + nM_1$, confirming our assignment of winding numbers.

6.2 Stability properties of periodic orbits

For the nearly circular orbits the values of $\lambda_i + 1/\lambda_i$ as functions of n_0 are shown in Fig. 6.6. For both orbits the stability in the symmetry plane (red and green curves) is almost identical. Looking at the direction out of the plane the behavior differs. The nearly circular orbit in the plane normal to $[100]$ is stable and the orbit normal to $[1\bar{1}0]$ is unstable against perturbations out of the symmetry planes.

For the two-dimensional orbits a similar behavior can be observed. Orbits in the plane normal to $[1\bar{1}0]$ are unstable against perturbations of the orbits out of the plane, whereas the orbits in the symmetry plane normal to $[100]$ are mostly stable. This can be seen in Fig. 6.7, where the sums $\lambda_i + 1/\lambda_i$ for the directions orthogonal to the orbit are shown for $n_0 = 3, 5$, and 10 . Regarding perturbations within the symmetry plane, for a given ratio M_1/M_2 two partner orbits exist, one stable and one unstable, as already discussed above (see the elliptic and hyperbolic fixed points in Fig. 6.3). The largest deviation from $\lambda_{\parallel} = 1$ is found at low ratios M_1/M_2 , where the influence of the band structure terms on the orbits becomes more pronounced. The strongest effect occurs for orbits exhibiting high symmetry, which are the shortest orbits in the fundamental region.

The stability eigenvalues of the two orbits with the same ratio M_1/M_2 against perturbations out of the symmetry plane are nearly identical and mostly located in the stable region, i.e., $|\lambda_{\perp} + 1/\lambda_{\perp}| \leq 2$. However, for the stability properties in the symmetry plane only the orbits with a low ratio M_1/M_2 show deviations from the integrable behavior characterized by $\lambda_{\parallel} = 1$ and for $n_0 = 3$ no deviations can be observed at all. We observe a similar behavior for the periodic orbits in the other symmetry plane and for the three-dimensional orbits.

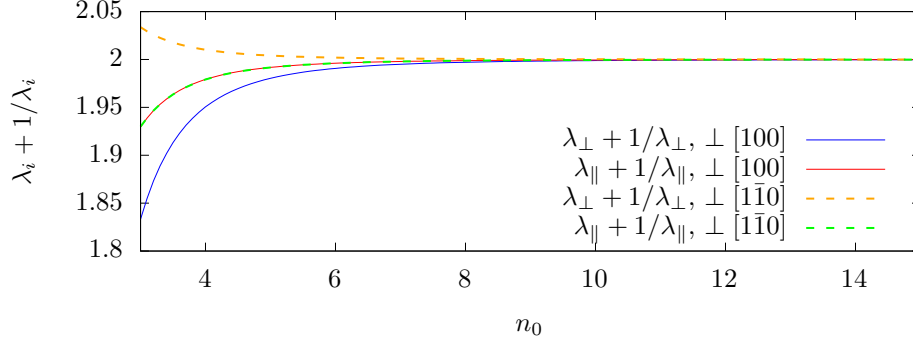


Figure 6.6.: Sum $\lambda_i + 1/\lambda_i$ for the nearly circular orbits in the different symmetry planes, where λ_{\parallel} and λ_{\perp} describe the stability of the orbits in the plane and out of the plane, respectively. The directions normal to the symmetry plane are stable for the plane normal to $[100]$ (blue curve) and unstable for the plane normal to $[1\bar{1}0]$ (orange curve). Both orbits are stable with respect to perturbations in the plane with almost identical stability eigenvalues λ_{\parallel} (red and green curves). This figure has already been published in Ref. [118].

6.3 Action and ordering scheme for orbits in cuprous oxide

To connect the classical trajectories to quantum properties of the system the action S of classical orbits is needed. It can be calculated by integrating the corresponding equation of motion

$$\frac{d}{dt}S = \mathbf{p} \frac{d\mathbf{r}}{dt} \quad (6.6)$$

along the orbit.

The structure of the classical exciton dynamics is illustrated in more detail in Fig. 6.8, where on the left the classical action \tilde{S}_{po} of the periodic orbits is shown as function of the ratio of the winding numbers M_1/M_2 . For better visibility, the actions are normalized by the actions $\tilde{S}_{\perp[1\bar{1}0]}$ of the corresponding orbits with the same winding numbers M_1 and M_2 in the plane perpendicular to the $[1\bar{1}0]$ axis. Therefore, by construction, the periodic orbits in the plane perpendicular to the $[1\bar{1}0]$ axis are located on the straight line at $\tilde{S}_{\text{po}}/\tilde{S}_{\perp[1\bar{1}0]} = 1$. These orbits lie on a 2D torus in phase space. With increasing ratio M_1/M_2 they converge at $M_1/M_2 \approx 67.8$ to the nearly circular orbit in the symmetry plane perpendicular to $[1\bar{1}0]$. This point in Fig. 6.8 (left) thus represents a limiting 1D torus in phase space indicated by the green rhombus. Similarly, the periodic orbits perpendicular to the $[100]$ axis, lying on a different 2D torus in phase space, are located

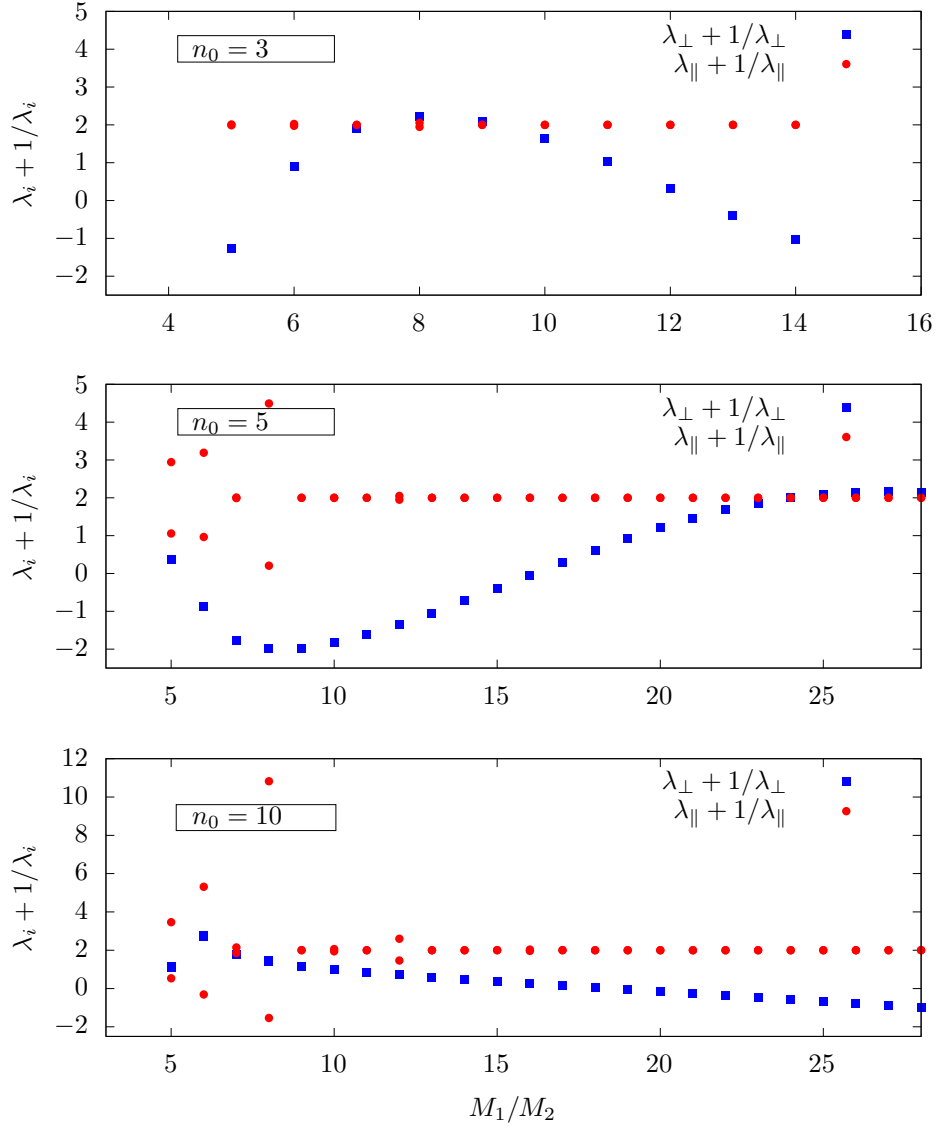


Figure 6.7.: Sum $\lambda_i + 1/\lambda_i$ for the two-dimensional orbits in the plane normal to $[100]$ for $n_0 = 3$ (top), $n_0 = 5$ (middle), and $n_0 = 10$ (bottom). λ_{\parallel} describes the stability of the orbits in the plane, λ_{\perp} describes the stability of the orbits out of the plane. This figure has already been published in Ref. [118].

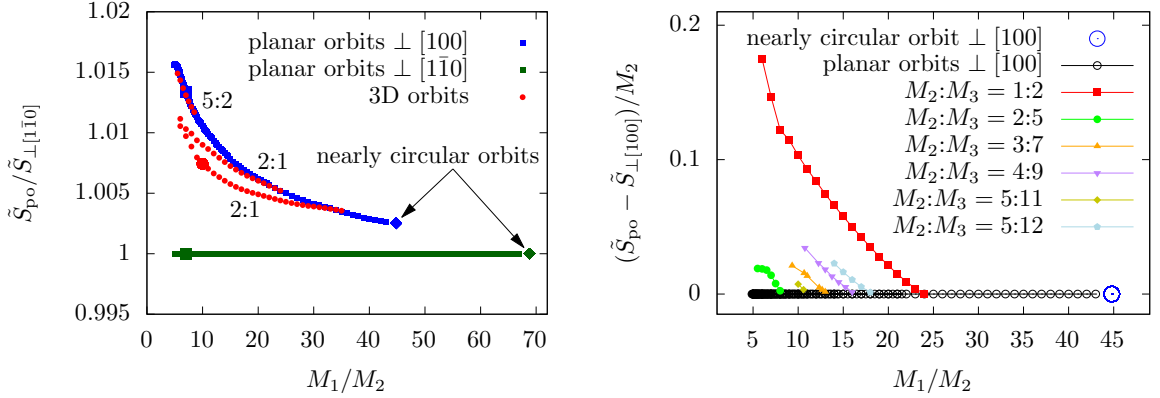


Figure 6.8.: Left: Actions \tilde{S}_{po} of periodic orbits as function of the ratio of winding numbers M_1/M_2 . The actions are normalized by the actions $\tilde{S}_{\perp[110]}$ of the corresponding orbits with the same winding numbers M_1 and M_2 in the plane perpendicular to the $[1\bar{1}0]$ axis. The two-dimensional orbits approach the action of the nearly circular orbit (indicated by rhombi) of the corresponding plane with increasing M_1/M_2 . Some three-dimensional orbits with marked ratio $M_3:M_2$ are located between the area enclosed by orbits in the two different symmetry planes of the O_h group. The orbits shown in Fig. 6.1 are highlighted by larger symbols. Right: Difference of the action \tilde{S}_{po} of the periodic orbits (po) at $n_0 = 5$ and the corresponding two-dimensional orbits $\tilde{S}_{\perp[100]}$ in the plane normal to $[100]$ normalized by their winding number M_2 over the ratio of winding numbers M_1/M_2 . Six different series of three-dimensional orbits with winding numbers $M_2:M_3$ are shown as solid points, connected by lines to guide the eye. The action of two-dimensional orbits in the plane normal to $[100]$ provides a lower border for the families of three-dimensional orbits. For increasing ratio M_1/M_2 the nearly circular orbit (indicated by a blue circle) is reached. Both parts of this figure have already been published in Refs. [118, 121].

on the upper line in Fig. 6.8 (left) with the limiting nearly circular orbit on a 1D torus at $M_1/M_2 \approx 43.8$ shown as blue rhombus. In between the orbits on the two limiting 2D tori the periodic orbits on the 3D tori are located. Subsets of these orbits with winding number $M_2 = 1$ or 2 and ratios $M_3:M_2 = 2:1$ or $5:2$ are marked by red dots in Fig. 6.8 (left). The three-dimensional orbits fill the area between the limiting 2D tori more densely when longer periodic orbits with more complicated ratios of the winding numbers are considered. As can be seen in Fig. 6.8 (left), the classical action of periodic orbits with the same winding numbers M_1 and M_2 differ by less than 2%. Here, the orbits with the highest action belong to the two-dimensional orbits in the (mostly)

stable symmetry plane perpendicular to the $[100]$ axis and its equivalents. At slightly lower action one finds unstable three-dimensional orbits, and the lowest action of the cluster belongs to a two-dimensional orbit in the plane perpendicular to the $[1\bar{1}0]$ axis.

On the right of Fig. 6.8 the difference of the action to the one of two-dimensional orbits in the plane normal to $[100]$ normalized by the second winding number M_2 is plotted over the ratio M_1/M_2 of the first two winding numbers at $n_0 = 5$ for selected pairs of winding numbers $M_2:M_3$. Different values of n_0 lead to qualitatively similar pictures. Note that additional orbits with other pairs of winding numbers $M_2:M_3$ would fill a finite dense area in Fig. 6.8 (right). With increasing ratio M_1/M_2 the three-dimensional orbits approach the zero line, where the two-dimensional orbits are located and disappear when this line is reached. The ratio M_1/M_2 where this is happening for the orbits with $M_2:M_3 = 1:2$ corresponds to the region in Fig. 6.7 where $|\lambda_i + 1/\lambda_i| \rightarrow 2$. A crossing of the line $|\lambda_i + 1/\lambda_i| = 2$ indicates a change of stability properties, which is connected to a bifurcation of the respective orbit. Similarly, the eigenvalues of two-dimensional orbits with higher values of M_2 approach $\lambda_i = 1$ where the corresponding three-dimensional orbits disappear. Thus, the two-dimensional orbits constitute a boundary for the three-dimensional orbits. For increasing values of the ratio M_1/M_2 these orbits approach the action of the nearly circular orbit in the plane normal to $[100]$ marked by a blue circle at $M_1/M_2 \approx 43.8$ in Fig. 6.8 (right).

6.4 Calculation of action variables

The periodic orbits on the rational tori observed in Fig. 6.2 can be characterized by two integer rotation numbers (M_1, M_2) , where M_1 describes the number of Rydberg cycles of the orbit and M_2 is the number of rotations of these cycles around the x axis. The classical action of the periodic orbits is given as

$$S_{M_1, M_2} = 2\pi M_1 I_1 + 2\pi M_2 I_2, \quad (6.7)$$

where I_1 and I_2 are the action variables of the torus, which smoothly depend on the energy and the ratio M_1/M_2 of the rotation numbers. The ratio M_1/M_2 increases from the outermost tori towards the central fixed point of the PSOS. This is related to a growing angular momentum of the classical orbits, i.e., orbits in the outermost (chaotic) part of the PSOS have low angular momenta and the nearly circular orbit belonging to the central fixed point has the highest angular momentum.

Using Eq. (6.7) and its derivative $dS_{M_1, M_2}/dM_1 = 2\pi I_1$, which can be well approximated by a differential quotient for two consecutive periodic orbits with rotation numbers M_1 differing by 1, the action variables I_1 and I_2 can be constructed for the rational tori and interpolated for the irrational tori. The action variables I_1 and I_2 at $n_0 = 5$ as a function of the ratio M_1/M_2 are presented in Fig. 6.9 for the plane normal to $[100]$. They behave monotonically in the finite region between $M_1/M_2 \approx 5.5$, which is close

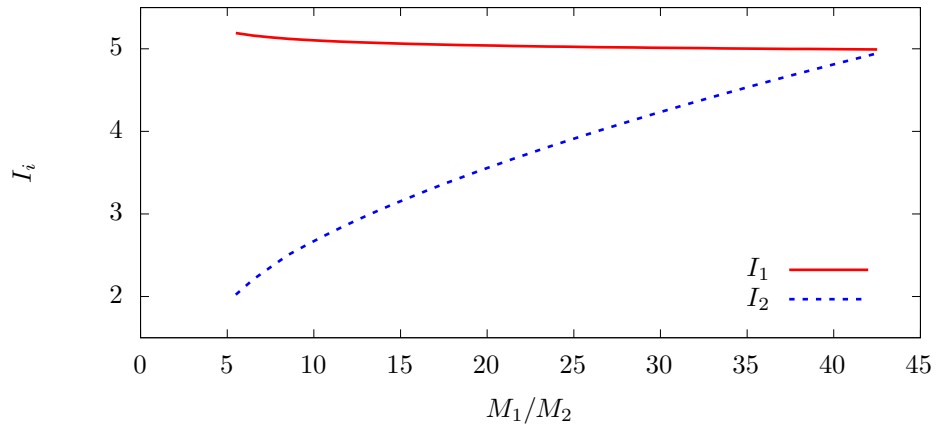


Figure 6.9.: Action variables I_1 and I_2 of the orbits in the plane normal to $[100]$ as functions of the ratio M_1/M_2 of the winding numbers. This figure has already been published in Ref. [115].

to the border of the regular tori [see Fig. 6.2] and $M_1/M_2 \approx 43.8$ related to the central elliptical fixed point in the PSOS. For the nearly circular periodic orbit the two action variables coincide, i.e., it is $I_1 = I_2$ at the fixed point. In principle this technique can also be extended to construct the action variables of three-dimensional orbits.

7

Evidence for the existence of exciton orbits in quantum spectra

In chapter 6 we have presented the classical dynamics for the yellow exciton series obtained via an adiabatic approach. The question remains whether quantum mechanical properties of the system can be understood in terms of these classical orbits. We want to address the question in this chapter. The majority of this chapter has been published in Refs. [118, 121]

7.1 Systems with scaling property

The amplitudes in Gutzwiller's trace formula (3.37) as well as in the Berry-Tabor-formula (3.24) depend on the energy or even additional parameters like external fields through the orbit parameters. In some systems it is possible to perform a scaling operation in such a way that the classical orbits no longer depend on a scaling parameter

$$w = \frac{1}{\hbar_{\text{eff}}} = \frac{n_{\text{eff}}}{\hbar}. \quad (7.1)$$

The action

$$S_{\text{po}}(w)/\hbar = \tilde{S}_{\text{po}}w, \quad (7.2)$$

then only depends linearly on the scaling parameter w with the constant scaled action \tilde{S}_{po} . Examples where such scaling techniques have been applied are billiard systems [181] or the hydrogen atom in a magnetic field [31, 120, 182]. Transforming the semiclassical density of states from energy to w domain the resulting expression

$$d_{\text{sc}}(w) = \bar{d}(w) + \text{Re} \sum_{\text{po}} \mathcal{A}_{\text{po}} \exp\left(i\tilde{S}_{\text{po}}w\right), \quad (7.3)$$

can be understood as a Fourier series with constant periodic orbit parameters. For convenience, the Maslov index α_{po} is contained in a complex valued amplitude \mathcal{A}_{po} .

The individual periodic orbits provide sinusoidal fluctuations to the density of states, which cannot be observed directly. However, the contributions of the periodic orbits can be revealed by Fourier transform from w to the scaled action domain. The obtained recurrence spectra

$$C_{\text{sc}}(\tilde{S}) = \sum_{\text{po}} \mathcal{A}_{\text{po}} \delta(\tilde{S} - \tilde{S}_{\text{po}}), \quad (7.4)$$

exhibit delta peaks at scaled actions \tilde{S}_{po} which allows for a direct assignment of individual orbits to the quantum mechanical recurrence spectrum.

7.2 Scaling technique for excitons in cuprous oxide

Here we apply the scaling technique to the classical exciton orbits in cuprous oxide. For all bound states of a hydrogen-like Rydberg spectrum, the scaling property (6.2) holds. The corresponding classical orbits are Kepler ellipses, and thus the classical phase space structure does not depend on the energy of the Rydberg states. However, the classical dynamics corresponding to a given exciton state depends on the energy. This can be seen when applying the scaling (6.2) to the Hamiltonian (4.54). After multiplying by n_{eff}^2 the Hamiltonian reads

$$H = H_{\text{kin}}(\tilde{\mathbf{p}}, \hat{\mathbf{I}}, \hat{\mathbf{S}}_{\text{h}}) + n_{\text{eff}}^2 H_{\text{SO}}(\hat{\mathbf{I}}, \hat{\mathbf{S}}_{\text{h}}) - \frac{e^2}{4\pi\epsilon_0\epsilon|\tilde{\mathbf{r}}|}. \quad (7.5)$$

Thus, the impact of the spin-orbit coupling on the states varies with energy. This dependence can be avoided by application of a scaling technique to the spin-orbit coupling. We apply a scaling technique to the spin-orbit term H_{SO} by replacing the coupling constant Δ in Eq. (4.50) with an energy-dependent coupling parameter $\tilde{\Delta}$, i.e.,

$$\Delta \rightarrow \tilde{\Delta} = \frac{n_0^2}{n_{\text{eff}}^2} \Delta, \quad (7.6)$$

where the constant parameter n_0 describes the strength of the scaled spin-orbit coupling. While changing material parameters as in Eq. (7.6) is not directly possible in an experiment, it can prove useful in theoretical investigations. A tunable spin-orbit coupling Δ has already been used to study the exchange interaction in the yellow exciton series [89].

7.3 Calculation of the trace formula amplitudes

Due to the energy surface $W_y(\mathbf{p})$ the dynamics of the excitons in cuprous oxide is not integrable. For such systems the density of states is given by Gutzwiller's trace formula (3.37). Applying the scaling technique for the spin-orbit coupling (7.6) the amplitudes in Gutzwiller's trace formula read

$$|\mathcal{A}_{\text{po}}| = \frac{1}{\pi\hbar} \frac{\tilde{S}_{\text{ppo}}}{\sqrt{|(\lambda_{\perp} + 1/\lambda_{\perp} - 2)(\lambda_{\parallel} + 1/\lambda_{\parallel} - 2)|}}. \quad (7.7)$$

Note that in the scaled system the period T_{ppo} must be replaced by the scaled action \tilde{S}_{ppo} [120]. For the isolated nearly circular orbits the stability eigenvalues λ_{\perp} and λ_{\parallel} differ from one, and Eq. (7.7) can be directly evaluated. The periodic orbit parameters and amplitudes for one cycle of these orbits with $n_0 = 3, 5,$ and 10 are given in table 7.1.

For the calculation of the amplitudes of the two- and three-dimensional orbits Eq. (7.7), however, is not applicable since the majority of orbits exhibit eigenvalue pairs close to $\lambda = 1$, which would lead to the divergence of the amplitude. For many orbits we find one eigenvalue pair with λ (and thus $1/\lambda$) close to one. The corresponding degree of freedom can be handled by application of the Berry-Tabor formula (3.28). The second eigenvalue pair λ_{po} significantly differs from $\lambda_{\text{po}} = 1$, and here the corresponding degree of freedom can be handled by application of Gutzwiller's trace formula (3.37). When combining the two semiclassical expressions we arrive at the semiclassical amplitude

$$|\mathcal{A}_{\text{po}}| = \frac{1}{\pi\hbar} \frac{1}{\sqrt{|\lambda_{\text{po}} + 1/\lambda_{\text{po}} - 2|}} \frac{\tilde{S}_{\text{po}}}{\sqrt{\hbar M_2^3 |g_E''|}}. \quad (7.8)$$

Table 7.1.: Periodic orbit parameters and Gutzwiller amplitudes for the nearly circular orbits in the planes \perp to $[100]$ and $[1\bar{1}0]$.

n_0	plane	$\tilde{S}_{\text{po}}/(2\pi)$	$\lambda_{\perp} + 1/\lambda_{\perp}$	$\lambda_{\parallel} + 1/\lambda_{\parallel}$	$ \mathcal{A}_{\text{po}} $
3	$[100]$	1.0086	1.8333	1.9295	18.6128
3	$[1\bar{1}0]$	1.0033	2.0338	1.9299	41.2599
5	$[100]$	0.9983	1.9803	1.9917	157.0315
5	$[1\bar{1}0]$	0.9965	2.0041	1.9917	343.0293
10	$[100]$	0.9942	1.9988	1.9995	2619.0137
10	$[1\bar{1}0]$	0.9938	2.0002	1.9995	5671.3482

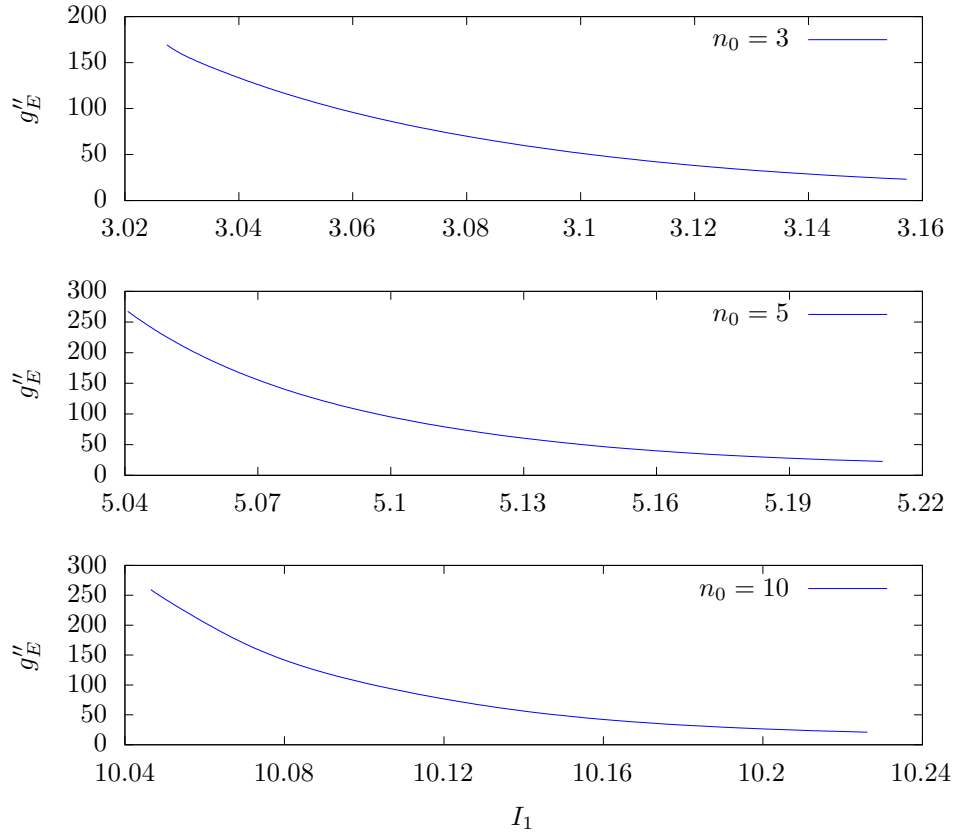


Figure 7.1.: Second derivative of the function $I_2 = g_E(I_1)$ with respect to I_1 for the two-dimensional orbits in the plane normal to $[100]$ at $n_0 = 3$ (top), 5 (middle), and 10 (bottom). This figure has already been published in Ref. [118].

The calculation of the semiclassical amplitudes (7.8) requires the knowledge of the function g''_E discussed in Sec. 3.1. For the two-dimensional orbits the action variables I_1 and I_2 defining the function $I_2 = g_E(I_1)$ are constructed with the help of derivatives of the classical action

$$S_M = 2\pi(M_1 I_1 + M_2 I_2), \quad (7.9)$$

with respect to the respective winding number M_i . The derivatives are obtained numerically via difference quotients of periodic orbits with consecutive winding numbers. For the three-dimensional orbits an effective two-dimensional description can be obtained by combining the contributions of the secular motion in φ - and ϑ -direction described by the greatest common divisor $\tilde{M}_2 = \text{GCD}(M_2, M_3)$ giving the action variable $\tilde{I}_2 = (M_2/\tilde{M}_2)I_2 + (M_3/\tilde{M}_2)I_3$. With the two action variables at hand, the function g''_E is obtained with Eq. (3.27) by differentiating I_2 two times with respect to I_1 . In Fig. 7.1 this is illustrated for the two-dimensional orbits in the plane normal to $[100]$ at

$n_0 = 3, 5,$ and 10 . This then allows for calculation of the amplitudes for the two and three-dimensional orbits. For the outermost part of the PSOS amplitudes can also be calculated using expressions for mixed regular chaotic systems [183]. These are however only applicable when the partner orbits are sufficiently well separated, which for the yellow series is only the case for the orbits close to the chaotic region. For these orbits a comparison to the amplitudes obtained by our heuristic expression (7.8) show good agreement [184].

7.4 Verification of exciton orbits in quantum spectra

Exciton spectra described by the Hamiltonian (4.54) have already been investigated experimentally [43] and theoretically [46, 53, 60]. Here, we want to reveal the existence of classical exciton orbits in quantum spectra of the yellow exciton series of cuprous oxide. For this aim we now exploit the scaling property introduced in Sec. 7.2 by using the scaled spin-orbit splitting (7.6) in quantum computations. The semiclassical analysis of Fourier transform quantum recurrence spectra then allows for the observation of signatures of classical exciton orbits and a detailed study of the energy dependence of the exciton dynamics in the quantum spectra.

7.4.1 Scaled exciton spectra

For the quantum mechanical description of the scaled system obtained by replacing the spin-orbit coupling in Eq. (7.5) with the scaled version (7.6) we need to find the expression for the operators in the scaled coordinates (6.2). In quantum mechanics the components of coordinates and momenta must satisfy the canonical commutation relations

$$[\hat{r}_i, \hat{p}_j] = i\hbar\delta_{ij}. \quad (7.10)$$

Inserting the scaled variables (6.2) into Eq. (7.10) yields the commutation relations

$$[\hat{\tilde{r}}_i, \hat{\tilde{p}}_j] = i\frac{\hbar}{n_{\text{eff}}}\delta_{ij}, \quad (7.11)$$

in the scaled coordinates, where now the Planck constant is replaced by an effective Planck constant

$$\hbar_{\text{eff}} = \hbar/n_{\text{eff}}. \quad (7.12)$$

The operators in coordinate space then take the form

$$\hat{\tilde{\mathbf{r}}} = \tilde{\mathbf{r}}, \quad \hat{\tilde{\mathbf{p}}} = -i\hbar_{\text{eff}}\nabla_{\tilde{\mathbf{r}}}. \quad (7.13)$$

In the scaled picture the Schrödinger equation can now be transformed to the generalized eigenvalue problem

$$\left[\frac{e^2}{4\pi\epsilon_0\epsilon|\tilde{\mathbf{r}}|} - n_0^2 H_{\text{SO}}(\hat{\mathbf{I}}, \hat{\mathbf{S}}_h) - E_{\text{Ryd}} \right] |\Psi\rangle = \frac{\hbar^2}{n_{\text{eff}}^2} H_{\text{kin}}(-i\nabla_{\tilde{\mathbf{r}}}, \hat{\mathbf{I}}, \hat{\mathbf{S}}_h) |\Psi\rangle \quad (7.14)$$

for the effective Planck constant $\hbar_{\text{eff}} = \hbar/n_{\text{eff}}$ (or the effective quantum number n_{eff}). The classical dynamics does not depend on the Planck constant, which means that for a given n_0 the classical dynamics is the same for all eigenvalues $n_{\text{eff},i}$. This allows us to reveal contributions of the classical exciton dynamics to the quantum mechanical recurrence spectra obtained via Fourier transform of the scaled exciton spectra. The quantum theoretical calculations were performed by Patric Rommel and Moritz Schumacher [185]. Details on the numerical calculation can be found in our publication [118].

7.4.2 Quantum recurrence spectra

We now want to uncover the contributions of classical orbits directly in the scaled quantum spectra

$$d(n_{\text{eff}}) = \sum_i \delta(n_{\text{eff}} - n_{\text{eff},i}). \quad (7.15)$$

The eigenvalues of the scaled Schrödinger equation (7.14) are shown in Fig. 7.2 for $n_0 = 3, 5,$ and 10 , where n_0 parameterizes the scaled classical dynamics, as shown in the PSOS in Fig. 6.2, i.e., spectra with increasing n_0 are related to a classical exciton dynamics with slower secular motion of orbits. The lowest axis label in Fig. 7.2 gives the eigenvalues n_{eff} and the upper labels of the individual plots compare the scaled spin-orbit coupling $\tilde{\Delta}$ to the real physical value Δ , i.e., $\tilde{\Delta}/\Delta = 1$ belongs to the crystal with the real (unscaled) material parameters of cuprous oxide.

As outlined in Sec. 7.2 the scaled density of states (7.15) can be approximated by a superposition of sinusoidal fluctuations, whose amplitudes and frequencies are directly related to properties of the periodic orbits of the underlying classical dynamics. Thus, we analyze the fluctuations of the scaled quantum spectrum (7.15) via Fourier transform in the variable n_{eff} , i.e., a quantum recurrence spectrum is obtained as

$$C(S) = \frac{1}{2\pi} \int d(n_{\text{eff}}) e^{-i\tilde{S}n_{\text{eff}}/\hbar} dn_{\text{eff}}. \quad (7.16)$$

The quantum recurrence spectrum (7.16) should provide peaks at frequencies given by the scaled actions \tilde{S}_{po} of the periodic orbits of the associated classical exciton dynamics. Due to the finite number of converged states obtained from numerically solving the generalized eigenvalue problem (7.14) the peaks appear broadened in comparison to the full (infinite) spectrum. This can also be understood in the following way. The finite spectrum can be obtained by multiplying the infinite one with a rectangular window

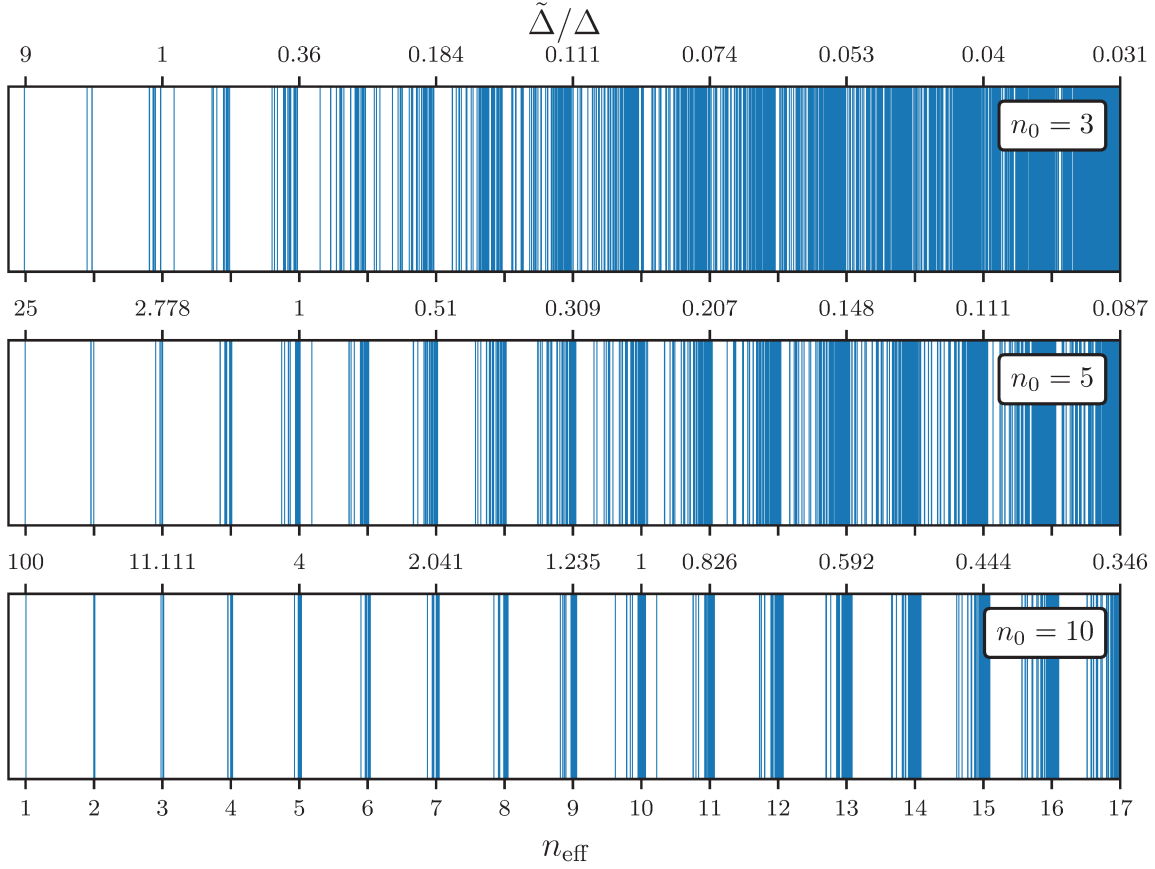


Figure 7.2.: Eigenvalue spectra for $n_0 = 3$ (top), $n_0 = 5$ (middle), and $n_0 = 10$ (bottom). Each eigenvalue contributes a delta peak to the quantum mechanical density of states (7.15). The lowest axis label for the effective quantum number n_{eff} is valid for all three parts of the figure. The three upper labels for the ratio $\tilde{\Delta}/\Delta$ of the scaled and real physical spin-orbit coupling are valid for the corresponding individual plots. This figure has already been published in Ref. [118]. The data in this plot was calculated by Moritz Schumacher [185].

function. Fourier transforming this expression will give the convolution of the delta peaks of the Fourier transformed infinite spectrum and

$$\frac{\sin\left(\Delta n_{\text{eff}} \tilde{S}_{\text{po}} / (2\hbar)\right)}{\pi \tilde{S}_{\text{po}} / \hbar} e^{-in_{\text{eff}}^0 \tilde{S}_{\text{po}} / \hbar}, \quad (7.17)$$

with the length of the finite spectrum Δn_{eff} and its center n_{eff}^0 . In addition to the main peaks this will also lead to the appearance of side peaks. To suppress these unwanted

features we use a Gaussian window function

$$w(n_{\text{eff}}) \equiv \exp\left(-\frac{(n_{\text{eff}} - n_{\text{eff}}^0)^2}{2\sigma^2}\right), \quad (7.18)$$

where we choose $\sigma \approx \Delta n_{\text{eff}}/6$.

The resulting expression for the quantum mechanical recurrence spectrum is given by

$$\begin{aligned} \hat{C}(\tilde{S}) &= \frac{1}{2\pi} \sum_{k=1}^{k_{\text{max}}} \int w(n_{\text{eff}}) \delta(n_{\text{eff}} - n_{\text{eff},k}) e^{-in_{\text{eff}}\tilde{S}/\hbar} dn_{\text{eff}} \\ &= \frac{1}{2\pi} \sum_{k=1}^{k_{\text{max}}} w(n_{\text{eff},k}) \left[\cos\left(n_{\text{eff},k}\tilde{S}/\hbar\right) - i \sin\left(n_{\text{eff},k}\tilde{S}/\hbar\right) \right], \end{aligned} \quad (7.19)$$

where k_{max} is the number of converged eigenvalues $n_{\text{eff},k}$ considered.

7.4.3 Semiclassical analysis and discussion

The quantum recurrence spectra obtained from the spectra in Fig. 7.2 are shown as solid black lines in Fig. 7.3 for the three different values of n_0 . They exhibit distinct peaks at certain values of the scaled action $\tilde{S}/(2\pi)$. The number of peaks and thus the complexity of the quantum recurrence spectra increases with decreasing values of n_0 , i.e., with decreasing energy of the excitons. The observed structures in the quantum recurrence spectra can be explained and interpreted with the help of the periodic exciton orbits. The semiclassical amplitudes of periodic orbits at positions \tilde{S}_{po} are shown in Fig. 7.3 as colored bars, labeled by the winding numbers of the corresponding orbits. The majority of the peaks in the quantum recurrence spectra can be understood in terms of classical orbits. For low actions $\tilde{S}/(2\pi)$ all peaks in the recurrence spectra can be assigned to the nearly circular orbits, which appear as central fixed point in the two symmetry planes in Fig. 6.2. These orbits move on one-dimensional tori and can therefore be labeled by an integer winding number M_1 which characterizes the repetitions of the orbits.

For increasing actions longer two-dimensional and three-dimensional orbits start to contribute to the recurrence spectra, leading to an increased density of peaks. These orbits belong to motion on two-dimensional tori in the two symmetry planes characterized by winding numbers $M_1:M_2$ or motion on fully three-dimensional tori characterized by winding numbers $M_1:M_2:M_3$. Orbits with the same winding numbers $M_1:M_2$ appear clustered together in the recurrence spectra in Fig. 7.3. Therein orbits in the mostly stable symmetry plane normal to $[100]$ exhibit the highest action as well as semiclassical amplitudes. The orbits in the unstable symmetry plane normal to $[1\bar{1}0]$ have the lowest action in the cluster and typically also the lowest semiclassical amplitude. At intermediate actions, the three-dimensional orbits can be found.

For $n_0 = 3$, only two pairs of primitive three-dimensional orbits (not counting repetitions) are found in the presented action range. Due to their small number, the values

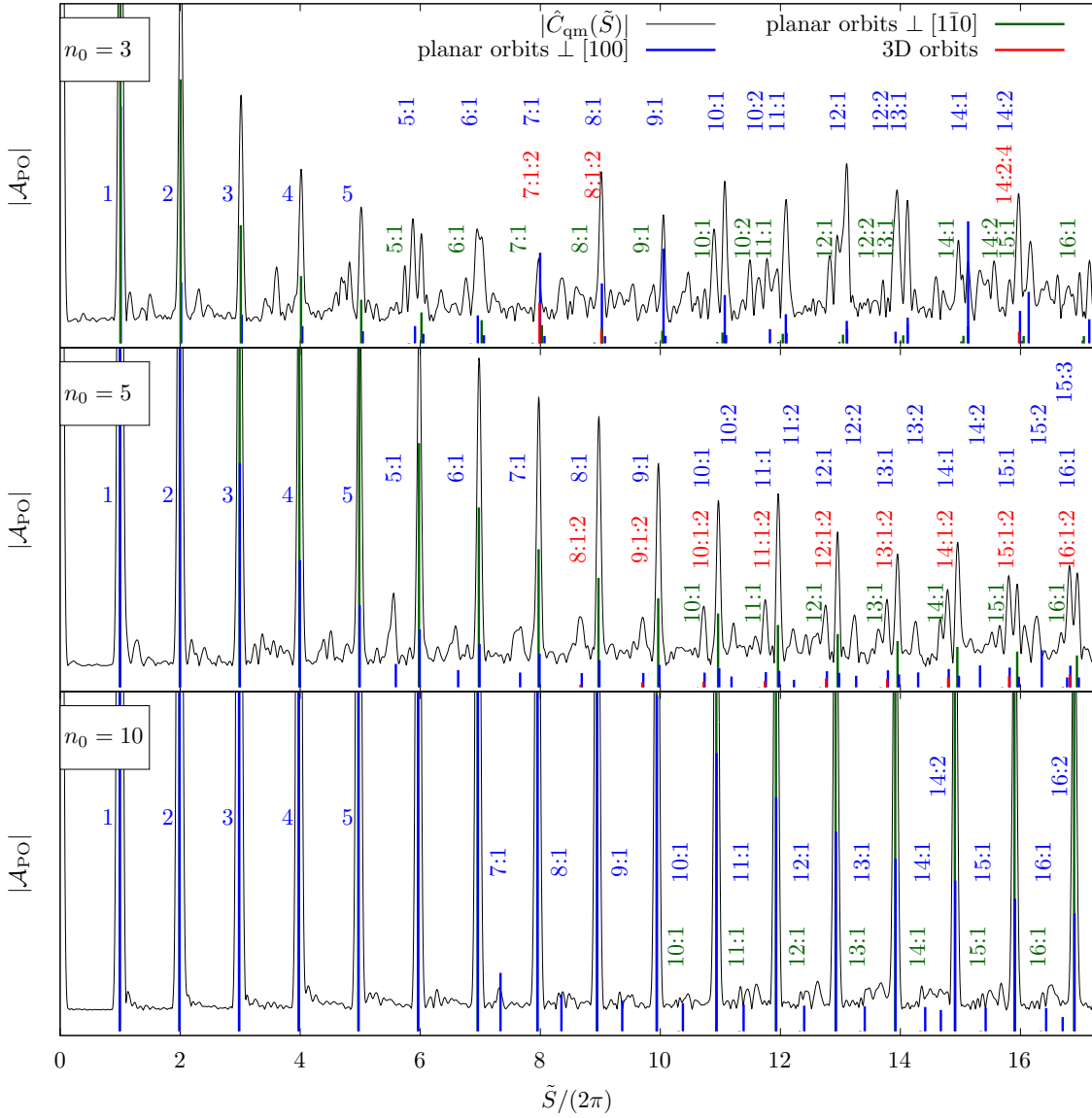


Figure 7.3.: Recurrence spectra for $n_0 = 3$ (top), $n_0 = 5$ (middle), and $n_0 = 10$ (bottom). The semiclassical amplitudes are shown as colored bars. Amplitudes for orbits in the plane normal to $[100]$ are shown in blue, amplitudes for orbits in the plane normal to $[1\bar{1}0]$ in green and amplitudes for three-dimensional orbits are shown in red. The amplitudes are labeled with the winding numbers of the corresponding orbits. The quantum recurrence spectra (black line) are shifted upwards for better visibility. This figure has already been published in Ref. [118]. Quantum mechanical results were provided by Moritz Schumacher [185]

g_E'' of the corresponding orbits in the plane normal to [100] are used for the calculation of their semiclassical amplitudes at $n_0 = 3$. This should provide a good approximation since the action of these orbits approaches their two-dimensional counterpart. Again, their $M_1:M_2$ values correspond to the region in which a change in stability properties can be observed in Fig. 6.7 (top). For $n_0 = 5$ multiple three-dimensional orbits exist in the given range, whereas for $n_0 = 10$ the three-dimensional orbits start to appear only at higher actions. For increasing n_0 the contributions of the two- and three-dimensional orbits decrease at low actions $\tilde{S}/(2\pi)$ compared to the one-dimensional orbits. On the one hand, the relative amplitudes of orbits with the same winding numbers (compared to the peaks corresponding to the nearly circular orbits) decrease for increasing n_0 . On the other hand, the range of $M_1:M_2$ values increases with n_0 , yielding more contributions for higher actions $\tilde{S}/(2\pi)$. The maximum value $(M_1/M_2)_{\max}$ is reached at the nearly circular one-dimensional orbits. Since $(M_1/M_2)_{\max}$ increases for increasing n_0 the secular motion slows down in the neighborhood of the central elliptical fixed points giving a more hydrogen-like behavior in this region. This also becomes apparent in the recurrence spectra. In the hydrogen-like case only Kepler ellipses with scaled action $\tilde{S}_{\text{po}}/(2\pi) = n$ with $n = 1, 2, \dots$ exist and therefore the peaks in the corresponding recurrence spectrum are located at the integers giving the number of repetitions of the orbits. When introducing the energy surface for the yellow series W_1 only the nearly circular orbits in the symmetry planes are periodic after one cycle providing a similar contribution as the Kepler ellipses in the hydrogen-like case. In comparison, contributions of other two-dimensional orbits in the symmetry planes and three-dimensional orbits become important for larger values of $\tilde{S}/(2\pi)$. With increasing values of n_0 this effect becomes more prominent and leads to a more hydrogen-like appearance of the recurrence spectra at $n_0 = 5$ and 10 in Fig. 7.3. This trend can also be observed at higher values of n_0 .

8

Quantum defects of the yellow exciton series in cuprous oxide

We have seen in chapter 6 that the majority of phase space for the yellow exciton series in cuprous oxide shows near-integrable behavior, where action variables can easily be constructed. In chapter 7 we were able to prove the existence of the classical exciton dynamics in the quantum spectra of the yellow series by the application of semiclassical formulas for the density of states. It now would be desirable to directly obtain the quantum states of the system similar as for the hydrogen atom. For such spherically symmetric system, the action angle variables

$$\begin{aligned}
 I_\varphi &= \frac{1}{2\pi} \oint p_\varphi d\varphi = \frac{1}{2\pi} \oint L_z d\varphi = m, \\
 I_\vartheta &= \frac{1}{2\pi} \oint p_\vartheta d\vartheta = \frac{1}{2\pi} \oint \sqrt{\mathbf{L}^2 - \frac{L_z^2}{\sin^2 \vartheta}} d\vartheta = l - |m| + \frac{1}{2}, \\
 I_r &= \frac{1}{2\pi} \oint p_r dr = n_r + \frac{1}{2},
 \end{aligned} \tag{8.1}$$

are characterized by spherical coordinates and a semiclassical quantization can be obtained using the Einstein-Brillouin-Keller-method [20–22]. The first two equations give the conservation of angular momentum L and its quantization with angular and magnetic quantum numbers l, m and the third equation gives the radial quantum number n_r . The principle quantum number n is then given by

$$n = n_r + l + 1. \tag{8.2}$$

The full Hamilton function for excitons in cuprous oxide breaks the spherical symmetry and the symmetry of the system is reduced to cubic O_h symmetry. However, we have seen in chapter 6 that the winding numbers correspond to the number of Kepler ellipses and the secular motion in the angular directions. Calculating $\frac{1}{2\pi} \oint p_\varphi d\varphi$, $\frac{1}{2\pi} \oint p_\vartheta d\vartheta$ and

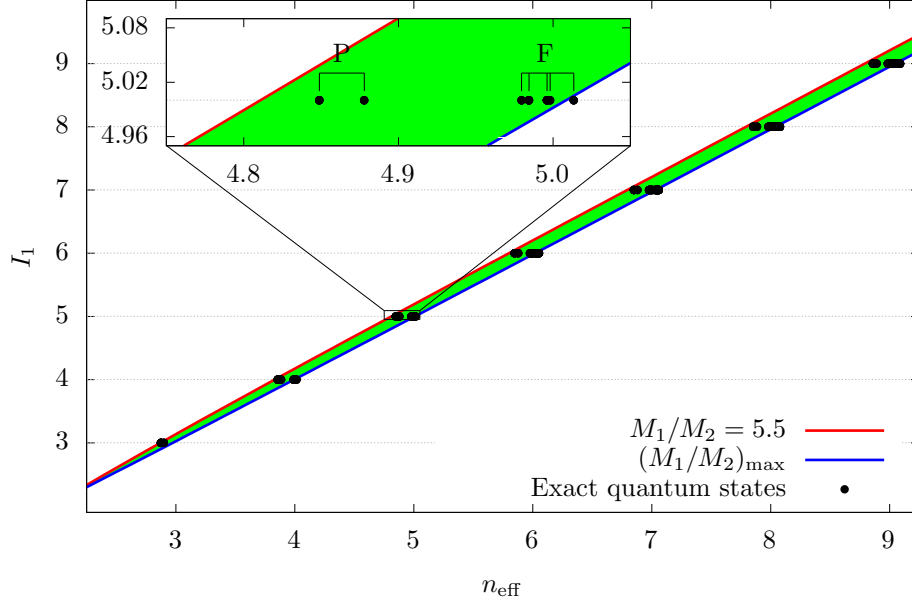


Figure 8.1.: Action variable I_1 as function of the effective quantum number n_{eff} . The green area marks the allowed region of tori with ratio M_1/M_2 of the rotation numbers between 5.5 (close to the outermost regular torus in the PSOS) and its maximum value $(M_1/M_2)_{\text{max}}$ (corresponding to the elliptical fixed point at the center of the PSOS). Semiclassically quantized exciton states belong to integer values of I_1 . The numerically exact quantum odd parity states with approximate principal quantum number n are marked by black dots. In the inset, the region around $n = 5$ is enlarged and excitons are labeled as P (for $l = 1$) or F (for $l = 3$) states [45, 60]. The black dots are perfectly located on the intersections of the lines $I_1 = n$ with the green area of classical tori, which indicates the validity of the torus quantization for excitons. This figure has already been published in Ref. [115].

$\frac{1}{2\pi} \oint p_r dr$ along a periodic orbit we find that even though the integrals no longer provide constants of motion and might differ for individual cycles in the corresponding angle, their average over the full periodic orbit is approximately equal to suitable combinations of the extracted action variables.

The quantization conditions (8.1) then allow for an assignment of quantum numbers. For the first action variable

$$I_1 \approx I_r + I_\varphi + I_\theta, \quad (8.3)$$

this is visualized in Fig. 8.1. In fact, it can be seen that the majority of quantum states lie in the semiclassical allowed energy region. However, an evaluation of the action variables in Fig. 6.9 reveals that the orbits in the regular region of the full model will not be able

to obtain the P and S states requiring $I_2 = 3/2$ and $1/2$, which are most prominent in single photon absorption and second harmonic generation experiments, respectively. For this, orbits from the chaotic region would be needed, where numerical calculations face severe difficulties.

We thus need to simplify our model further. While a hydrogen-like model is not capable of producing a splitting of the different l -states, this can be achieved using a model with spherical symmetry. The simplest model possible is obtained by setting $\nu = \delta' = \tau = 0$ in equation (4.57). In fact this was done for first theoretical calculations in cuprous oxide where a value of $\mu' = 0.47$ was found to accurately describe the experimental spectra [122]. Such a model would lead to a classical description via energy surfaces with spherical symmetry. However, this value differs drastically from the one obtained from full band structure calculations $\mu' = 0.0586$ and the value for μ obtained from band structure calculations is an order of magnitude smaller than the value found by fitting the spherical model to experimental spectra, while the cubic parts have a strong contribution [46–48].

8.1

Spherical averages of energy surfaces in cuprous oxide

To obtain a spherical model from the more accurate, full model obtained from band structure calculations, we perform a spherical average

$$\widetilde{W}_y(p) = \frac{1}{4\pi} \int_0^{2\pi} \int_0^\pi W_y(p, \varphi, \vartheta) d\Omega \quad (8.4)$$

using an efficient spherical design [123]. From the quantization condition for angular momentum $L = l + \frac{1}{2}$ we can estimate that the maximum momentum for a given l in a Rydberg state is given by

$$p_{\max} = \frac{4}{2l + 1} \quad (8.5)$$

reaching a maximum value of 4 for S states. In figure 8.2 the spherical average $\widetilde{W}_y(p)$ as well as the energy surfaces obtained from a spherical model with $\mu' = 0.47$ and $\mu' = 0.0586$ are shown.

It becomes obvious that simply ignoring ν, δ' and τ in the model obtained from band structure calculations is not sufficient to describe the spherical average correctly. To obtain a spherical model from the full model we fit the spherical model to the spherical average obtaining a value of $\mu' = 0.51$. For the fit we assume the probability of $|\psi|^2 \sim 1/|p|$ to find the particle at momentum p as weight, according to a WKB-like wave function (3.6). This value is in good agreement with the value obtained by the Dortmund group when fitting the spherical model to experimental spectra [122], considering that

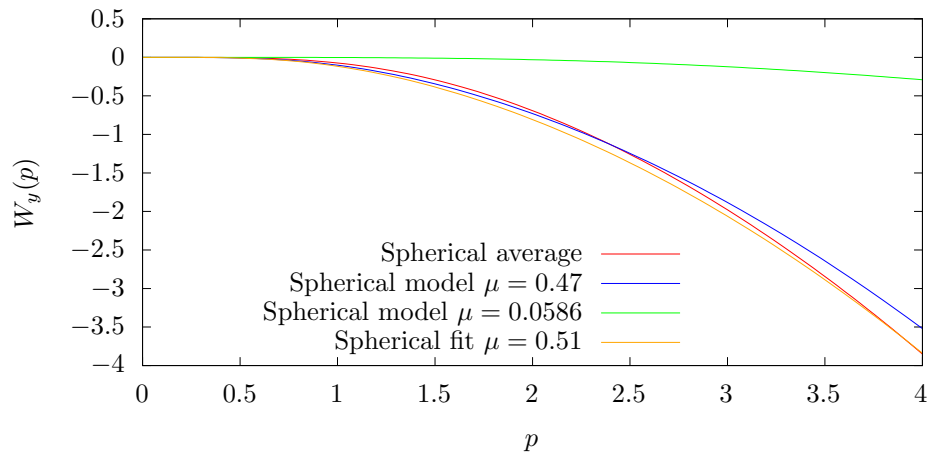


Figure 8.2.: Comparison of the spherical average $\widetilde{W}_y(p)$ with spherical models using $\mu' = 0.47$ and $\mu' = 0.0586$. A fit of the spherical model to the spherical model obtains $\mu' = 0.51$.

slightly different material parameter and a semiclassical estimation scheme were used here.

8.2

EBK-quantization for excitons in cuprous oxide

For our semiclassical calculations we thus continue with the literature value $\mu' = 0.47$. For a given angular momentum quantum number l the corresponding m -manifold is degenerate due to the spherical symmetry of the problem. By fixing the angular momentum l and numerically integrating the equation for I_r (8.1) the energy eigenvalues $E_{n,l}$ are obtained which take the form

$$E_{n,l} = E_g + \frac{E_{\text{Ryd}}}{n_{\text{eff}}^2(n,l)}, \quad (8.6)$$

with the excitonic Rydberg energy E_{Ryd} . The quantum defects are then given by

$$\delta_{n,l} = n - n_{\text{eff}}(n,l). \quad (8.7)$$

The values of the quantum defects for S, P, D and F states are shown in figure 8.3 (left) up to $n = 25$.

It can be seen that the quantum defects are positive and increase and saturate with increasing n , while for increasing l the quantum defects decrease as expected. While the

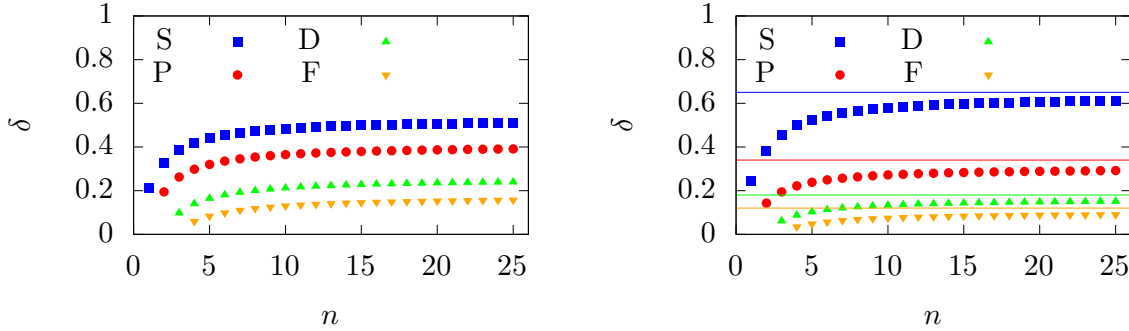


Figure 8.3.: Left: Quantum defects $\delta_{n,l}$ for S, P, D and F states up to principle quantum number $n = 25$ for $\mu' = 0.47$. Right: Quantum defects using spherical model with μ' optimized for different l series. Experimental values in the limit of large n from Ref. [66] are shown as solid line in the corresponding color.

quantum defects obtained within the semiclassical picture are accurate enough to reproduce the experimental findings by Uihlein et al. from 1981 [122] up to meV precision, a comparison with more recent quantum mechanical and experimental results [47, 48] unveils that the quantum defects are overestimated in the simple spherical model for higher angular momentum quantum numbers. A possible reason is that the fit to the spherical average was performed up to the maximum allowed value of the momentum in a hydrogen-like S state. As can be seen from equation (8.5) this value decreases for increasing l . This suggests that the fitting procedure should be adapted to the corresponding momentum range. In fact this leads to different values for μ' . We obtain $\mu'_S = 0.51$, $\mu'_P = 0.41$, $\mu'_D = 0.38$ and $\mu'_F = 0.36$. For increasing l the spherical corrections become less and less important leading to a more dominant hydrogen-like behavior. Repeating the quantization procedure for the different models provides the quantum defects shown in figure 8.3 (right).

The quantum defects for the higher angular momentum space are now shifted downwards, providing a good agreement of semiclassical and experimental values where the quantum defects for large n saturate to $\delta_S = 0.65$, $\delta_P = 0.34$, $\delta_D = 0.18$ and $\delta_F = 0.12$ [66], as well as for semiclassical and quantum mechanical values [47, 48]. In fact the semiclassical results are closer to the quantum mechanical results using the full model than some values obtained by perturbative approaches [66].

9

Chaos in the green exciton series

After discussing the classical dynamics and semiclassical quantization of the yellow exciton series, we now want to focus on the green exciton series where we compare the results to the yellow series. At the Γ point the green series is shifted by Δ , meaning that the scaling (6.2) has to be slightly modified for the green series

$$n_{\text{eff}} = \sqrt{E_{\text{Ryd}}/(E_{\text{g}} + \Delta - E)}. \quad (9.1)$$

The classical dynamics can then again be calculated by choosing a fixed value $n_0 = n_{\text{eff}}$. The majority of this paper has been submitted for publication [119].

9.1 Dynamics at $n_0 = 5$

In figure 9.1 PSOS for $n_0 = 5$ for both symmetry planes are presented for the yellow series and the green series with heavy and light hole. For the dynamics in the plane normal to $[100]$ one can observe a central elliptical fixed point surrounded by regular tori. For the yellow exciton series the majority of phase space exhibits regular structures, with only a small chaotic region in the outermost part of the PSOS, while for the green series the chaotic regions are larger and the tori in the outermost part of the PSOS appear stronger deformed than in the case for the yellow series. The orbit for the central fixed point appears almost circular for the yellow series in the plane normal to $[100]$ as well as in the plane normal to $[1\bar{1}0]$ resembling the circular orbit one would obtain for similar starting conditions in the hydrogen-like model. By contrast, the central fixed points for the green series show stronger deviations from the hydrogen-like behavior, instead one can observe the C_{4v} symmetry for the orbit in the plane normal to $[100]$ and the C_{2v} symmetry for the orbit in the plane normal to $[1\bar{1}0]$ respectively. Concerning the phase space in the symmetry plane normal to $[1\bar{1}0]$ the emerging structures for the

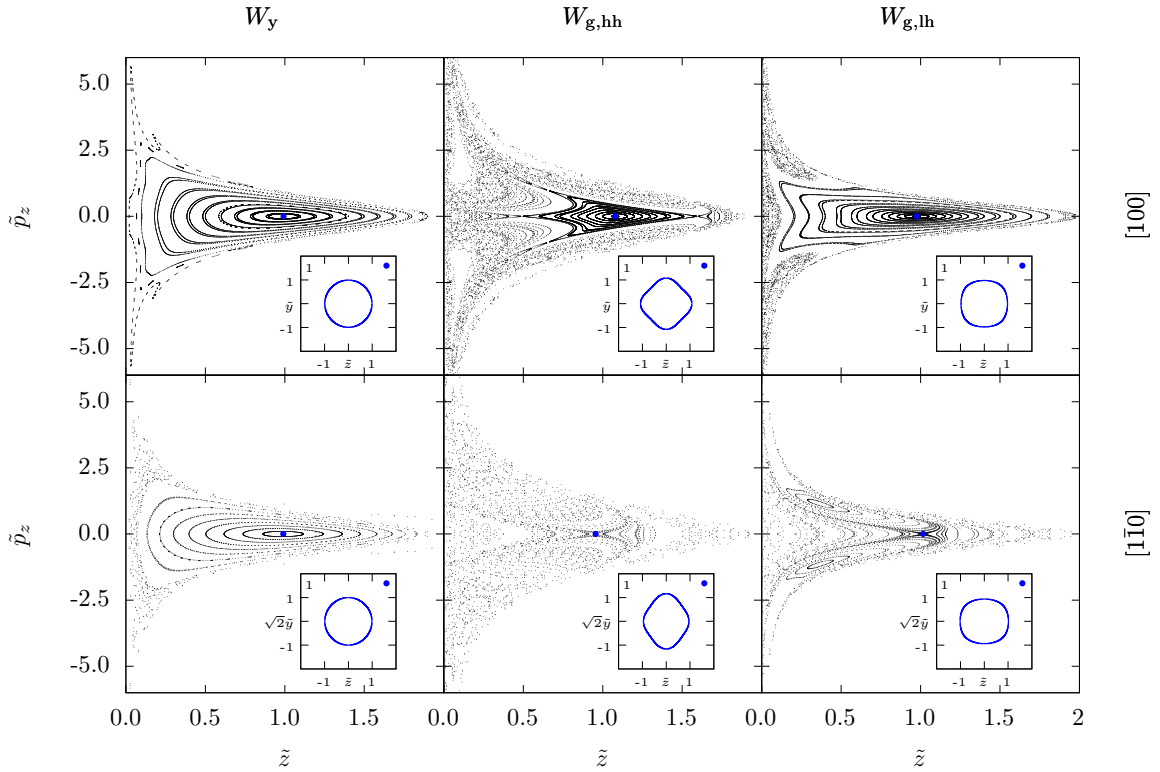


Figure 9.1.: PSOS at $n_0 = 5$ for the yellow exciton series (left), the green exciton series with heavy holes (middle), and the green exciton series with light holes (right) for the plane normal to [100] (top), and the plane normal to [110] (bottom). Insets show the orbit for the central fixed point. The units are chosen such that $\hbar = e = m_0/\gamma'_1 = 1/(4\pi\epsilon_0\epsilon) = 1$. Coordinates and momenta are scaled according to $\mathbf{r} = n_0^2\tilde{\mathbf{r}}$, $\mathbf{p} = n_0^{-1}\tilde{\mathbf{p}}$. This figure has already been presented in Ref. [119].

yellow series look fairly similar to what can be observed in the plane normal to [100] with a central elliptical fixed point surrounded by a large region with regular tori and a small chaotic region in the outermost part of the PSOS. For the green series the structures, however, differ entirely. Here, the central periodic orbit becomes a hyperbolic fixed point surrounded by a stochastic region in phase space. For the green series with heavy holes the remaining part of the phase appears entirely chaotic while for the green series with light holes some regular structures persists surrounding two elliptical fixed points in addition to the central hyperbolic fixed point.

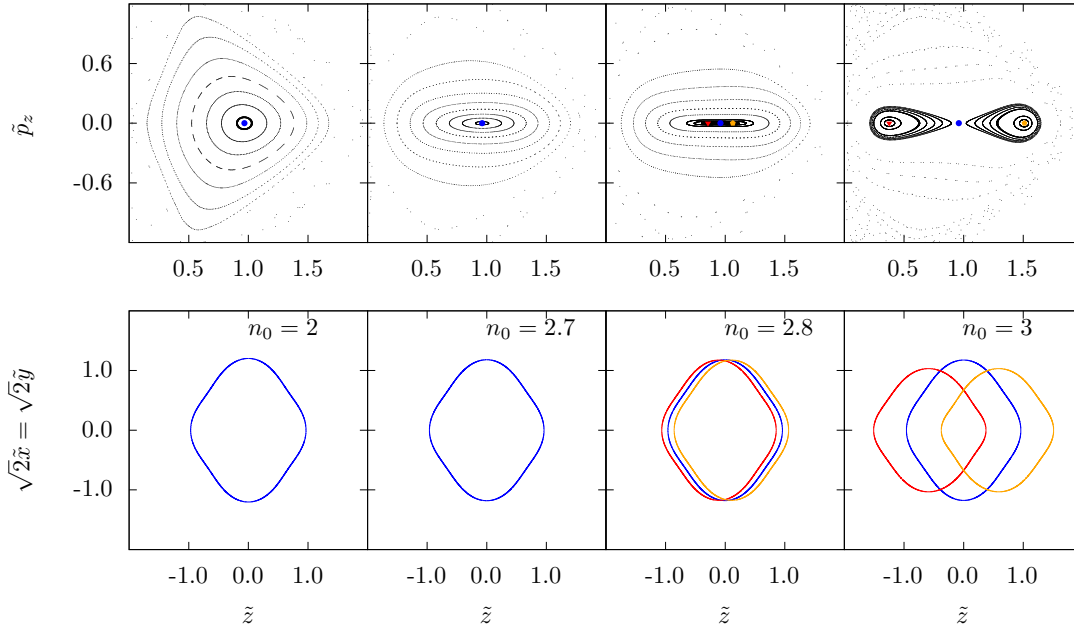


Figure 9.2.: PSOS for the plane normal to $[1\bar{1}0]$ for the green series with heavy holes (top) and orbits corresponding to the observable fixed points (bottom). The energy ranges from values corresponding to effective principle quantum numbers $n_0 = 2$, $n_0 = 2.7$, $n_0 = 2.8$ to $n_0 = 3$ from top to bottom. The units are chosen such that $\hbar = e = m_0/\gamma'_1 = 1/(4\pi\epsilon_0\epsilon) = 1$. Coordinates and momenta are scaled according to $\mathbf{r} = n_0^2\tilde{\mathbf{r}}$, $\mathbf{p} = n_0^{-1}\tilde{\mathbf{p}}$. This figure has already been presented in Ref. [119].

9.2

Bifurcations of the central green exciton orbit

For the yellow exciton series the phase space in the two distinct symmetry planes behave similar when varying the energy (see Chapter 6). For the green series this holds true for the plane normal to $[100]$, a closer investigation of the energy dependence of the green series reveals however, that the central orbit in the plane normal to $[1\bar{1}0]$ undergoes a bifurcation going from an elliptical fixed point, splitting into a hyperbolic fixed point and two elliptical orbits. We present this process for the green series with heavy holes, the investigation of the light hole yields similar results. The PSOS and the shape of the central orbit at various values of n_0 in the range from $n_0 = 2$ to 3 are presented in figure 9.2. For energies corresponding to principle quantum number up to $n_0 = 2.7$

the PSOS reveals a stable elliptical fixed point, at $n_0 = 2.8$ the structure has changed now showing an unstable fixed point at the center of the PSOS as well as two separated stable elliptical fixed points which move outward with increasing energy. The orbits corresponding to the fixed points are shown on the bottom right of their respective PSOS. Up to $n_0 = 2.7$ there is only one orbit with the full C_{2v} symmetry of the $[1\bar{1}0]$ plane. This still holds for the unstable orbit of the central fixed point, however the two orbits corresponding to the elliptical fixed point no longer exhibit the full symmetry of the plane. Instead, they can be transformed into each other using symmetry operations of the C_{2v} group. We can observe that the central fixed point undergoes a pitchfork-bifurcation, changing its stability in the plane from stable to unstable. This can also be viewed as a period doubling. Projecting the central orbit to the fundamental region, the orbit returns to the fixed point after half a revolution, while the stable orbits alternate between the two fixed points. For the green series with light holes a similar behavior can be observed. In contrast to the series with heavy holes the split off stable fixed points do not stay on the $p_z = 0$ axis instead they move along the $p_x = p_y = 0$ axis. The corresponding fixed points can still be seen in figure 9.1. For higher values the elliptical fixed points move outward towards the chaotic region showing a clear separation for example for $n_0 = 3$ in figure 9.2 for the green series with heavy holes. Increasing the energy further the elliptical fixed points formed in the pitchfork bifurcation move further towards the chaotic region. There they finally collide with a hyperbolic fixed point and disappear in a saddle-node bifurcation. This results in a completely chaotic phase space, as can be seen for the green series with heavy holes at $n_0 = 5$ in figure 9.1.

9.3 Lyapunov exponents

The stability of the central fixed points can also be analyzed quantitatively using Lyapunov exponents. In addition to the dynamics in the plane this also enables us to gain insights concerning the stability of the orbit against perturbations out of the plane. For the plane normal to $[100]$ the central fixed points of all series are stable both against perturbations in the plane, resulting in the elliptical shape of the fixed point in figure 9.1, and for perturbations out of the symmetry plane. Thus, all Lyapunov exponents are equal to zero in this case. For the plane normal to $[1\bar{1}0]$ the situation becomes more complex. The Lyapunov exponents for the orbits corresponding to the central fixed points in the plane normal to $[1\bar{1}0]$ are shown in figure 9.3. It becomes apparent, that the Lyapunov exponent corresponding to perturbations of the orbit out of the symmetry plane Λ_{\perp} shows unstable behavior for all energies, i.e., the Lyapunov exponents are positive and approach zero for larger energies. In this case the dominant contribution from the band structure corrections is due to the spin-orbit coupling, which then results in a more hydrogen-like behavior of the three series. In the hydrogen-like case the central orbit would be a circle with all Lyapunov exponents equaling zero, since this

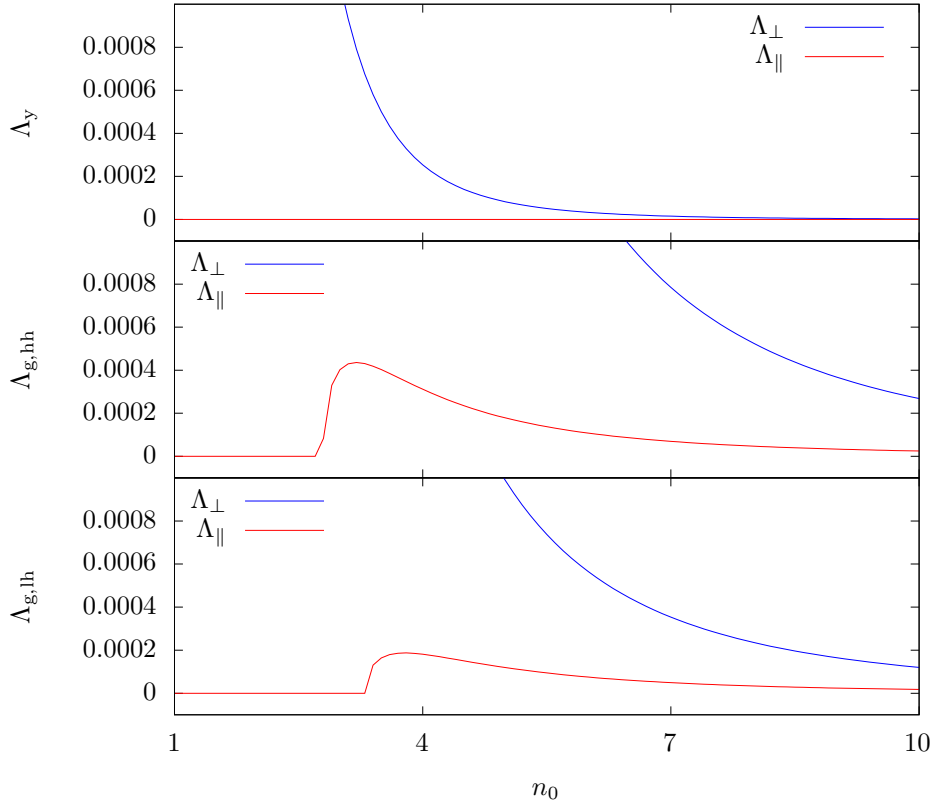


Figure 9.3.: Lyapunov exponents for the orbits corresponding to the central fixed points in the plane normal to $[1\bar{1}0]$ for the yellow series (left), the green series with heavy holes (middle), and the green series with light holes (right). The energy ranges from values corresponding to effective principle quantum numbers $n_0 = 1$ to $n_0 = 10$. This figure has already been presented in Ref. [119].

case is completely regular. For the yellow series the central orbit bares resemblance to a circle, and also the Lyapunov exponent corresponding to perturbations in the symmetry plane Λ_{\parallel} shows stable behavior for all given energies. By contrast, the central orbits corresponding to the green series show stronger deviations from the circular shape. In addition, their stability properties in the plane differ from the hydrogen-like behavior. While the Lyapunov exponents are equal to zero for low energies a change in stability can be observed for both green series. For the series with heavy holes this happens between $n_0 = 2.7$ and $n_0 = 2.8$, matching the transition observed in figure 9.2. For the series with light holes this change can be observed between $n_0 = 3.3$ and $n_0 = 3.4$. After changing their stability the Lyapunov exponents start decreasing again and approach $\Lambda_{\perp} = 0$ at high energies.

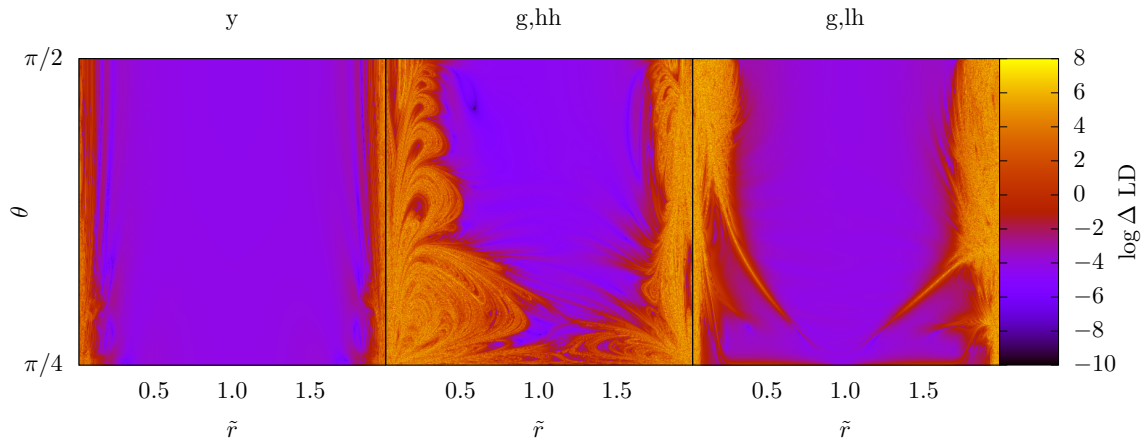


Figure 9.4.: ΔLD at $n_0 = 5$ for the yellow exciton series (top), the green exciton series with heavy holes (middle), and the green exciton series with light holes (bottom). The time corresponds to 10 cycles of a Kepler ellipse in the hydrogen-like case. At the upper boarder the plane normal to $[001]$ and at the lower boarder the plane normal to $[\bar{1}01]$ are located. Strong fluctuations in the arc length are characterized by large values of ΔLD and indicate a classically chaotic exciton dynamics. The chaotic regions are more pronounced for the green than for the yellow excitons. This figure has already been presented in Ref. [119].

9.4 Analysis of the full phase space with LDs

In cuprous oxide periodic three-dimensional orbits do exist when moving the initial conditions out of the symmetry planes. The two-dimensional periodic orbits exhibit a turning point in the radial direction on one of the symmetry axis ($[100]$, $[1\bar{1}0]$ or equivalent). The projection of the three-dimensional periodic orbits on the symmetry plane exhibit the same behavior with either the velocity exhibiting an angle to the plane or the velocity parallel to the plane and the starting position rotated above the symmetry axis. This allows for the characterization of the three-dimensional periodic orbits by only the initial radius, i.e., the r coordinate and one of these angles. Changing these parameters, however, in general results in non-periodic three-dimensional orbits. We use this property to examine the three-dimensional motion for the three distinct exciton series. To examine the three-dimensional motion we initialize the orbit at $\varphi = 0$ in a turning point for the r and ϑ direction exemplarily. We thus can visualize the three-dimensional dynamics using the ΔLD indicator (2.29) over r and ϑ calculating the

LD on a 500×500 mesh and using a finite difference quotient for the second derivatives as in reference [13]. The results are presented in Fig. 9.4. Stochastic regions with large values of ΔLD indicate chaotic behavior, whereas smaller values indicate regions with regular behavior.

For the yellow exciton series chaotic regions only exist at the lowest and highest r values, with large regular regions in between. For the two green exciton series the situation is similar close to the plane normal to $[001]$ but the area of the chaotic regions increases when the plane normal to $[\bar{1}01]$ is approached. Here, the ΔLD indicator exhibits a completely chaotic phase space for the green series with heavy holes and a small regular region remaining for the green series with light holes at $n_0 = 5$ matching the appearance of the PSOS in Fig. 9.1. Figures for the ΔLD indicator, where the starting conditions are chosen to match the other periodic three-dimensional orbits, result in qualitatively similar pictures. The same holds true when varying n_0 and T , the emerging phase space structures are qualitatively similar to $n_0 = 5$ and $T = 20\pi n_0^3$. While for the green series the share of the phase space which exhibits stochastic regions stays roughly the same, for the yellow series, however, the stochastic regions shrink with increasing n_0 resulting in a more regular phase space.

10

Conclusion and outlook

In this thesis we developed the foundations for a semiclassical description of excitons in cuprous oxide. In the theoretical description additional spin degrees of freedom appear compared to a simple hydrogen-like model to accurately model the complex valence band structure. The full Hamiltonian describes three distinct exciton series, a yellow series, where holes are located in a split-off valence band, and a green series with light and heavy holes, where the corresponding valence bands are shifted downwards by the spin-orbit splitting Δ at the Γ point compared to the split-off band. A treatment of the quasispin I and hole spin S_h through an adiabatic approach leads to a description via energy surfaces in momentum space that only depend on the momentum $W_k(\mathbf{p})$. In chapter 5 we derived analytical expressions for these energy surfaces for the case without external fields. The three distinct energy surfaces $W_k(\mathbf{p})$ can be directly assigned to the different exciton series.

Classical exciton orbits can be calculated by choosing an energy surface and integrating Hamilton's equations of motion. In chapter 6 we investigated the classical dynamics of the yellow exciton series. Here we found a largely regular phase space when investigating the PSOS with regular tori surrounding a fixed point belonging to a nearly circular orbit. The classical orbits observed resemble classical Kepler ellipses experiencing a secular motion. In addition to two-dimensional orbits in the symmetry planes, fully three-dimensional orbits exist due to the band structure corrections which reduce the rotational $SO(4)$ symmetry of the hydrogen-like system to cubic O_h symmetry. Because of this symmetry reduction, the system is no longer integrable and small chaotic regions can be observed in phase space. In accordance with the Poincaré–Birkhoff theorem the rational tori break up leaving behind pairs of stable and unstable periodic partner orbits for the dynamics in the symmetry planes. For three-dimensional motion, four partner orbits can be found. Since the periodic orbits are the remnants of the resonant tori, they can be used to reconstruct action angle variables. The stability properties of the system can be quantified by computing the eigenvalues of the stability matrix.

To demonstrate the existence of the classical exciton dynamics we used semiclassical

formulas for the density of states in chapter 7. In these, every periodic orbit contributes a sinusoidal fluctuation defined by the action of the orbit. The amplitudes are given through parameters of the periodic orbit as well. The amplitudes become particularly simple for systems exhibiting a scaling property. Here, the density of states is given by a Fourier series in the scaled action with constant amplitudes. Performing a Fourier transformation from the domain of the scaled parameter to scaled action domain, the resulting recurrence spectra provide δ peaks at values of the scaled action of individual orbits. We recover such a scaling property for excitons in cuprous oxide by applying a scaling technique to the spin-orbit coupling. This allows us to compute quantum mechanical recurrence spectra, where all major peaks can be assigned to a corresponding classical orbit.

In chapter 8 we calculated the quantum defects for the yellow exciton series in cuprous oxide. For this we developed a spherically symmetric model by taking the spherical average of the model with the full cubic symmetry. Fitting the spherically symmetric model with $\nu = \delta' = \tau = 0$ to the obtained spherical average we obtain a material parameter $\mu' = 0.51$ characterizing the spherical symmetry, which is in good agreement with earlier works, that obtained $\mu' = 0.47$ by fitting theoretical spectra to their experimental counterpart [122]. Using the literature value we computed the quantum defects in cuprous oxide via the EBK-method. The agreement with results obtained by quantum calculations with the full model [47] is already good for S states while the defects for higher l states are overestimated. This is due to the momentum range used when fitting the spherically symmetric model to the spherical average which was chosen to allow for all classically allowed values for S states. For higher l states this range becomes smaller leading to different parameters when fitting the model in the corresponding range. We obtain $\mu'_S = 0.51$, $\mu'_P = 0.41$, $\mu'_D = 0.38$ and $\mu'_F = 0.36$ resulting in a good agreement between semiclassical theory and fully quantum mechanical models.

Finally, we investigated the classical dynamics of the green exciton series in chapter 9. While the yellow exciton series shows largely regular behavior, we were able to uncover large chaotic phase space regions by using PSOS and LDs. For the central fixed point in the plane normal to $[1\bar{1}0]$ we observed a bifurcation, finally resulting in completely chaotic phase space regions. Excitons in cuprous oxide thus provide an example of a two-particle system with classical chaos, even without the introduction of external fields. The chaotic dynamics arises due to the complex valence band structure of the system.

In principle one could now also use semiclassical quantization methods to further investigate the green exciton series. Here, it would be interesting to study the impact of the observed bifurcation on the quantum spectra by analyzing the quantum recurrence spectra of the green series similar to the yellow exciton series (see chapter 7), where peaks in the quantum recurrence spectra occur at the action of a corresponding orbit. After the bifurcation takes place one should be able to identify a splitting of the corresponding peak in the quantum recurrence spectrum.

The classically chaotic dynamics of the green series should manifest in the level spacing statistics, leading to a repulsion of adjacent levels [126, 131, 186]. While the existence

of quantum chaos has been demonstrated for magnetoexcitons in cuprous oxide which break all antiunitary symmetries [59, 61, 64], it would be interesting to see whether quantum mechanical calculations for the green exciton series could uncover signatures of chaos even without external fields.

A semiclassical quantization within the adiabatic approach would lead to bound green states. In reality, due to the coupling to the yellow continuum, the green exciton states become resonances with finite lifetimes [53]. In semiclassical theory the decay of these states is related to a surface hopping between the green and yellow energy surfaces. This surface hopping may be modeled within the adiabatic approach when additional non-adiabatic coupling terms are considered, similar as for the surface hopping on molecules within the Born-Oppenheimer approximation [187–191]. In cuprous oxide this would allow the exciton to jump between green and yellow energy surfaces, until it reaches the unbound region on the yellow energy surface where it dissipates. This extension of the adiabatic approach would allow for a semiclassical interpretation of the resonant states in cuprous oxide. A treatment within a more simple one-dimensional model was already capable of obtaining values in the correct order of magnitude compared to quantum mechanical calculations [192].

Future work could expand the semiclassical treatment of the yellow exciton series. We observed a mixed regular-chaotic phase space, where the dynamics determining the low angular momentum states are located, while higher angular momentum states correspond to nearly integrable regions. For the higher lying angular momentum states one could perform a torus quantization to obtain the quantum states including the fine-structure splitting. For this a large set of three-dimensional orbits would be necessary, to obtain a continuous area providing the action variables I_i for a given set of winding numbers M_i . In principle one could also search for more periodic orbits in the chaotic region and use the methods presented in Refs. [35, 180] to reconstruct the action angle variables. The chaotic region is however difficult to handle. On the one hand there is the Coulomb singularity for $r \rightarrow 0$, which can be lifted using an appropriate coordinate transformation [193, 194] on the other hand even after the regularization the energy surfaces $W_k(\mathbf{p})$ will exhibit a discontinuity for $r \rightarrow 0$ when examining the full model with cubic symmetry. In both areas one could use machine learning algorithms like Gaussian process regression [195] to aid in the search for periodic orbits and the construction of action variables.

The semiclassical methods developed here make it possible to investigate regimes where full quantum mechanical calculations are no longer feasible. An example would be the magnetoexciton for which only the lower-lying quantum states can be calculated in the quantum mechanical framework [58]. However, Rydberg systems are known to display interesting new phenomena. Coulomb and Lorentz forces become comparable near the ionization threshold including quasi-Landau resonances [182, 196–203]. Semiclassical absorption spectra can be calculated using the theory developed by Du and Delos [204, 205]. Here closed orbits starting at $r = 0$ are needed. Previous approaches explaining the quasi-Landau in this semiclassical framework were unsuccessful [114].

This was partially due to convergence issues of stability properties in the full cubic symmetric model. A problem with this is that the band structure contributions become large in the region $r \rightarrow 0$ where dynamics become chaotic even without external fields. One way to omit this would be to use in a first approximation the spherically symmetric energy surfaces, similar to our calculations of quantum defects in this thesis. Here, the discontinuity of the energy surfaces at $r \rightarrow 0$ does not take place allowing for a much simpler numerical treatment.

Another interesting topic would be to investigate excitons in quantum wells [101, 109, 206]. Here the Coulomb potential needs to be corrected accounting for the image charges due to the boundary surfaces [207] leading to the Rytova-Keldysh potential for thin quantum wells [208, 209]. Due to the symmetry reduction fully quantum mechanical approaches are difficult when including the band structure of cuprous oxide into calculations and thus far the theoretical investigations are based on hydrogen-like models [101, 109]. It would be interesting to investigate the influence of the confining potential on the classical dynamics. With the adiabatic approach one could also include energy surfaces into the semiclassical calculations for excitons in quantum wells, which would allow for the discussion of effects due to the complicated band structure.

Furthermore, the classical model intrinsically exhibits a dipole moment which could provide a starting point to describe and better understand interactions between Rydberg excitons such as scattering processes between Rydberg excitons [210, 211], the Rydberg blockade [86], and the possible existence of an exciton molecule [212] in analogy to Rydberg molecules [213, 214].

A

Material parameters

The material parameters of cuprous oxide used in this thesis are summarized in the following table A.1.

Table A.1.: Material parameters of Cu_2O used in this thesis.

band-gap energy	E_g	2.17208eV	[43]
electron mass	m_e	$0.99m_0$	[159]
hole mass	m_h	$0.58m_0$	[159]
dielectric constant	ϵ	7.5	[160]
spin-orbit coupling	Δ	0.131eV	[48]
Luttinger parameters	γ_1	1.76	[48]
	γ_2	0.7532	[48]
	γ_3	-0.3668	[48]
	η_1	-0.02	[48]
	η_2	-0.00367	[48]
	η_3	-0.03367	[48]

B

Exciton-Hartree units

We follow [114, 175, 215] in introducing exciton-Hartree units obtained by setting

$$e = \frac{m_0}{\gamma'_1} = \hbar = \frac{1}{4\pi\epsilon\epsilon_0} = 1. \quad (\text{B.1})$$

In the following table B.1 we give Hartree units for the exciton ($\gamma'_1 = 2.77, \epsilon = 7.5$) and for hydrogen ($\gamma'_1 = 1, \epsilon = 1$) as well as their conversion to SI units.

Table B.1.: Conversion rates for exciton-Hartree units and atomic Hartree units to SI units.

quantity		unit	SI (exciton)	SI (hydrogen)
charge	q	e	$1.602 \times 10^{-19}\text{C}$	$1.602 \times 10^{-19}\text{C}$
mass	m	$m_0\gamma'_1{}^{-1}$	$3.288 \times 10^{-31}\text{kg}$	$9.109 \times 10^{-31}\text{kg}$
ang. momentum	L	\hbar	$1.055 \times 10^{-34}\text{Js}$	$1.055 \times 10^{-34}\text{Js}$
length	r	$a_{\text{exc}} = \epsilon\gamma'_1 4\pi\epsilon_0 \hbar^2 m_0^{-1} e^{-2}$	$1.099 \times 10^{-9}\text{m}$	$0.529 \times 10^{-10}\text{m}$
momentum	p	$\hbar a_{\text{exc}}^{-1}$	$9.593 \times 10^{-26}\text{kg m s}^{-1}$	$1.993 \times 10^{-24}\text{kg m s}^{-1}$
energy	E	$E_{\text{h}} = \hbar^2 \gamma'_1 a_{\text{exc}}^{-2} m_0^{-1}$	$1.399 \times 10^{-20}\text{J}$	$4.360 \times 10^{-18}\text{J}$
time	t	$\hbar E_{\text{h}}^{-1}$	$3.769 \times 10^{-15}\text{s}$	$2.419 \times 10^{-17}\text{s}$
mag. flux density	B	$\hbar e^{-1} a_{\text{exc}}^{-2}$	$5.446 \times 10^2\text{T}$	$2.350 \times 10^5\text{T}$
el. field strength	F	$E_{\text{h}} e^{-1} a_{\text{exc}}^{-1}$	$1.589 \times 10^8\text{Vm}^{-1}$	$5.142 \times 10^{11}\text{Vm}^{-1}$

C

Matrix representation of angular momentum operators

To arrive at a matrix representation for the band structure Hamiltonian $H_{\text{band}}(\mathbf{p}, \mathbf{I}, \mathbf{S}_h)$ given by Eq. (4.49) we introduce ladder operators for quasispin I

$$\mathbf{I}_{\pm} = \mathbf{I}_x \pm i\mathbf{I}_y, \quad (\text{C.1})$$

and hole spin S_h

$$\mathbf{S}_{h\pm} = \mathbf{S}_{hx} \pm i\mathbf{S}_{hy}. \quad (\text{C.2})$$

These operators act on a given state according to

$$\mathbf{I}_{\pm} |I, m_I\rangle = \hbar\sqrt{I(I+1) - m_I(m_I \pm 1)} |I, m_I \pm 1\rangle, \quad (\text{C.3})$$

and

$$\mathbf{S}_{h\pm} |S_h, m_{S_h}\rangle = \hbar\sqrt{S_h(S_h+1) - m_{S_h}(m_{S_h} \pm 1)} |S_h, m_{S_h} \pm 1\rangle. \quad (\text{C.4})$$

Note that at $I = 1$ and S_h the root takes the value $\sqrt{2}$ for all allowed values of m_I and m_{S_h} . By inverting Eq. (C.1) and Eq. (C.2) we can find the following matrix elements for states

$$|\Phi\rangle = \left| 1, m_I, \frac{1}{2}, m_{S_h} \right\rangle. \quad (\text{C.5})$$

To simplify the presentation we make the convention that $\tilde{\delta}_{i,i} = 1$ only for values $|i| \leq 1$ and zero otherwise,

$$\begin{aligned} \langle \Phi' | \mathbf{I}_1 \mathbf{S}_{h1} | \Phi \rangle = \frac{\hbar^2}{2} & \left(\tilde{\delta}_{m'_I, m_I - 1} \tilde{\delta}_{m'_{S_h}, m_{S_h} - 1} + \tilde{\delta}_{m'_I, m_I + 1} \tilde{\delta}_{m'_{S_h}, m_{S_h} - 1} \right. \\ & \left. + \tilde{\delta}_{m'_I, m_I - 1} \tilde{\delta}_{m'_{S_h}, m_{S_h} + 1} + \tilde{\delta}_{m'_I, m_I + 1} \tilde{\delta}_{m'_{S_h}, m_{S_h} + 1} \right), \end{aligned} \quad (\text{C.6})$$

C. Matrix representation of angular momentum operators

$$\langle \Phi' | \mathbf{I}_2 \mathbf{S}_{h2} | \Phi \rangle = \frac{\hbar^2}{2} \left(-\tilde{\delta}_{m'_I, m_I-1} \tilde{\delta}_{m'_{S_h}, m_{S_h}-1} + \tilde{\delta}_{m'_I, m_I+1} \tilde{\delta}_{m'_{S_h}, m_{S_h}-1} \right. \\ \left. + \tilde{\delta}_{m'_I, m_I-1} \tilde{\delta}_{m'_{S_h}, m_{S_h}+1} - \tilde{\delta}_{m'_I, m_I+1} \tilde{\delta}_{m'_{S_h}, m_{S_h}+1} \right), \quad (\text{C.7})$$

$$\langle \Phi' | \mathbf{I}_3 \mathbf{S}_{h3} | \Phi \rangle = \hbar^2 m_I m_{S_h} \tilde{\delta}_{m'_I, m_I} \tilde{\delta}_{m'_{S_h}, m_{S_h}}, \quad (\text{C.8})$$

$$\langle \Phi' | \mathbf{I}_1^2 | \Phi \rangle = \frac{\hbar^2}{2} \left(\tilde{\delta}_{m'_I, m_I-2} \tilde{\delta}_{m'_{S_h}, m_{S_h}} + \tilde{\delta}_{m'_I, m_I} \tilde{\delta}_{m'_{S_h}, m_{S_h}} \right. \\ \left. + \tilde{\delta}_{m_I, 0} \tilde{\delta}_{m'_I, 0} \tilde{\delta}_{m'_{S_h}, m_{S_h}} + \tilde{\delta}_{m'_I, m_I+2} \tilde{\delta}_{m'_{S_h}, m_{S_h}} \right), \quad (\text{C.9})$$

$$\langle \Phi' | \mathbf{I}_2^2 | \Phi \rangle = \frac{\hbar^2}{2} \left(-\tilde{\delta}_{m'_I, m_I-2} \tilde{\delta}_{m'_{S_h}, m_{S_h}} + \tilde{\delta}_{m'_I, m_I} \tilde{\delta}_{m'_{S_h}, m_{S_h}} \right. \\ \left. + \tilde{\delta}_{m_I, 0} \tilde{\delta}_{m'_I, 0} \tilde{\delta}_{m'_{S_h}, m_{S_h}} - \tilde{\delta}_{m'_I, m_I+2} \tilde{\delta}_{m'_{S_h}, m_{S_h}} \right), \quad (\text{C.10})$$

$$\langle \Phi' | \mathbf{I}_3^2 | \Phi \rangle = \hbar^2 m_I^2 \tilde{\delta}_{m'_I, m_I} \tilde{\delta}_{m'_{S_h}, m_{S_h}}, \quad (\text{C.11})$$

$$\langle \Phi' | \frac{\mathbf{I}_1 \mathbf{I}_2 + \mathbf{I}_2 \mathbf{I}_1}{2} | \Phi \rangle = \frac{\hbar^2}{2} \left(i \tilde{\delta}_{m'_I, m_I-2} \tilde{\delta}_{m'_{S_h}, m_{S_h}} - i \tilde{\delta}_{m'_I, m_I+2} \tilde{\delta}_{m'_{S_h}, m_{S_h}} \right), \quad (\text{C.12})$$

$$\langle \Phi' | \frac{\mathbf{I}_2 \mathbf{I}_3 + \mathbf{I}_3 \mathbf{I}_2}{2} | \Phi \rangle = \frac{\hbar^2}{4} \left(i(2m_I - 1) \sqrt{2} \tilde{\delta}_{m'_I, m_I-1} \tilde{\delta}_{m'_{S_h}, m_{S_h}} \right. \\ \left. - i(2m_I + 1) \sqrt{2} \tilde{\delta}_{m'_I, m_I+1} \tilde{\delta}_{m'_{S_h}, m_{S_h}} \right), \quad (\text{C.13})$$

$$\langle \Phi' | \frac{\mathbf{I}_1 \mathbf{I}_3 + \mathbf{I}_3 \mathbf{I}_1}{2} | \Phi \rangle = \frac{\hbar^2}{4} \left((2m_I - 1) \sqrt{2} \tilde{\delta}_{m'_I, m_I-1} \tilde{\delta}_{m'_{S_h}, m_{S_h}} \right. \\ \left. + (2m_I + 1) \sqrt{2} \tilde{\delta}_{m'_I, m_I+1} \tilde{\delta}_{m'_{S_h}, m_{S_h}} \right), \quad (\text{C.14})$$

$$\langle \Phi' | \frac{\mathbf{I}_1 \mathbf{S}_{h2} + \mathbf{I}_2 \mathbf{S}_{h1}}{2} | \Phi \rangle = \frac{\hbar^2}{2} \left(-i \tilde{\delta}_{m'_I, m_I-1} \tilde{\delta}_{m'_{S_h}, m_{S_h}-1} + i \tilde{\delta}_{m'_I, m_I+1} \tilde{\delta}_{m'_{S_h}, m_{S_h}+1} \right), \quad (\text{C.15})$$

$$\langle \Phi' | \frac{\mathbf{I}_2 \mathbf{S}_{h3} + \mathbf{I}_3 \mathbf{S}_{h2}}{2} | \Phi \rangle = \frac{\hbar^2}{4} \left(-i m_{S_h} \sqrt{2} \tilde{\delta}_{m'_I, m_I+1} \tilde{\delta}_{m'_{S_h}, m_{S_h}} - i m_I \sqrt{2} \tilde{\delta}_{m'_I, m_I} \tilde{\delta}_{m'_{S_h}, m_{S_h}+1} \right. \\ \left. + i m_{S_h} \sqrt{2} \tilde{\delta}_{m'_I, m_I-1} \tilde{\delta}_{m'_{S_h}, m_{S_h}} + i m_I \sqrt{2} \tilde{\delta}_{m'_I, m_I} \tilde{\delta}_{m'_{S_h}, m_{S_h}-1} \right), \quad (\text{C.16})$$

$$\langle \Phi' | \frac{\mathbf{I}_1 \mathbf{S}_{h3} + \mathbf{I}_3 \mathbf{S}_{h1}}{2} | \Phi \rangle = \frac{\hbar^2}{4} \left(m_{S_h} \sqrt{2} \tilde{\delta}_{m'_I, m_I+1} \tilde{\delta}_{m'_{S_h}, m_{S_h}} + m_I \sqrt{2} \tilde{\delta}_{m'_I, m_I} \tilde{\delta}_{m'_{S_h}, m_{S_h}+1} \right. \\ \left. + m_{S_h} \sqrt{2} \tilde{\delta}_{m'_I, m_I-1} \tilde{\delta}_{m'_{S_h}, m_{S_h}} + m_I \sqrt{2} \tilde{\delta}_{m'_I, m_I} \tilde{\delta}_{m'_{S_h}, m_{S_h}-1} \right). \quad (\text{C.17})$$

D

Functions for the calculation of energy surfaces in cuprous oxide

For the calculation of energy surfaces in cuprous oxide the functions c_5 , p , and q are needed. The c_i are the coefficients of the characteristic polynomial of the band-structure Hamiltonian $H_{\text{band}}(\mathbf{p}, \mathbf{I}, \mathbf{S}_h)$. The functions p and q can be expressed by these coefficients (see Eq. (5.34) and Eq. (5.35)). The following expressions are obtained

$$c_5 = -4\Delta, \quad (\text{D.1})$$

$$p = a_0 + a_1(p_1^2 + p_2^2 + p_3^2) + a_2(p_1^2 + p_2^2 + p_3^2)^2 + a_3(p_1^2 p_2^2 + p_1^2 p_3^2 + p_2^2 p_3^2), \quad (\text{D.2})$$

with the constant coefficients

$$a_0 = -\frac{\Delta^2}{3}, \quad (\text{D.3})$$

$$a_1 = -\frac{\Delta\eta_1}{m_0}, \quad (\text{D.4})$$

$$a_2 = -\frac{3}{100m_0^2} \left\{ \gamma_1'^2 (6\delta' - 5\mu')^2 + \eta_1^2 [25 + 2(5\nu - 6\tau)^2] \right\}, \quad (\text{D.5})$$

$$a_3 = \frac{9}{5m_0^2} \left[\gamma_1'^2 (\delta'^2 - 5\delta'\mu') + 2\eta_1^2 \tau (-5\nu + \tau) \right], \quad (\text{D.6})$$

and

$$q = b_0 + b_1(p_1^2 + p_2^2 + p_3^2) + b_2(p_1^2 + p_2^2 + p_3^2)^2 + b_3(p_1^2 + p_2^2 + p_3^2)^3 \quad (\text{D.7})$$

D. Functions for the calculation of energy surfaces in cuprous oxide

$$+ b_4(p_1^2 p_2^2 + p_1^2 p_3^2 + p_2^2 p_3^2) + b_5(p_1^2 + p_2^2 + p_3^2)(p_1^2 p_2^2 + p_1^2 p_3^2 + p_2^2 p_3^2) \\ + b_6(p_1^2 p_2^2 p_3^2),$$

with the constant coefficients

$$b_0 = \frac{2\Delta^3}{27}, \quad (\text{D.8})$$

$$b_1 = \frac{\Delta^2 \eta_1}{3m_0}, \quad (\text{D.9})$$

$$b_2 = \frac{\Delta \eta_1}{50m_0^2} [2\gamma_1'(6\delta' - 5\mu')(5\nu - 6\tau) - \eta_1(-5 + 5\nu - 6\tau)(5 + 5\nu - 6\tau)], \quad (\text{D.10})$$

$$b_3 = \frac{1}{500m_0^3} [\gamma_1'^3(6\delta' - 5\mu')^3 - 3\eta_1^2 \gamma_1'(6\delta' - 5\mu')(-10 + 5\nu - 6\tau)(5\nu - 6\tau) \\ - \eta_1^3(-5 + 10\nu - 12\tau)(5 + 5\nu - 6\tau)^2], \quad (\text{D.11})$$

$$b_4 = -\frac{6\Delta \eta_1}{5m_0^2} [\delta' \gamma_1'(5\nu - 2\tau) + \tau(5\gamma_1' \mu' + 5\eta_1 \nu - \eta_1 \tau)], \quad (\text{D.12})$$

$$b_5 = \frac{9}{50m_0^3} \left\{ -6\delta'^3 \gamma_1'^3 + 35\delta'^2 \gamma_1'^3 \mu' \right. \\ \left. - \eta_1^2 \tau [2\eta_1(5 + 5\nu - 6\tau)(5\nu - \tau) + 5\gamma_1' \mu'(10 - 10\nu + 7\tau)] \right. \\ \left. + \delta' \gamma_1' [-25\gamma_1'^2 \mu'^2 + \eta_1^2(25(-2 + \nu)\nu + 10(2 - 7\nu)\tau + 18\tau^2)] \right\}, \quad (\text{D.13})$$

$$b_6 = -\frac{27}{10m_0^3} (\delta' \gamma_1' - \eta_1 \tau) [2\delta'^2 \gamma_1'^2 + \eta_1 \tau(15\gamma_1' \mu' - 30\eta_1 \nu - 4\eta_1 \tau) \\ + \delta' \gamma_1'(15\gamma_1' \mu' + 2\eta_1 \tau)]. \quad (\text{D.14})$$

Spherically symmetric models can then be obtained by setting $\delta' = \tau = 0$.



Bibliography

- [1] J. Barrow-Green. *Poincare and the Three Body Problem*. History of mathematics. American Mathematical Society (1997).
- [2] N. C. Stone and N. W. C. Leigh. A statistical solution to the chaotic, non-hierarchical three-body problem. *Nature* 576, 406–410 (2019).
- [3] P. G. Breen, C. N. Foley, T. Boekholt, and S. P. Zwart. Newton versus the machine: solving the chaotic three-body problem using deep neural networks. *Monthly Notices of the Royal Astronomical Society* 494, 2465–2470 (2020).
- [4] S. Liao, X. Li, and Y. Yang. Three-body problem—From Newton to supercomputer plus machine learning. *New Astronomy* 96, 101850 (2022).
- [5] A. N. Kolmogorov. On conservation of conditionally periodic motions for a small change in Hamilton’s function. *Dokl. Akad. Nauk SSSR* 98, 527–530 (1954).
- [6] V. I. Arnold. Proof of a theorem of A. N. Kolmogorov on the invariance of quasi-periodic motions under small perturbations of the Hamiltonian. *Russian Mathematical Surveys* 18, 9 (1963).
- [7] J. Möser. On invariant curves of area-preserving mappings of an annulus. *Nachr. Akad. Wiss. Göttingen, II* pp. 1–20 (1962).
- [8] H. Poincaré. Sur un théoreme de géométrie. *Rendiconti del Circolo Matematico di Palermo (1884-1940)* 33, 375–407 (1912).
- [9] G. D. Birkhoff. Proof of Poincaré’s geometric theorem. *Transactions of the American Mathematical Society* 14, 14–22 (1913).
- [10] G. D. Birkhoff. An extension of Poincaré’s last geometric theorem. *Acta mathematica* 47, 297–311 (1926).

- [11] C. Mendoza and A. M. Mancho. Hidden geometry of ocean flows. *Physical Review Letters* 105, 038501 (2010).
- [12] A. M. Mancho, S. Wiggins, J. Curbelo, and C. Mendoza. Lagrangian descriptors: A method for revealing phase space structures of general time dependent dynamical systems. *Communications in Nonlinear Science and Numerical Simulation* 18, 3530–3557 (2013).
- [13] J. Daquin, R. Pédenon-Orlanducci, M. Agaoglou, G. García-Sánchez, and A. M. Mancho. Global dynamics visualisation from Lagrangian Descriptors. Applications to discrete and continuous systems. *Physica D: Nonlinear Phenomena* 442, 133520 (2022).
- [14] J. J. Balmer. Notiz über die Spectrallinien des Wasserstoffs. *Annalen der Physik* 261, 80–87 (1885).
- [15] J. R. Rydberg. On the structure of the line-spectra of the chemical elements. *The London, Edinburgh, and Dublin Philosophical Magazine and Journal of Science* 29, 331–337 (1890).
- [16] T. Lyman. The spectrum of hydrogen in the region of extremely short wave-lengths. *Astrophysical Journal*, vol. 23, p. 181 23, 181 (1906).
- [17] F. Paschen. Zur Kenntnis ultraroter Linienspektra. I. (Normalwellenlängen bis 27000 Å.-E.). *Annalen der Physik* 332, 537–570 (1908).
- [18] N. Bohr. On the constitution of atoms and molecules. *The London, Edinburgh, and Dublin Philosophical Magazine and Journal of Science* 26, 1–25 (1913).
- [19] A. Sommerfeld. Zur Quantentheorie der Spektrallinien. *Annalen der Physik* 356, 1–94 (1916).
- [20] A. Einstein. Zum Quantensatz von Sommerfeld und Epstein. *Verh. d. D. Physik. Ges.* pp. 82–92 (1917).
- [21] J. B. Keller. Corrected Bohr-Sommerfeld quantum conditions for nonseparable systems. *Annals of Physics* 4, 180–188 (1958).
- [22] L. Brillouin. Remarques sur la mécanique ondulatoire. *J. Phys. Radium* 7, 353–368 (1926).
- [23] M. V. Berry and M. Tabor. Closed orbits and the regular bound spectrum. *Proceedings of the Royal Society of London. A. Mathematical and Physical Sciences* 349, 101–123 (1976).

-
- [24] M. V. Berry and M. Tabor. Calculating the bound spectrum by path summation in action-angle variables. *Journal of Physics A: Mathematical and General* 10, 371 (1977).
- [25] M. C. Gutzwiller. Phase-Integral Approximation in Momentum Space and the Bound States of an Atom. *Journal of Mathematical Physics* 8, 1979–2000 (1967).
- [26] M. C. Gutzwiller. Periodic Orbits and Classical Quantization Conditions. *Journal of Mathematical Physics* 12, 343–358 (1971).
- [27] M. C. Gutzwiller. *Chaos in Classical and Quantum Mechanics*. Springer, New York (1990).
- [28] K. Richter, J. S. Briggs, D. Wintgen, and E. A. Solov'ev. Novel dynamical symmetries of asymmetrically doubly excited two-electron atoms. *Journal of Physics B: Atomic, Molecular and Optical Physics* 25, 3929 (1992).
- [29] D. Wintgen, K. Richter, and G. Tanner. The semiclassical helium atom. *Chaos: An Interdisciplinary Journal of Nonlinear Science* 2, 19–33 (1992).
- [30] G. Tanner and D. Wintgen. Semiclassical quantization of intermittency in helium. *Physical Review Letters* 75, 2928 (1995).
- [31] H. Friedrich and D. Wintgen. The hydrogen atom in a uniform magnetic field – An example of chaos. *Physics Reports* 183, 37–79 (1989).
- [32] H. Hasegawa, M. Robnik, and G. Wunner. Classical and Quantal Chaos in the Diamagnetic Kepler Problem. *Progress of Theoretical Physics Supplement* 98, 198–286 (1989).
- [33] G. Tanner, K. T. Hansen, and J. Main. The semiclassical resonance spectrum of hydrogen in a constant magnetic field. *Nonlinearity* 9, 1641 (1996).
- [34] T. Bartsch, J. Main, and G. Wunner. Semiclassical quantization of the hydrogen atom in crossed electric and magnetic fields. *Physical Review A* 67, 063411 (2003).
- [35] S. Gekle, J. Main, T. Bartsch, and T. Uzer. Hydrogen atom in crossed electric and magnetic fields: Phase space topology and torus quantization via periodic orbits. *Physical Review A* 75, 023406 (2007).
- [36] J. Frenkel. On the transformation of light into heat in solids. I. *Physical Review* 37, 17–44 (1931).
- [37] J. Frenkel. On the transformation of light into heat in solids. II. *Physical Review* 37, 1276–1294 (1931).

- [38] J. Frenkel. On the absorption of light and the trapping of electrons and positive holes in crystalline dielectrics. *Phys. Z. Sowjetunion* 9, 533 (1936).
- [39] R. Peierls. Zur Theorie der Absorptionsspektren fester Körper. *Annalen der Physik* 405, 905–952 (1932).
- [40] G. H. Wannier. The Structure of Electronic Excitation Levels in Insulating Crystals. *Physical Review* 52, 191–197 (1937).
- [41] R. S. Knox. *Theory of excitons*. Solid state physics: Supplement. Academic Press (1963).
- [42] E. F. Gross and I. A. Karryjew. The optical spectrum of the exciton. *Dokl. Akad. Nauk SSSR* 84 (1952).
- [43] T. Kazimierzuk, D. Fröhlich, S. Scheel, H. Stolz, and M. Bayer. Giant Rydberg excitons in the copper oxide Cu_2O . *Nature* 514, 343–347 (2014).
- [44] M. A. M. Versteegh, S. Steinhauer, J. Bajo, T. Lettner, A. Soro, A. Romanova, S. Gyger, L. Schweickert, A. Mysyrowicz, and V. Zwiller. Giant Rydberg excitons in Cu_2O probed by photoluminescence excitation spectroscopy. *Physical Review B* 104, 245206 (2021).
- [45] J. Thewes, J. Heckötter, T. Kazimierzuk, M. Aßmann, D. Fröhlich, M. Bayer, M. A. Semina, and M. M. Glazov. Observation of high angular momentum excitons in cuprous oxide. *Physical Review Letters* 115, 027402 (2015).
- [46] F. Schweiner, J. Main, M. Feldmaier, G. Wunner, and C. Uihlein. Impact of the valence band structure of Cu_2O on excitonic spectra. *Physical Review B* 93, 195203 (2016).
- [47] F. Schöne, S.-O. Krüger, P. Grünwald, M. Aßmann, J. Heckötter, J. Thewes, H. Stolz, D. Fröhlich, M. Bayer, and S. Scheel. Coupled valence band dispersions and the quantum defect of excitons in Cu_2O . *Journal of Physics B: Atomic, Molecular and Optical Physics* 49, 134003 (2016).
- [48] F. Schöne, S.-O. Krüger, P. Grünwald, H. Stolz, S. Scheel, M. Aßmann, J. Heckötter, J. Thewes, D. Fröhlich, and M. Bayer. Deviations of the exciton level spectrum in Cu_2O from the hydrogen series. *Physical Review B* 93, 075203 (2016).
- [49] J. M. Luttinger and W. Kohn. Motion of Electrons and Holes in Perturbed Periodic Fields. *Physical Review* 97, 869–883 (1955).
- [50] J. M. Luttinger. Quantum Theory of Cyclotron Resonance in Semiconductors: General Theory. *Physical Review* 102, 1030–1041 (1956).

-
- [51] K. Suzuki and J. C. Hensel. Quantum resonances in the valence bands of germanium. I. Theoretical considerations. *Physical Review B* 9, 4184–4218 (1974).
- [52] J. B. Grun, M. Sieskind, and S. Nikitine. Détermination de l'intensité d'oscillateur des raies de la série verte de Cu_2O aux basses températures. *J. Phys. Radium* 22, 176–178 (1961).
- [53] P. Rommel, P. Zielinski, and J. Main. Green exciton series in cuprous oxide. *Physical Review B* 101, 075208 (2020).
- [54] S. Zielińska-Raczyńska, D. Ziemkiewicz, and G. Czajkowski. Electro-optical properties of Rydberg excitons. *Physical Review B* 94, 045205 (2016).
- [55] F. Schweiner, J. Main, G. Wunner, and C. Uihlein. K-dependent exchange interaction of the $1S$ orthoexciton in Cu_2O . *Physical Review B* 94, 115201 (2016).
- [56] P. Grünwald, M. Aßmann, J. Heckötter, D. Fröhlich, M. Bayer, H. Stolz, and S. Scheel. Signatures of quantum coherences in Rydberg excitons. *Physical Review Letters* 117, 133003 (2016).
- [57] F. Schöne, H. Stolz, and N. Naka. Phonon-assisted absorption of excitons in Cu_2O . *Physical Review B* 96, 115207 (2017).
- [58] F. Schweiner, J. Main, G. Wunner, M. Freitag, J. Heckötter, C. Uihlein, M. Aßmann, D. Fröhlich, and M. Bayer. Magnetoexcitons in cuprous oxide. *Physical Review B* 95, 035202 (2017).
- [59] F. Schweiner, J. Main, and G. Wunner. Magnetoexcitons Break Antiunitary Symmetries. *Physical Review Letters* 118, 046401 (2017).
- [60] F. Schweiner, J. Main, G. Wunner, and C. Uihlein. Even exciton series in Cu_2O . *Physical Review B* 95, 195201 (2017).
- [61] F. Schweiner, J. Main, and G. Wunner. GOE-GUE-Poisson transitions in the nearest-neighbor spacing distribution of magnetoexcitons. *Physical Review E* 95, 062205 (2017).
- [62] F. Schweiner, P. Rommel, J. Main, and G. Wunner. Exciton-phonon interaction breaking all antiunitary symmetries in external magnetic fields. *Physical Review B* 96, 035207 (2017).
- [63] F. Schweiner, J. Ertl, J. Main, G. Wunner, and C. Uihlein. Exciton-polaritons in cuprous oxide: Theory and comparison with experiment. *Physical Review B* 96, 245202 (2017).

- [64] F. Schweiner, J. Laturner, J. Main, and G. Wunner. Crossover between the Gaussian orthogonal ensemble, the Gaussian unitary ensemble, and Poissonian statistics. *Physical Review E* 96, 052217 (2017).
- [65] D. Semkat, S. Sobkowiak, F. Schöne, H. Stolz, T. Koch, and H. Fehske. Multi-component exciton gas in cuprous oxide: cooling behaviour and the role of Auger decay. *Journal of Physics B: Atomic, Molecular and Optical Physics* 50, 204001 (2017).
- [66] J. Heckötter, M. Freitag, D. Fröhlich, M. Aßmann, M. Bayer, M. A. Semina, and M. M. Glazov. Scaling laws of Rydberg excitons. *Physical Review B* 96, 125142 (2017).
- [67] J. Heckötter, M. Freitag, D. Fröhlich, M. Aßmann, M. Bayer, M. A. Semina, and M. M. Glazov. High-resolution study of the yellow excitons in Cu_2O subject to an electric field. *Physical Review B* 95, 035210 (2017).
- [68] M. Takahata and N. Naka. Photoluminescence properties of the entire excitonic series in Cu_2O . *Physical Review B* 98, 195205 (2018).
- [69] V. Walther, S.-O. Krüger, S. Scheel, and T. Pohl. Interactions between Rydberg excitons in Cu_2O . *Physical Review B* 98, 165201 (2018).
- [70] S. Zielińska-Raczyńska, D. Ziemkiewicz, and G. Czajkowski. Electro-optical properties of Cu_2O for P excitons in the regime of Franz-Keldysh oscillations. *Physical Review B* 97, 165205 (2018).
- [71] S. A. Lynch, C. Hodges, W. W. Langbein, L. Gallagher, J. Rogers, C. S. Adams, M. P. A. Jones, and R. P. Singh. Giant Rydberg excitons in synthetic and artificial cuprous oxide. In *20th International Conference on Transparent Optical Networks (ICTON)*, pp. 1–4. IEEE (2018).
- [72] P. Rommel, F. Schweiner, J. Main, J. Heckötter, M. Freitag, D. Fröhlich, K. Lehninger, M. Aßmann, and M. Bayer. Magneto-Stark effect of yellow excitons in cuprous oxide. *Physical Review B* 98, 085206 (2018).
- [73] J. Heckötter, M. Freitag, D. Fröhlich, M. Aßmann, M. Bayer, P. Grünwald, F. Schöne, D. Semkat, H. Stolz, and S. Scheel. Rydberg excitons in the presence of an ultralow-density electron-hole plasma. *Physical Review Letters* 121, 097401 (2018).
- [74] H. Stolz, F. Schöne, and D. Semkat. Interaction of Rydberg excitons in cuprous oxide with phonons and photons: optical linewidth and polariton effect. *New Journal of Physics* 20, 023019 (2018).

-
- [75] S.-O. Krüger and S. Scheel. Waveguides for Rydberg excitons in Cu_2O from strain traps. *Physical Review B* 97, 205208 (2018).
- [76] S. Zielińska-Raczyńska, G. Czajkowski, K. Karpiński, and D. Ziemkiewicz. Non-linear optical properties and self-Kerr effect of Rydberg excitons. *Physical Review B* 99, 245206 (2019).
- [77] A. M. Konzelmann, S.-O. Krüger, and H. Giessen. Interaction of orbital angular momentum light with Rydberg excitons: Modifying dipole selection rules. *Physical Review B* 100, 115308 (2019).
- [78] S.-O. Krüger and S. Scheel. Interseries transitions between Rydberg excitons in Cu_2O . *Physical Review B* 100, 085201 (2019).
- [79] V. Walther and T. Pohl. Plasma-enhanced interaction and optical nonlinearities of Cu_2O Rydberg excitons. *Physical Review Letters* 125, 097401 (2020).
- [80] D. Ziemkiewicz, K. Karpiński, G. Czajkowski, and S. Zielińska-Raczyńska. Excitons in Cu_2O : From quantum dots to bulk crystals and additional boundary conditions for Rydberg exciton-polaritons. *Physical Review B* 101, 205202 (2020).
- [81] P. Zielinski, P. Rommel, F. Schweiner, and J. Main. Rydberg excitons in electric and magnetic fields obtained with the complex-coordinate-rotation method. *Journal of Physics B: Atomic, Molecular and Optical Physics* 53, 054004 (2020).
- [82] P. Rommel, J. Main, A. Farenbruch, J. Mund, D. Fröhlich, D. R. Yakovlev, M. Bayer, and C. Uihlein. Second harmonic generation of cuprous oxide in magnetic fields. *Physical Review B* 101, 115202 (2020).
- [83] S.-O. Krüger, H. Stolz, and S. Scheel. Interaction of charged impurities and Rydberg excitons in cuprous oxide. *Physical Review B* 101, 235204 (2020).
- [84] A. Farenbruch, D. Fröhlich, D. R. Yakovlev, and M. Bayer. Rydberg Series of Dark Excitons in Cu_2O . *Physical Review Letters* 125, 207402 (2020).
- [85] A. Farenbruch, J. Mund, D. Fröhlich, D. R. Yakovlev, M. Bayer, M. A. Semina, and M. M. Glazov. Magneto-Stark and Zeeman effect as origin of second harmonic generation of excitons in Cu_2O . *Physical Review B* 101, 115201 (2020).
- [86] J. Heckötter, V. Walther, S. Scheel, M. Bayer, T. Pohl, and M. Aßmann. Asymmetric Rydberg blockade of giant excitons in Cuprous Oxide. *Nat. Commun.* 12, 3556 (2021).
- [87] D. Ziemkiewicz, G. Czajkowski, K. Karpiński, and S. Zielińska-Raczyńska. Electro-optical properties of excitons in Cu_2O quantum wells. I. Discrete states. *Physical Review B* 104, 075303 (2021).

- [88] S. A. Lynch, C. Hodges, Soumen Mandal, W. Langbein, R. P. Singh, L. A. P. Gallagher, J. D. Pritchett, D. Pizzey, J. P. Rogers, C. S. Adams, et al. Rydberg excitons in synthetic cuprous oxide Cu_2O . *Physical Review Materials* 5, 084602 (2021).
- [89] P. Rommel, J. Main, A. Farenbruch, D. R. Yakovlev, and M. Bayer. Exchange interaction in the yellow exciton series of cuprous oxide. *Physical Review B* 103, 075202 (2021).
- [90] P. Rommel, J. Main, S.-O. Krüger, and S. Scheel. Interseries dipole transitions from yellow to green excitons in cuprous oxide. *Physical Review B* 104, 085204 (2021).
- [91] J. Heckötter, P. Rommel, J. Main, M. Aßmann, and M. Bayer. Analysis of the Fine Structure of the D-Exciton Shell in Cuprous Oxide. *Physica Status Solidi (RRL)–Rapid Research Letters* 15, 2100335 (2021).
- [92] A. Farenbruch, D. Fröhlich, H. Stolz, D. R. Yakovlev, and M. Bayer. Second-harmonic generation of blue series excitons and magnetoexcitons in Cu_2O . *Physical Review B* 104, 075203 (2021).
- [93] L. A. P. Gallagher, J. P. Rogers, J. D. Pritchett, R. A. Mistry, D. Pizzey, C. S. Adams, M. P. A. Jones, P. Grünwald, V. Walther, C. Hodges, et al. Microwave-optical coupling via Rydberg excitons in cuprous oxide. *Physical Review Research* 4, 013031 (2022).
- [94] K. Orfanakis, S. K. Rajendran, V. Walther, T. Volz, T. Pohl, and H. Ohadi. Rydberg exciton–polaritons in a Cu_2O microcavity. *Nature Materials* 21, 767–772 (2022).
- [95] A. Neubauer, J. Heckötter, M. Ubl, M. Hentschel, B. Panda, M. Aßmann, M. Bayer, and H. Giessen. Spectroscopy of nanoantenna-covered Cu_2O : Towards enhancing quadrupole transitions in Rydberg excitons. *Physical Review B* 106, 165305 (2022).
- [96] C. Morin, J. Tignon, J. Mangeney, S. Dhillon, G. Czajkowski, K. Karpiński, S. Zielińska-Raczyńska, D. Ziemkiewicz, and T. Boulier. Self-Kerr effect across the yellow Rydberg series of excitons in Cu_2O . *Physical Review Letters* 129, 137401 (2022).
- [97] D. Ziemkiewicz and S. Zielińska-Raczyńska. Copper plasmonics with excitons. *Physical Review B* 106, 205404 (2022).
- [98] J. P. Rogers, L. A. P. Gallagher, D. Pizzey, J. D. Pritchett, C. S. Adams, M. P. A. Jones, C. Hodges, W. Langbein, and S. A. Lynch. High-resolution nanosecond

- spectroscopy of even-parity Rydberg excitons in Cu_2O . *Physical Review B* 105, 115206 (2022).
- [99] M. Bergen, V. Walther, B. Panda, M. Harati, S. Siegeroth, J. Heckötter, and M. Aßmann. Large scale purification in semiconductors using Rydberg excitons. *Nature Communications* 14, 8235 (2023).
- [100] D. Ziemkiewicz, K. Karpiński, and S. Zielińska-Raczyńska. Excitonic superlens with copper and copper oxide. *Physical Review B* 108, 075307 (2023).
- [101] P. A. Belov, F. Morawetz, S.-O. Krüger, N. Scheuler, P. Rommel, J. Main, H. Giessen, and S. Scheel. Energy states of excitons in finite crystals: From weak to strong confinement. *Physical Review B* 109, 235404 (2024).
- [102] J. DeLange, K. Barua, A. S. Paul, H. Ohadi, V. Zwiller, S. Steinhauer, and H. Alaeian. Highly-excited Rydberg excitons in synthetic thin-film cuprous oxide. *Scientific Reports* 13, 16881 (2023).
- [103] D. Ziemkiewicz and S. Zielińska-Raczyńska. Optical-to-microwave frequency conversion with Rydberg excitons. *Physical Review B* 107, 195303 (2023).
- [104] P. Egenlauf, P. Rommel, and J. Main. Gaussian-process-regression-based method for the localization of exceptional points in complex resonance spectra. *Machine Learning: Science and Technology* 5, 015045 (2024).
- [105] M. Makhonin, A. Delphan, K. W. Song, P. Walker, T. Isoniemi, P. Claronino, K. Orfanakis, S. K. Rajendran, H. Ohadi, J. Heckötter, et al. Nonlinear Rydberg exciton-polaritons in Cu_2O microcavities. *Light: Science & Applications* 13, 47 (2024).
- [106] J. Heckötter, B. Panda, K. Brägelmann, M. Aßmann, and M. Bayer. A Temperature Study of High- n Rydberg States in Cu_2O . *Advanced Quantum Technologies* (2024).
- [107] K. Morin, D. Lagarde, A. Gillet, X. Marie, and T. Boulier. Large-scale characterization of Cu_2O monocrystals via Rydberg excitons. *Physical Review Materials* 8, 026202 (2024).
- [108] D. Ziemkiewicz, G. Czajkowski, and S. Zielińska-Raczyńska. Optical properties of Rydberg excitons in Cu_2O -based superlattices. *Physical Review B* 109, 085309 (2024).
- [109] N. Scheuler, P. Rommel, J. Main, and P. A. Belov. Resonance energies and linewidths of Rydberg excitons in Cu_2O quantum wells. *Physical Review B* 109, 165440 (2024).

- [110] A. S. Paul, S. K. Rajendran, D. Ziemkiewicz, T. Volz, and H. Ohadi. Local tuning of Rydberg exciton energies in nanofabricated Cu_2O pillars. *Communications Materials* 5, 43 (2024).
- [111] J. D. Pritchett, L. A. P. Gallagher, A. Brewin, H. Q. X. Wong, W. Langbein, S. A. Lynch, C. S. Adams, and M. Jones. Giant microwave–optical Kerr nonlinearity via Rydberg excitons in cuprous oxide. *APL Photonics* 9, 031303 (2024).
- [112] J. Luft. *Closed-Orbit Theorie für Magnetoexcitonen in Kupferoxydul*. Master’s thesis, Universität Stuttgart (2018).
- [113] C. Deter. *Klassische Bahnen in Kupferoxydul unter Berücksichtigung des Quasispins*. Bachelor’s thesis, Universität Stuttgart (2019).
- [114] J. Ertl. *Adiabatic approximation for the dynamics of magnetoexcitons in Cu_2O* . Master’s thesis, Universität Stuttgart (2019).
- [115] J. Ertl, P. Rommel, M. Mom, J. Main, and M. Bayer. Classical and semiclassical description of Rydberg excitons in cuprous oxide. *Physical Review B* 101, 241201 (2020).
- [116] M. Aßmann, J. Thewes, D. Fröhlich, and M. Bayer. Quantum chaos and breaking of all anti-unitary symmetries in Rydberg excitons. *Nature materials* 15, 741–745 (2016).
- [117] M. Freitag, J. Heckötter, M. Bayer, and M. Aßmann. Role of phonons in the quantum chaos of Rydberg excitons. *Physical Review B* 95, 155204 (2017).
- [118] J. Ertl, M. Marquardt, M. Schumacher, P. Rommel, J. Main, and M. Bayer. Classical dynamics and semiclassical analysis of excitons in cuprous oxide. *Physical Review B* 109, 165203 (2024).
- [119] J. Ertl, S. Rentschler, and J. Main. Rydberg excitons in cuprous oxide: A two-particle system with classical chaos. *Chaos* submitted (2024).
- [120] J. Main. Use of harmonic inversion techniques in semiclassical quantization and analysis of quantum spectra. *Phys. Rep.* 316, 233–338 (1999).
- [121] J. Ertl, M. Marquardt, M. Schumacher, P. Rommel, J. Main, and M. Bayer. Signatures of Exciton Orbits in Quantum Mechanical Recurrence Spectra of Cu_2O . *Physical Review Letters* 129, 067401 (2022).
- [122] C. Uihlein, D. Fröhlich, and R. Kenklies. Investigation of exciton fine structure in Cu_2O . *Physical Review B* 23, 2731–2740 (1981).

-
- [123] R. S. Womersley. Efficient spherical designs with good geometric properties. *Contemporary computational mathematics-A celebration of the 80th birthday of Ian Sloan* pp. 1243–1285 (2018).
- [124] J. Heckötter, A. Farenbruch, D. Fröhlich, M. Aßmann, D. R. Yakovlev, M. Bayer, M. A. Semina, M. M. Glazov, P. Rommel, J. Ertl, J. Main, and H. Stolz. The energy level spectrum of the yellow exciton series in cuprous oxide. *Physics Reports* submitted (2024).
- [125] J. Main. Nichtlineare Dynamik. Lecture, Universität Stuttgart (2016-2017).
- [126] S. Wimberger. *Nonlinear dynamics and quantum chaos*, volume 10. Springer (2014).
- [127] V. I. Arnold. *Mathematical Methods of Classical Mechanics*. Springer, Berlin (1989).
- [128] A. J. Lichtenberg and M. A. Leiberman. *Regular and chaotic dynamics*, volume 38. Springer Science & Business Media (2013).
- [129] H. G. Schuster and W. Just. *Deterministic Chaos: An Introduction*. John Wiley & Sons (2005).
- [130] M. Tabor. Chaos and Integrability in Nonlinear Dynamics: An Introduction, Wiley Interscience. *Chaos and Integrability in Nonlinear Dynamics: An Introduction* (1989).
- [131] E. Ott. *Chaos in dynamical systems*. Cambridge university press (2002).
- [132] J. Moser. *Stable and random motions in dynamical systems: With special emphasis on celestial mechanics*, volume 1. Princeton university press (2001).
- [133] V. I. Arnold and A. Avez. *Ergodic problems of classical mechanics*. W. A. Benjamin, New York (1968).
- [134] F. Schwabl. *Statistische Mechanik*. Springer (2006).
- [135] M. Brack and R. Bhaduri. *Semiclassical physics*. Addison-Wesley Publishing (1997).
- [136] G. Wentzel. Eine Verallgemeinerung der Quantenbedingungen für die Zwecke der Wellenmechanik. *Zeitschrift für Physik* 38, 518–529 (1926).
- [137] H. A. Kramers. Wellenmechanik und halbzahlige Quantisierung. *Zeitschrift für Physik* 39, 828–840 (1926).

- [138] L. Brillouin. La mécanique ondulatoire de Schrödinger; une méthode générale de résolution par approximations successives. *CR Acad. Sci* 183, 24–26 (1926).
- [139] V. P. Maslov and M. V. Fedoriuk. *Semi-classical approximation in quantum mechanics*, volume 7. Springer Science & Business Media (2001).
- [140] E. C. Titchmarsh. *Introduction to the theory of Fourier integrals*, volume 2. Clarendon Press, Oxford (1948).
- [141] S. C. Creagh and R. G. Littlejohn. Semiclassical trace formulas in the presence of continuous symmetries. *Physical Review A* 44, 836–850 (1991).
- [142] S. Tomsovic, M. Grinberg, and D. Ullmo. Semiclassical Trace Formulas of Near-Integrable Systems: Resonances. *Physical Review Letters* 75, 4346–4349 (1995).
- [143] J. H. Van Vleck. The correspondence principle in the statistical interpretation of quantum mechanics. *Proceedings of the National Academy of Sciences* 14, 178–188 (1928).
- [144] S. Hunklinger. *Festkörperphysik*. De Gruyter Oldenbourg, Berlin, Boston (2018).
- [145] C. Kittel and P. McEuen. *Introduction to solid state physics*. John Wiley & Sons (2018).
- [146] U. Rössler. *Solid State Theory: An Introduction*. Advanced Texts in Physics. Springer Berlin Heidelberg (2004).
- [147] C. F. Klingshirn. *Semiconductor Optics*. Advanced texts in physics. Springer Berlin Heidelberg (2007).
- [148] J. Ertl. *Polaritontransformation der gelben Magnetoexzitonen in Kupferoxydul*. Bachelor’s thesis, Universität Stuttgart (2017).
- [149] M. Born and R. Oppenheimer. Zur Quantentheorie der Molekeln. *Annalen der Physik* 389, 457–484 (1927).
- [150] Enrico Fermi. Zur Quantelung des idealen einatomigen Gases. *Zeitschrift für Physik* 36, 902–912 (1926).
- [151] E. Wigner and F. Seitz. On the Constitution of Metallic Sodium. *Physical Review* 43, 804–810 (1933).
- [152] A. Bravais. *Abhandlung über die Systeme von regelmässig auf einer Ebene oder im Raum vertheilten Punkten*. W. Engelmann (1897).
- [153] S. K. Chatterjee. *Crystallography and the World of Symmetry*, volume 113. Springer Science & Business Media (2008).

-
- [154] L. Brillouin. Les électrons libres dans les métaux et le rôle des réflexions de Bragg. *J. Phys. Radium* 1, 377–400 (1930).
- [155] F. Bloch. Über die Quantenmechanik der Elektronen in Kristallgittern. *Zeitschrift für Physik* 52, 555–600 (1929).
- [156] A. Werner and H. D. Hochheimer. High-pressure x-ray study of Cu_2O and Ag_2O . *Physical Review B* 25, 5929–5934 (1982).
- [157] M. Jörger. *Terahertzspektroskopie an Cu_2O : Intraexzitonische und phononische Übergänge*. Ph.D. thesis, Karlsruher Institut für Technologie (KIT) (2004).
- [158] H. E. Swanson and R. K. Fuyat. Standard X-ray diffraction powder patterns. *NBS Circular* 539 II, 23 (1953).
- [159] J. W. Hodby, T. E. Jenkins, C. Schwab, H. Tamura, and D. Trivich. Cyclotron resonance of electrons and of holes in cuprous oxide, Cu_2O . *Journal of Physics C: Solid State Physics* 9, 1429 (1976).
- [160] O. Madelung, U. Rössler, and M. Schulz (editors). *Landolt-Börnstein - Group III Condensed Matter*. Springer-Verlag, Berlin Heidelberg (1998).
- [161] P. R. Markworth, R. P. H. Chang, Y. Sun, G. K. Wong, and J. B. Ketterson. Epitaxial stabilization of orthorhombic cuprous oxide films on MgO (110). *Journal of Materials Research* 16, 914–921 (2001).
- [162] T. Ito, H. Yamaguchi, K. Okabe, and T. Masumi. Single-crystal growth and characterization of Cu_2O and CuO . *Journal of materials science* 33, 3555–3566 (1998).
- [163] Y. Sui, W. Fu, H. Yang, Y. Zeng, Y. Zhang, Q. Zhao, Y. Li, X. Zhou, Y. Leng, M. Li, et al. Low temperature synthesis of Cu_2O crystals: shape evolution and growth mechanism. *Crystal Growth & Design* 10, 99–108 (2010).
- [164] S. Steinhauer, M. A. M. Versteegh, S. Gyger, A. W. Elshaari, B. Kunert, A. Mysyrowicz, and V. Zwiller. Rydberg excitons in Cu_2O microcrystals grown on a silicon platform. *Communications Materials* 1, 11 (2020).
- [165] D. R. Hartree. The wave mechanics of an atom with a non-Coulomb central field. Part I. Theory and methods. *Mathematical Proceedings of the Cambridge Philosophical Society* 24, 89–110 (1928).
- [166] R. McWeeny. Natural units in atomic and molecular physics. *Nature* 243, 196–198 (1973).

- [167] M. Feldmaier, J. Main, F. Schweiner, H. Cartarius, and G. Wunner. Rydberg systems in parallel electric and magnetic fields: an improved method for finding exceptional points. *Journal of Physics B: Atomic, Molecular and Optical Physics* 49, 144002 (2016).
- [168] J. Robertson. Electronic structure and x-ray near-edge core spectra of Cu_2O . *Physical Review B* 28, 3378–3385 (1983).
- [169] G. F. Koster, J. O. Dimmock, R. G. Wheeler, and H. Statz. *Properties of the thirty-two point groups*. Massachusetts Institute of Technology Press research monograph. M.I.T. Press, Cambridge (1963).
- [170] F. Schwabl. *Quantenmechanik für Fortgeschrittene (QM II)*. Springer-Verlag (2008).
- [171] A. R. Edmonds. *Angular Momentum in Quantum Mechanics*. Princeton University Press, Princeton (1957).
- [172] A. Baldereschi and N. O. Lipari. Spherical model of shallow acceptor states in semiconductors. *Physical Review B* 8, 2697 (1973).
- [173] A. Baldereschi and N. O. Lipari. Cubic contributions to the spherical model of shallow acceptor states. *Physical Review B* 9, 1525 (1974).
- [174] J. Broeckx. Acceptor excitation spectra in germanium in a uniform magnetic field. *Physical Review B* 43, 9643–9648 (1991).
- [175] F. Schweiner. *Theory of excitons in cuprous oxide*. Ph.D. thesis, Universität Stuttgart (2017).
- [176] W. Nolting. *Grundkurs Theoretische Physik 5/2: Quantenmechanik-Methoden und Anwendungen*. Springer (2015).
- [177] E. Anderson, Z. Bai, C. Bischof, S. Blackford, J. Demmel, J. Dongarra, J. D. Croz, A. Greenbaum, S. Hammarling, and A. McKenney. *LAPACK Users' Guide, Third edition*. Society for Industrial and Applied Mathematics, Philadelphia (1999).
- [178] J. Bewersdorff. *Algebra für Einsteiger*. Springer (2019).
- [179] R.W. Brankin, I. Gladwell, and L.F. Shampine. *RKSUITE: a suite of Runge-Kutta codes for the initial value problem for ODEs, Softreport 92-S1*. Department of Mathematics, Southern Methodist University, Dallas, Texas (1992).
- [180] S. Gekle, J. Main, T. Bartsch, and T. Uzer. Extracting Multidimensional Phase Space Topology from Periodic Orbits. *Physical Review Letters* 97, 104101 (2006).

-
- [181] P. Cvitanović and B. Eckhardt. Periodic-orbit quantization of chaotic systems. *Physical Review Letters* 63, 823–826 (1989).
- [182] A. Holle, J. Main, G. Wiebusch, H. Rottke, and K. H. Welge. Quasi-Landau Spectrum of the Chaotic Diamagnetic Hydrogen Atom. *Physical Review Letters* 61, 161–164 (1988).
- [183] J. Main and G. Wunner. Periodic Orbit Quantization of Mixed Regular Chaotic Systems. *Physical Review Letters* 82, 3038–3041 (1999).
- [184] M. Marquardt. *Semiclassical quantization for the states of cuprous oxide in consideration of the band structure*. Master’s thesis, Universität Stuttgart (2021).
- [185] M. Schumacher. *Semiclassical analysis and interpretation of quantum mechanically computed Cu_2O exciton spectra*. Master’s thesis, Universität Stuttgart (2021).
- [186] F. Haake. *Quantum signatures of chaos*. Springer (1991).
- [187] M. F. Herman. Nonadiabatic semiclassical scattering. I. Analysis of generalized surface hopping procedures. *The Journal of chemical physics* 81, 754–763 (1984).
- [188] J. C. Tully. Molecular dynamics with electronic transitions. *The Journal of Chemical Physics* 93, 1061–1071 (1990).
- [189] S. Hammes-Schiffer and J. C. Tully. Proton transfer in solution: Molecular dynamics with quantum transitions. *The Journal of Chemical Physics* 101, 4657–4667 (1994).
- [190] M. Barbatti. Nonadiabatic dynamics with trajectory surface hopping method. *WIREs Computational Molecular Science* 1, 620–633 (2011).
- [191] W. Dou and J. E. Subotnik. Nonadiabatic Molecular Dynamics at Metal Surfaces. *The Journal of Physical Chemistry A* 124, 757–771 (2020).
- [192] R. Schleicher. *Quantenmechanisches und semiklassisches Modell zum Zerfall der grünen Exzitonzustände*. Bachelor’s thesis, Universität Stuttgart (2023).
- [193] E. Stiefel and P. Kustaanheimo. Perturbation theory of Kepler motion based on spinor regularization. *Journal für die reine und angewandte Mathematik* 218, 204–219 (1965).
- [194] G. Scheifele and E. Stiefel. Linear and regular celestial mechanics, Band 174 von Grundlehren der mathematischen Wissenschaften (1971).
- [195] C. E. Rasmussen and C. K. I. Williams. *Gaussian Processes for Machine Learning*. The MIT Press (2005).

- [196] W. R. S. Garton and F. S. Tomkins. Diamagnetic Zeeman effect and magnetic configuration mixing in long spectral series of Ba I. *The Astrophysical Journal* 158, 839 (1969).
- [197] A. R. Edmonds. The theory of the quadratic Zeeman effect. *Le Journal de Physique Colloques* 31, C4–71 (1970).
- [198] K. T. Lu, F. S. Tomkins, and W. R. S. Garton. Configuration interaction effect on diamagnetic phenomena in atoms: strong mixing and Landau regions. *Proceedings of the Royal Society of London. A. Mathematical and Physical Sciences* 362, 421–424 (1978).
- [199] N. P. Economou, R. R. Freeman, and P. F. Liao. Diamagnetic structure of Rb in intense magnetic fields. *Physical Review A* 18, 2506 (1978).
- [200] R. J. Fonck, F. L. Roesler, D. H. Tracy, and Frank S. Tomkins. Comparison of atomic quasi-Landau spectrum with semiclassical strong-field-mixing models. *Physical Review A* 21, 861 (1980).
- [201] J. C. Castro, M. L. Zimmerman, R. G. Hulet, D. Kleppner, and R. R. Freeman. Origin and structure of the quasi-Landau resonances. *Physical Review Letters* 45, 1780 (1980).
- [202] J. Main, G. Wiebusch, A. Holle, and K. H. Welge. New Quasi-Landau Structure of Highly Excited Atoms: The Hydrogen Atom. *Physical Review Letters* 57, 2789–2792 (1986).
- [203] A. Holle, G. Wiebusch, J. Main, B. Hager, H. Rottke, and K. H. Welge. Diamagnetism of the Hydrogen Atom in the Quasi-Landau Regime. *Physical Review Letters* 56, 2594–2597 (1986).
- [204] M. L. Du and J. B. Delos. Effect of closed classical orbits on quantum spectra: Ionization of atoms in a magnetic field. I. Physical picture and calculations. *Physical review. A* 38, 1896–1912 (1988).
- [205] M. L. Du and J. B. Delos. Effect of closed classical orbits on quantum spectra: Ionization of atoms in a magnetic field. II. Derivation of formulas. *Physical Review A* 38, 1913–1930 (1988).
- [206] A. Konzelmann, B. Frank, and H. Giessen. Quantum confined Rydberg excitons in reduced dimensions. *Journal of Physics B: Atomic, Molecular and Optical Physics* 53, 024001 (2019).
- [207] D. B. Tran Thoai, R. Zimmermann, M. Grundmann, and D. Bimberg. Image charges in semiconductor quantum wells: Effect on exciton binding energy. *Physical Review B* 42, 5906–5909 (1990).

- [208] N. S. Rytova. The screened potential of a point charge in a thin film. *Moscow University Physics Bulletin* 3, 18 (1967).
- [209] L. V. Keldysh. Coulomb interaction in thin semiconductor and semimetal films. *JETP Lett.* 29, 716 (1979).
- [210] Y. Hefetz, X.-C. Zhang, and A. V. Nurmikko. Observation of exciton-exciton scattering in Cu_2O by time-resolved photomodulation spectroscopy. *Physical Review B* 31, 5371 (1985).
- [211] J. Shumway and D. M. Ceperley. Quantum Monte Carlo treatment of elastic exciton-exciton scattering. *Physical Review B* 63, 165209 (2001).
- [212] F. Bassani and M. Rovere. Biexciton binding energy in Cu_2O . *Solid State Commun.* 19, 887–890 (1976).
- [213] V. Bendkowsky, B. Butscher, J. Nipper, J. P. Shaffer, R. Löw, and T. Pfau. Observation of ultralong-range Rydberg molecules. *Nature* 458, 1005–1008 (2009).
- [214] A. Junginger, J. Main, and G. Wunner. Quantum-classical model for the formation of Rydberg molecules. *Physical Review A* 86, 012713 (2012).
- [215] M. Schmidt. *Hoch angeregte Resonanzen im Absorptionsspektrum von Kupferoxydul in gekreuzten elektrischen und magnetischen Feldern*. Bachelor's thesis, Universität Stuttgart (2018).



Zusammenfassung in deutscher Sprache

Die klassische Physik liefert eine akkurate Beschreibung beobachtbarer Phänomene auf mesoskopischen und makroskopischen Längenskalen und spielt damit eine entscheidende Rolle in unserem Verständnis unserer Umwelt. Auf mikroskopischen Längenskalen ist eine rein klassische Beschreibung nicht mehr möglich und die quantenmechanischen Eigenschaften des Systems treten zu Tage. Der Zustand eines solchen Systems wird durch eine komplexwertige Wellenfunktion beschrieben. Diese lässt sich jedoch selbst nicht messen und auch ihre Interpretation im Rahmen der Kopenhagener Deutung als Wahrscheinlichkeitsamplitude ist nur schwer mit unserer Alltagserfahrung zu vereinbaren. Einen intuitiveren Zugang liefern semiklassische Methoden. Ein Paradebeispiel liefert das Bohr-Sommerfeldsche Atommodell [18, 19]. Aufgrund der selben mathematischen Struktur des Coulombschen Gesetzes und des Newtonschen Gravitationsgesetzes bewegen sich die Elektronen auf Kepler-Ellipsen um den positiv geladenen Atomkern, ganz ähnlich wie sich die Planeten um die Sonne bewegen. Anhand von semiklassischen Quantisierungsvorschriften lassen sich die klassischen Bahnen einem Quantenzustand zuordnen. Für das Wasserstoffproblem sagt das Bohr-Sommerfeldsche Atommodell dann korrekt das Energiespektrum voraus.

Ein analoges Problem lässt sich in Halbleitern formulieren. Wird hier ein Elektron aus dem Valenz- ins Leitungsband angehoben, so lässt es im Valenzband einen unbesetzten Platz zurück. Dieser lässt sich durch ein positiv geladenes Quasiteilchen, das Loch, beschreiben. Das Loch kann nun über die Coulombkraft mit dem Elektron im Leitungsband wechselwirken und gebundene Zustände, die Exzitonen, bilden. In einer ersten Näherung können diese Zustände anhand eines wasserstoffartigen Modells verstanden werden. In der wegweisenden Arbeit von T. Kazimierczuk et al. konnte für Kupferoxydul eine Rydbergserie bis zur Hauptquantenzahl $n = 25$ beobachtet werden [43]. Dieses Experiment legte damit den Grundstein für intensive Forschung auf dem Feld der Rydbergexzitonen [53–111]. Die größten Zustände haben dabei eine Ausdehnung im Mikrometerbereich, sie erreichen somit Skalen, auf denen das Korrespondenzprinzip anwendbar sein sollte und das Quantensystem anhand von klassischer Dynamik ver-

ständig wird. Eine genauere Untersuchung der Spektren zeigt dabei Abweichungen von einem rein wasserstoffartigen Verhalten. Diese Abweichungen lassen sich anhand der komplexen Bandstruktur erklären, welche die kubische O_h Symmetrie des Kristalls trägt [45–48]. Dies eröffnet nun die Fragen, welchen Einfluss die Bandstruktur auf die klassische Dynamik des Systems hat und ob die quantenmechanischen Eigenschaften von Kupferoxydul mithilfe semiklassischer Methoden anhand dieser klassischen Bahnen verstanden werden können.

Kapitel 2: Nichtlineare Dynamik in Hamiltonschen Systemen

Zunächst führen wir die Grundlagen ein, die ein theoretisches Verständnis von nichtlinearer Dynamik und Chaos in Hamiltonschen Systemen ermöglicht. Dazu führen wir den Hamilton-Formalismus ein, wobei sich die klassische Dynamik durch Integration der Hamiltonschen Bewegungsgleichungen

$$\dot{\gamma} = \mathbf{J} \frac{\partial H}{\partial \gamma},$$

ergibt. Nachfolgend betrachten wir die klassische Dynamik integrierbarer Systeme. Dabei tritt die gleiche Anzahl an unabhängigen Erhaltungsgrößen wie die Zahl der Freiheitsgrade auf. Im gebundenen System lassen sich dann Wirkungs-Winkel-Variablen $\mathbf{I}, \boldsymbol{\theta}$ einführen, welche die Dynamik auf Tori im Phasenraum charakterisieren. Für rationale Frequenzverhältnisse ω_i/ω_j der Umläufe auf den einzelnen Tori ergeben sich periodische Bahnen, man spricht dann von resonanten Tori. Dabei stellt sich nun die Frage, was mit den Strukturen im Phasenraum beim hinzuaddieren einer nichtintegrierbaren Störung geschieht. Für die nichtresonanten Tori wird diese Frage durch das KAM Theorem beantwortet [5–7]. Dieses besagt, dass fast alle Tori eine kleine Störung überleben und lediglich deformiert werden. Bei einem Anwachsen der Störung brechen mehr und mehr Torusstrukturen auf und es bilden sich chaotische Bereiche aus. Im zweidimensionalen System liefert das Poincaré-Birkhoff-Theorem eine Aussage für die resonanten Tori [8–10]. Aus diesem ergibt sich, dass die resonanten Tori in eine gerade Anzahl von Fixpunkten zerfallen, wobei die eine Hälfte elliptisches (stabiles), die andere Hälfte hyperbolisches (instabiles) Verhalten aufweist.

Abschließend werden verschiedene Verfahren eingeführt, welche die Untersuchung des Phasenraums ermöglichen. Explizit sind das Poincaré-Schnitte, Stabilitätsparameter wie der Lyapunov-Exponent und Lagrangesche Deskriptoren (LD). Poincaré-Schnitte eignen sich dabei besonders zur Untersuchung zweidimensionaler Systeme. Die Dynamik in der Ebene wird dabei durch zwei Koordinaten x und y bestimmt. Nun wählt man eine Schnittbedingung, z.B. $x = 0$, und betrachtet dort die Koordinate y und ihren kanonisch

konjugierten Impuls p_y . Diese charakterisieren die Dynamik des Systems dann vollständig. Der übrig gebliebene Impuls p_x ergibt sich aus der Energieerhaltung. Chaotische Gebiete zeigen sich dann durch stochastische Gebiete im Phasenraum. Zur Stabilitätsanalyse betrachten wir die Stabilitätsmatrix $\mathbf{M}(0, T)$, welche eine Störung

$$\Delta\gamma(T) = \mathbf{M}(0, T)\Delta\gamma(0),$$

des Phasenraumvektors γ im zeitlichen Verlauf beschreibt. Aus ihren Eigenwerten λ_i lässt sich dann der Lyapunov-Exponent

$$\Lambda_i(T) = \frac{1}{T} \ln(|\lambda_i(0, T)|),$$

für die jeweilige Richtung bestimmen. Der Lagrangesche Deskriptor gibt die Bogenlänge einer Bahn für gegebene Startbedingungen γ_0 an [11, 12]

$$\text{LD}(\gamma_0, T) = \int_0^T \|\mathbf{v}\| dt.$$

Für Bereiche regulärer Dynamik, in denen eine kleine Abweichung der Anfangsbedingungen auch klein bleibt, erwartet man qualitativ ähnliches Verhalten. Geht man über in Phasenraumbereiche mit qualitativ anderem Verhalten, so erwartet man, dass sich auch das Verhalten des LD ändert. Je nach System kann die Bogenlänge allerdings stark von den Anfangsbedingungen abhängen, sodass lokale Fluktuationen nicht mehr aufgelöst werden können. Um dies zu umgehen, lässt sich ein Indikator auf Basis der zweiten Ableitung des LDs einführen [13]. Ähnlich wie bei den Poincaré-Schnitten weisen stochastische Regionen dann auf chaotisches Verhalten hin.

Kapitel 3: Semiklassische Beschreibung Hamiltonscher Systeme

Anschließend werden die Grundlagen der semiklassischen Physik diskutiert. Die Ansätze von Bohr und Sommerfeld werden hierzu erweitert [18, 19]. Einstein erkannte die ausgezeichnete Rolle der Wirkungsvariablen, auf welche er die Koordinaten in Sommerfelds Quantisierungsvorschrift einschränkte [20]. Dies liefert auch eine Erklärung für das Versagen der alten Quantenmechanik bei der Quantisierung von Mehrelektronensystemen wie Helium. Die zugrundeliegende Dynamik des Dreikörperproblems ist nämlich chaotisch, was ein Einführen von Wirkungs-Winkel-Variablen verhindert. Mit dem Aufkommen der Quantenmechanik konnte auch die Semiklassik weiter entwickelt werden. Eine semiklassische Behandlung der Wellenfunktion zeigt nun, dass singuläre Punkte auftreten, welche in den Quantisierungsvorschriften berücksichtigt werden müssen. Dies

führt auf die EBK-Methode [20–22]

$$I_i = \frac{1}{2\pi} \oint_{\mathcal{C}_i} \mathbf{p} d\mathbf{r} = \hbar \left(n_i + \frac{\alpha_i}{4} \right).$$

Der Maslov-Index α_i zählt dabei die Anzahl der singulären Punkte, die auf dem Pfad \mathcal{C}_i durchlaufen werden. Auf Basis dessen konnten Berry und Tabor eine semiklassische Formel für die Zustandsdichte ableiten [23, 24]. Jede periodische Bahn liefert dabei einen oszillierenden Beitrag, wobei die Amplitude von Bahnparametern abhängt. Für nichtintegrale Systeme liefert die Gutzwiller-Spurformel einen ähnlichen Ausdruck, wobei die Amplituden nun über Eigenschaften der isolierten periodischen Bahnen charakterisiert sind [25–27]. In beiden Fällen ergibt sich aber eine Form

$$d_{\text{sc}}(E) = \bar{d}(E) + \text{Re} \sum_{\text{po}} \mathcal{A}_{\text{po}} \exp(iS_{\text{po}}/\hbar),$$

wobei sich lediglich die Amplituden unterscheiden. Phasenfaktoren, die sich aufgrund der Topologie der Bahn ergeben, werden hier in der komplexen Amplitude aufgenommen.

Kapitel 4: Von Festkörpersystemen zu Exzitonen in Kupferoxydul

In diesem Kapitel wird nun, ausgehend von der theoretischen Beschreibung von Festkörpern das theoretische Modell für Exzitonen in Kupferoxydul entwickelt. Der volle Hamiltonian des Systems stellt ein komplexes Vielteilchenproblem dar, in dem die Wechselwirkung von Elektronen und Kernen berücksichtigt werden muss. Die Born-Oppenheimer-Näherung erlaubt dann eine getrennte Betrachtung von Elektronen und Kernen [149]. Berücksichtigt man nun die periodische Struktur kristalliner Festkörper und nimmt an, dass jedes Elektron ein ähnliches effektives Potenzial erfährt, so führt das auf die Beschreibung der Elektronen mithilfe von Blochfunktionen [155]. Damit ergibt sich im Halbleiter eine Bandstruktur wobei Energiebereiche auftreten, in denen keine Elektronen vorkommen können. Im Grundzustand bezeichnet man die voll besetzten Bänder als Valenzbänder, während die darüber liegenden Bänder als Leitungsbander bezeichnet werden. Im Γ -Punkt bei $\mathbf{p} = 0$ weisen diese ein annähernd parabolisches Verhalten auf. In der Nähe des Γ -Punktes lassen sich in Halbleitern Elektronen aus dem obersten Valenzband ins unterste Leitungsband anregen. Dabei lässt das Elektron eine leere Stelle im Valenzband zurück, die als positives Quasiteilchen, welches man als Loch bezeichnet, behandelt werden kann. In einem einfachen Modell können gebundene Elektron- und Loch-Paare, die Exzitonen, wasserstoffartig behandelt werden, wobei die beiden Teilchen über die Coulombwechselwirkung interagieren. Neben einer ausgeprägten Rydbergserie lassen sich allerdings auch Abweichungen von einem rein wasserstoffartigen Verhalten beobachten, welche auf die komplexe Valenzbandstruktur zurückgeführt

werden können [45–48]. Die Beschreibung des Systems erfolgt dann im Rahmen der Luttinger-Kohn-Theorie [49–51]. Dabei wird ein Quasispin $I = 1$ eingeführt, der das dreifach entartete Valenzband des Kristalls beschreibt. Durch die Kopplung des Lochspins an den Quasispin kommt es zur Aufspaltung des Valenzbandes. Daraus resultieren drei Exzitonserien, eine gelbe und zwei grüne, eine mit leichten und eine mit schweren Löchern. Der volle Hamiltonian beinhaltet dann neben wasserstoffartigen Anteilen noch Korrekturterme $H_{\text{band}}(\mathbf{p}, \mathbf{I}, \mathbf{S}_h)$, die mit der kubischen Symmetrie des Kristalls vereinbar sind,

$$H = E_g + \frac{\gamma'_1}{2m_0} \mathbf{p}^2 + H_{\text{band}}(\mathbf{p}, \mathbf{I}, \mathbf{S}_h) - \frac{e^2}{4\pi\epsilon_0\epsilon|\mathbf{r}|}.$$

Kapitel 5: Adiabatischer Ansatz für die Exzitondynamik in Kupferoxydul

Im vollen Hamiltonian treten im Vergleich zum wasserstoffartigen Fall neue Spinfreiheitsgrade auf, die kein klassisches Analogon besitzen. Um diese mitzubeschreiben, entwickeln wir in diesem Kapitel einen adiabatischen Ansatz. Dieser fußt auf einer Betrachtung der Energieaufspaltungen. Für die Spinfreiheitsgrade ist diese über die Spin-Bahn-Kopplung Δ festgesetzt, während die Aufspaltung benachbarter Rydbergzustände mit n^{-3} abfällt. Da die Zeitskalen, auf denen sich die Dynamik in den jeweiligen Freiheitsgraden abspielt, mit dem Inversen der Energieaufspaltungen gehen, sieht man, dass schon ab $n = 3$ die Spindynamik deutlich schneller abläuft als die Dynamik im Ortsraum. In Analogie zur Born-Oppenheimer-Näherung behandeln wir die schnelle Spindynamik im quantenmechanischen Formalismus. Dazu diagonalisieren wir die Bandstrukturterme des Hamiltonians $H_{\text{band}}(\mathbf{p}, \mathbf{I}, \mathbf{S}_h)$ in einer Basis für den Quasi- und Lochspin. Dies führt zu einer Beschreibung über Energieflächen im Impulsraum $W_k(\mathbf{p})$, die sich dann direkt den verschiedenen Exzitonserien zuordnen lassen. Für die Energieflächen lassen sich analytische Ausdrücke finden

$$W_k = -\frac{c_5}{6} + \sqrt{-\frac{4p}{3}} \cos \left[\frac{1}{3} \arccos \left(-\frac{q}{2} \sqrt{-\frac{27}{p^3}} \right) - \frac{2\pi(k-1)}{3} \right],$$

wobei die Funktionen c_5 , p , und q in Anhang D gegeben sind. Es ergeben sich nun Hamiltonians der Form

$$\tilde{H} = \frac{\gamma'_1 \mathbf{p}^2}{2m_0} + W_k(\mathbf{p}) - \frac{e^2}{4\pi\epsilon_0\epsilon r}.$$

Diese erlauben nach Wahl einer Energiefläche die Dynamik der zugehörigen Serie zu berechnen, indem die Hamiltonschen Bewegungsgleichungen gelöst werden. Dabei tragen die Energieflächen die kubische Symmetrie des Systems.

Kapitel 6: Klassische Dynamik der gelben Exzitonserie

In diesem Kapitel betrachten wir die klassische Dynamik der gelben Serie. Poincaré-Schnitte in den beiden Symmetrieebenen des Kristalls zeigen dabei große reguläre Bereiche mit Torusstrukturen, die um einen zentralen Fixpunkt orientiert liegen. Im äußersten Bereich der Poincaré-Schnitte zeigen sich stochastische Gebiete, die auf chaotisches Verhalten zurückzuführen sind. Die klassischen Bahnen sind dabei Fixpunkte in den Poincaré-Schnitten. Dabei lassen sich, wie durch das Poincaré-Birkhoff-Theorem vorhergesagt, jeweils zwei Partnerorbits finden, von denen einer elliptisches, der andere hyperbolisches Verhalten an den Fixpunkten zeigt. Im Ortsraum zeigen die klassischen Bahnen eine Sekularbewegung von Keplerellipsen. Neben den zweidimensionalen Bahnen in den Symmetrieebenen treten dabei auch vollständig dreidimensionale Bahnen auf, wobei sich nun vier Partnerorbits finden lassen. Die periodischen Bahnen lassen sich dann durch zwei beziehungsweise drei Windungszahlen charakterisieren, die sich über die Fourieranalyse der Bahn im Ortsraum zuordnen lassen. Dies erlaubt uns dann, die Wirkungsvariablen der Bahnen zu extrahieren, indem die Wirkung mithilfe eines Differenzenquotientens abgeleitet wird. Die Stabilität der Bahnen wird anhand der Stabilitätsmatrix untersucht. Dabei zeigt sich, dass die Bahnen in der Ebene orthogonal zu $[1\bar{1}0]$ instabil sind gegen Auslenkungen aus der Ebene, während die Bahnen in der Ebene normal zu $[100]$ hauptsächlich stabiles Verhalten gegen Auslenkungen aus der Ebene zeigen. Bereiche in denen der zugehörige Stabilitätseigenwert eins erreicht, lassen sich mit dem Auftauchen dreidimensionaler Bahnen in Verbindung setzen. In den Symmetrieebenen selbst ist die Stabilität gegen Auslenkungen in der Ebene wie erwartet stabil für einen und instabil für den anderen Partnerorbit, wobei sich diese Unterscheidung anhand der Stabilitätsmatrix für längere Orbits nicht mehr durchführen lässt, da hier die jeweiligen Stabilitätseigenwerte numerisch nicht mehr von eins unterschieden werden können.

Kapitel 7: Nachweis der klassischen Exzitonbahnen in den Quantenspektren von Kupferoxydul

Um die Existenz der im vorangegangenen Kapitel gefundenen Exzitondynamik in den Quantenspektren nachzuweisen, sollen nun semiklassische Methoden verwendet werden. Dabei trägt jede Bahn sinusförmige Fluktuationen zu den Quantenspektren bei. Besonders einfach werden die Ausdrücke für die semiklassische Zustandsdichte dabei für

Systeme die eine Skalierungseigenschaft aufweisen. In den skalierten Einheiten hängen die Amplituden dann nicht mehr vom Skalierungsparameter w ab und die Wirkung weist eine lineare Skalierung mit dem Parameter auf. Der resultierende semiklassische Ausdruck

$$d_{sc}(w) = \bar{d}(w) + \operatorname{Re} \sum_{p_0} \mathcal{A}_{p_0} \exp\left(i\tilde{S}_{p_0} w\right)$$

kann als Fourierreihe in der skalierten Wirkung aufgefasst werden. Im fouriertransformierten Wirkungsspektrum werden die Beiträge der Bahnen durch Delta-Peaks bei den skalierten Wirkungen der klassischen periodischen Bahnen sichtbar. Das Wasserstoffproblem hat dabei eine solche Skalierungseigenschaft für den Skalierungsparameter

$$n_{\text{eff}} \equiv \sqrt{E_{\text{Ryd}}/(E_g - E)}.$$

Nach Multiplikation mit n_{eff}^2 wird der Hamiltonian energieunabhängig. Um für das Modell mit Bandstruktur diese Skalierungseigenschaft wieder herzustellen, führen wir eine Skalierungstechnik für die Spin-Bahn-Kopplung ein,

$$\Delta \rightarrow \tilde{\Delta} = \frac{n_0^2}{n_{\text{eff}}^2} \Delta.$$

Quantenmechanisch lassen sich Spektren für n_{eff} berechnen, die zu einer vorgegebenen klassischen Dynamik bei n_0 gehören. Die so berechneten skalierten quantenmechanischen Spektren lassen sich als Summe von Delta-Peaks leicht fouriertransformieren. Das quantenmechanische Wirkungsspektrum weist Peaks auf, die sich über die skalierte Wirkung mit klassischen Bahnen identifizieren lassen. Dabei lässt sich so gut wie allen dominanten Peaks eine klassische Bahn zuordnen. Eine Untersuchung der Energieabhängigkeit zeigt dabei, dass die Wirkungsspektren umso mehr von einem rein wasserstoffartigen Verhalten abweichen, je niedriger n_0 gewählt wird.

Kapitel 8: Quantendefekte für die gelbe Exzitonenserie

Wie wir gesehen haben, weist der Phasenraum der gelben Exzitonenserie große fastintegrale Gebiete mit Torusstrukturen auf. In diesem Fall kann über die EBK-Methode eine Torusquantisierung durchgeführt werden. Das Ziel ist die Berechnung der Quantendefekte $\delta_{n,l}$ für die gelbe Serie, welche dann die Aufspaltung in verschiedene Drehimpulszustände erklärt. Diese Beschreibung lässt sich bereits in einem sphärischen Modell realisieren, wobei die sphärischen Anteile über

$$\mu' = \frac{6\gamma_3 + 4\gamma_2}{5\gamma_1}$$

charakterisiert sind. Dabei zeigen sich allerdings starke Abweichungen zwischen Materialparametern die direkt aus Bandstrukturrechnungen bestimmt wurden [48] und früheren Ansätzen, wo der Materialparameter über einen Fit an die experimentellen Spektren bestimmt wurde [122]. In Ref. [48] werden dabei noch weitere Materialparameter berücksichtigt, die weitere sphärische Terme und kubische Korrekturen mit einschließen. Da die Materialparameter von der Bandstruktur stammen müssen, gehen wir nun vom Modell mit der vollen kubischen Symmetrie aus und bilden einen sphärischen Durchschnitt. Betrachtet man den aus einem Fit erhaltenen resultierenden Parameter für μ' , so findet man eine gute Übereinstimmung mit dem in Ref. [122] gefundenen Wert, was nun einen Zusammenhang der ursprünglich widersprüchlich erscheinenden Modelle herstellt. Die Quanteneffekte lassen sich dann durch Quantisierung der Wirkungs-Winkel-Variablen bestimmen

$$\begin{aligned} I_\varphi &= \frac{1}{2\pi} \oint p_\varphi d\varphi = \frac{1}{2\pi} \oint L_z d\varphi = m, \\ I_\vartheta &= \frac{1}{2\pi} \oint p_\vartheta d\vartheta = \frac{1}{2\pi} \oint \sqrt{\mathbf{L}^2 - \frac{L_z^2}{\sin^2 \vartheta}} d\vartheta = l - |m| + \frac{1}{2}, \\ I_r &= \frac{1}{2\pi} \oint p_r dr = n_r + \frac{1}{2}, \end{aligned}$$

wobei $n = n_r + l + 1$. Die semiklassischen Quanteneffekte stimmen für S-Zustände bereits gut mit Literaturwerten [47, 48, 66] überein, während für höhere l die semiklassischen Resultate etwas zu hoch liegen. Dies lässt sich beheben, wenn beim Fitten der sphärischen Durchschnitte berücksichtigt wird, dass der klassisch erlaubte Impulsbereich für wachsende l kleiner wird. Damit erhält man nun Materialparameter für die verschiedenen Serien $\mu'_S = 0.51$, $\mu'_P = 0.41$, $\mu'_D = 0.38$ und $\mu'_F = 0.36$, welche eine gute Übereinstimmung mit quantenmechanischen Resultaten liefert [47, 48, 66].

Kapitel 9: Chaos in der grünen Exzitonenserie

In diesem Kapitel wird nun die klassische Dynamik der grünen Exzitonenserien den Resultaten der gelben Serie gegenübergestellt. In den Poincaré-Schnitten für $n_0 = 5$ zeigt sich hier ein qualitativ unterschiedliches Verhalten zwischen gelber Serie und den grünen Serien für die Ebene orthogonal zu $[1\bar{1}0]$. Während für die gelbe Serie ein elliptischer Fixpunkt im Zentrum des Poincaré-Schnittes gefunden werden kann, lässt sich für die grüne Serie ein zentraler hyperbolischer Fixpunkt beobachten. Auch sind die chaotischen Phasenraumbereiche der grünen Serie deutlich größer als für die gelbe. Bei einer genaueren Betrachtung der Energieabhängigkeit findet sich, dass die zentralen Fixpunkte für die grünen Serien zunächst stabil sind und dann eine Bifurkation durchlaufen, die letztendlich in einem vollständig chaotischen Phasenraum resultiert. Der Stabilitätswechsel

lässt sich dabei auch anhand des Lyapunov-Exponenten nachweisen. Abschließend wird der dreidimensionale Phasenraum mithilfe des Lagrangeschen Deskriptors untersucht. Auch hier zeigen sich für die grünen Serien große chaotische Gebiete, die beim Übergang von der Ebene normal zu $[100]$ zur Ebene normal zu $[1\bar{1}0]$ anwachsen. Exzitonen in Kupferoxydul bilden somit ein Zweikörperproblem, dessen Dynamik auch bereits ohne die Existenz externer Felder chaotisches Verhalten aufweist.

Kapitel 10: Zusammenfassung und Ausblick

In den vorangegangenen Kapitel haben wir gesehen, dass sich die wesentlichen quantenmechanischen Eigenschaften von Kupferoxydul anhand von klassischen Bahnen verstehen lassen. Die semiklassischen Interpretationen lassen sich prinzipiell noch weiter ausbauen, um so beispielsweise die Hyperfeinaufspaltung der F-Zustände [45] im Modell mit der vollen kubischen Symmetrie über die EBK-Methode direkt klassischen Bahnen zuzuordnen.

Innerhalb des adiabatischen Ansatzes liefern semiklassische Quantisierungsvorschriften gebundene Zustände für die grüne Serie. In Realität sind diese aber aufgrund ihrer Kopplung an das gelbe Kontinuum Resonanzen mit endlicher Lebensdauer [53]. Diese können nun in Anlehnung an die Molekülchemie durch eine Erweiterung der Born-Oppenheimer-Näherung semiklassisch beschrieben werden [187–191]. Dabei werden nicht-adiabatische Kopplungsterme mitberücksichtigt, welche nun erlauben, dass das Exziton zwischen den Energieflächen hin und her springt, bis auf der gelben Fläche der ungebundene Bereich erreicht wird und das Teilchen dissipiert. Erste Ansätze in einem einfachen eindimensionalen Modell konnten bereits Lebensdauern in der korrekten Größenordnung vorhersagen [192].

Darüber hinaus lassen sich die semiklassischen Methoden in Bereichen anwenden, in denen voll quantenmechanische Rechnung versagen. Interessante Beispiele wären hierbei Magnetoexzitonen in der Nähe der Ionisationsschwelle. In atomphysikalischen Systemen treten hier Quasi-Landau-Resonanzen auf, welche im Rahmen semiklassischer Theorien erklärt werden können [182, 196–203]. Hierbei wäre es nun interessant zu sehen, welche Modifikationen der Einfluss der Bandstruktur in den Absorptionsspektren hervorruft, welche sich semiklassisch dann durch die *closed-orbit theory* berechnen lassen sollten [204, 205].

Ein weiterer interessanter Aspekt wäre die semiklassische Untersuchung von Exzitonen in *Quantum Wells* [101, 109, 206]. Aufgrund der Grenzflächen müssen hier Bildladungen im Potenzial mitberücksichtigt werden [207]. Weiterhin ist aufgrund der Symmetriereduktion gegenüber des Festkörpers eine quantenmechanische Behandlung mit Bandstruktur numerisch aufwendig. So finden aktuell Rechnungen nur in einem wasserstoffartigen Modell statt [101, 109]. Semiklassisch lässt sich der Einfluss der Bandstruktur

über den adiabatischen Ansatz verhältnismäßig einfach mitberücksichtigen.

Weitere interessante Fragestellungen befassen sich mit der Wechselwirkung von Rydberg-Exzitonen [86, 210–212]. So könnten beispielsweise Quanten-klassische Ansätze Aussagen über die Existenz von Exziton-Molekülen in Analogie an die Rydberg-Moleküle in der Atomphysik liefern [213, 214].

Jan Ertl

Lebenslauf

Persönliche Daten

Geburtstag: 11.02.1994
Geburtsort: Stuttgart

Sprachen

Deutsch Muttersprache
Englisch Fließend
Französisch Grundkenntnisse

Schulbildung

2000–2004 **Grundschule**, Benningen am Neckar
2004–2012 **Gymnasium**, *Friedrich Schiller Gymnasium*, Marbach am Neckar

Studium

2012-2017 **Bachelor Studium Physik**, *Universität Stuttgart*
Bachelorarbeit Physik, *Polaritontransformation der gelben Magnetoexzitonen in Kupferoxydul*, unter der Betreuung von Prof. Dr. Jörg Main, 1. Institut für Theoretische Physik, Universität Stuttgart

2017-2019 **Master Studium Physik**, *Universität Stuttgart*
Masterarbeit Physik, *Adiabatic approximation for the dynamics of magnetoexcitons in Cu₂O*, unter der Betreuung von Prof. Dr. Jörg Main, 1. Institut für Theoretische Physik, Universität Stuttgart

2020-2024 **Promotionsstudium Physik**, *Universität Stuttgart*

Berufliche und wissenschaftliche Tätigkeiten

1/1/20 - 31/12/20 **Wissenschaftlicher Mitarbeiter**, *Experimentelle Physik 2, Technische Universität Dortmund*

1/1/21 - 31/7/24 **Wissenschaftlicher Mitarbeiter**, *1. Institut für Theoretische Physik, Universität Stuttgart*

Publikationen

- **Exciton-polaritons in cuprous oxide: Theory and comparison with experiment**, F. Schweiner, J. Ertl, J. Main, G. Wunner, Ch. Uihlein, *Phys. Rev. B*, **96**, 245202 (2017).
- **Classical and semiclassical description of Rydberg excitons in cuprous oxide**, J. Ertl, P. Rommel, M. Mom, J. Main, M. Bayer, *Phys. Rev. B* **101**, 241201(R) (2020).
- **Signatures of Exciton Orbits in Quantum Mechanical Recurrence Spectra of Cu₂O**, J. Ertl, M. Marquardt, M. Schumacher, P. Rommel, J. Main, M. Bayer, *Phys. Rev. Lett.* **129**, 067401 (2022).

- **Classical dynamics and semiclassical analysis of excitons in cuprous oxide**, J. Ertl, M. Marquardt, M. Schumacher, P. Rommel, J. Main, M. Bayer, Phys. Rev. B **109**, 165203 (2024).
- **Rydberg excitons in cuprous oxide: A two-particle system with classical chaos**, J. Ertl, S. Rentschler, J. Main, Chaos, submitted.
- **The energy level spectrum of the yellow exciton series in cuprous oxide**, J. Heckötter, A. Farenbruch, D. Fröhlich, M. Aßmann, D. R. Yakovlev, M. Bayer, M. A. Semina, M. M. Glazov, P. Rommel, J. Ertl, J. Main, H. Stolz, Physics Reports, submitted .
- **Quantum defects of Rydberg excitons in cuprous oxide: A semiclassical picture**, J. Ertl, J. Main, in preparation.

Wissenschaftliche Präsentationen und Fachvorträge

- **3rd International Workshop on Rydberg Excitons in Semiconductors 2019**, *Poster*, Durham, UK
- **Seminarvortrag, TU Dortmund 10.12.2019**, *Vortrag*, Dortmund, Germany
- **GiRyd Status Workshop 2020**, *Poster*, Mainz, Deutschland (Online)
- **4th International Workshop on Rydberg Excitons in Semiconductors 2020**, *Vortrag*, Online
- **GiRyd Status Workshop 2021**, *Vortrag und Poster*, Online
- **GiRyd Status Workshop 2022**, *Vortrag und Poster*, Mainz, Deutschland
- **5th International Workshop on Rydberg Excitons in Semiconductors 2022**, *Vortrag und Poster*, Aarhus, Dänemark
- **Advanced SRitp und GiRyd School on Giant Interactions in Rydberg Systems 2022**, *Poster*, Tel Aviv, Israel
- **GiRyd Status Workshop 2023**, *Vortrag*, Tübingen, Deutschland
- **6th International Workshop on Rydberg Excitons in Semiconductors 2023**, *Vortrag*, Rostock, Deutschland



Danksagung

Ich möchte mich bei all denjenigen bedanken, die mir bei der Umsetzung dieser Doktorarbeit geholfen haben.

- Herrn Prof. Dr. Jörg Main, für die Vergabe des spannenden Themas, hilfreiche Diskussionen und hervorragende Betreuung und Unterstützung, sowie die Möglichkeit meine Ergebnisse bei verschiedenen Konferenzen vorzustellen. Darüber hinaus für die gute Zusammenarbeit auf dem Gebiet der Exzitonen, sowie die Übernahme des Hauptberichts.
- Herrn Prof. Dr. Manfred Bayer für das Interesse an meiner Forschung und die gute Zusammenarbeit auf dem Gebiet des Exzitonen. Ohne seine Unterstützung wäre diese Arbeit nicht zustande gekommen.
- Herrn Prof. Dr. Johannes Roth, für die Übernahme des Mitberichtes.
- Herrn Prof. Dr. Ronny Nawrodt, für die Übernahme des Prüfungsvorsitzes.
- Herrn Dr. Patric Rommel, für die Hilfe bei offenen Fragen, spannenden Diskussionen, die gute Zusammenarbeit auf dem Gebiet der Exzitonen in Kupferoxydul und die tolle Büroatmosphäre.
- Herrn Michel Mom (MSc.), Herrn Michael Marquardt (MSc.), Herrn Moritz Schumacher (MSc.), Herrn Sebastian Rentschler (BSc.), Herrn Dr. Julian Heckötter, Herrn Dr. Andreas Farenbruch, Herrn Prof. Dr. Dietmar Fröhlich, Herrn Prof. Dr. Marc Aßmann, Herrn Prof. Dr. Dmitri Yakovlev, Frau Dr. Marina Semina, Herrn Prof. Dr. Mikhail Glazov, sowie Herrn Prof. Dr. Heinrich Stolz für die gute Zusammenarbeit auf dem Gebiet der Exzitonen in Kupferoxydul.
- Herrn Dr. Johannes Reiff sowie Herrn Finn Schmolke (MSc.), in ihrer Funktion als Systemadministrator.

Danksagung

- Frau Monika Bund und Frau Michaela Wäscher, für all die Unterstützung bei verwaltungstechnischen Aufgaben.
- Allen weiteren Mitgliedern des 1. Institut für Theoretische Physik, für die tolle Atmosphäre und spannenden Gespräche in der Kafferrunde.
- Meinen Freunden und meiner Familie, dabei insbesondere meinen Eltern, durch deren Unterstützung diese Arbeit überhaupt erst ermöglicht wurde.

Ehrenwörtliche Erklärung

Ich erkläre, dass ich diese Dissertation, abgesehen von den ausdrücklich bezeichneten Hilfsmitteln, selbständig verfasst habe.

Stuttgart, den 12.06.2024

Jan Ertl